2014

Application of Two-Photon Absorbing Fluorene-Containing Compounds in Bioimaging and Photodyanimc Therapy

Xiling Yue
University of Central Florida

APPLICATION OF TWO-PHOTON ABSORBING FLUORENE-CONTAINING COMPOUNDS IN BIOIMAGING AND PHOTODYNAMIC THERAPY

by
XILING YUE
B. S. Fudan University, 2009

A dissertation submitted in partial fulfillment of the requirements
for the degree of Doctor of Philosophy
in the Department of Chemistry
in the College of Science
at the University of Central Florida
Orlando, Florida

Fall Term

2014

Major Professor: Kevin D. Belfield

ABSTRACT

Two-photon absorbing (2PA) materials has been widely studied for their highly localized excitation and nonlinear excitation efficiency. Application of 2PA materials includes fluorescence imaging, microfabrication, 3D data storage, photodynamic therapy, etc. Many materials have good 2PA photophysical properties, among which, the fluorenyl structure and its derivatives have attracted attention with their high 2PA cross-section and high fluorescence quantum yield.

Herein, several compounds with 2PA properties are discussed. All of these compounds contain one or two fluorenyl core units as part of the conjugated system. The aim of this dissertation is to discuss the application of these compounds according to their photophysical properties. In chapters 2 to 4, compounds were investigated for cell imaging and tissue imaging. In chapter 5, compounds were evaluated for photodynamic therapy effects on cancer cells.

Chapters 2 and 3 detail compounds with quinolizinium and pyran as core structures, respectively. Fluorene was introduced into structures as substituents. Quinolizinium structures exhibited a large increase in fluorescence when binding with Bovine Serum Albumin (BSA). Further experiments in cell imaging demonstrated a fluorescence turn-on effect in cell membranes, indicating the possibility for these novel compounds to be promising membrane probes. Pyran structures were conjugated with arginylglycylaspartic acid peptide (RGD) to recognize integrin and introduced in cells and an animal model with tumors. Both probes showed specific targeting of tumor vasculature. Imaging reached penetration as deep as 350 μm in solid tumors and exhibited good resolution. These results suggest the RGD-conjugated pyran structure should be a good candidate probe for live tissue imaging.

Chapter 4 applied a fluorene core structure conjugated with RGD as well. Application of this fluorenyl probe compound is in wound healing animal models. Fluorescence was collected from vasculature and fibroblasts up to ≈ 1600 μm within wound tissue in lesions made on the skin of mice. The resolution of images is also high enough to recognize cell types by immunohistochemical staining. This technology can be applied for reliable quantification and illustration of key biological processes taking place during tissue regeneration in the skin.

Chapter 5 describes three fluorenyl core structures with photoacid generation properties. One of the structures showed excellent photo-induced toxicity. Cancer cells underwent necrotic cell death due to pH decrease in lysosomes and endosomes, suggesting a new mechanism for photodynamic therapy.

ACKNOWLEDGMENTS

I would like to first give thanks to my research advisor, Dr. Kevin Belfield, for giving me a lot of help during my Ph. D. study. Since I began in this group, he offered me many advices, encouragements, and supports for my research and qualifications. Especially during one time I would have given up one of my projects if without his encouragement to continue. Thanks to him, I got my first paper published from that project. He also gave me many opportunities to try new techniques, attend conferences and collaborate with different research groups. I really appreciate all these opportunities that help me be a better researcher.

I also want to specially thank Dr. Ciceron Yanez, who guided me with more than half of my entire Ph. D. projects. He is very nice to share his knowledge and techniques with me. I really learned a lot from him, not only scientific knowledge, but also his enthusiasm to science and optimistic attitude when confronting problems.

I would not have completed this thesis without the help of some other exceptional researchers. Dr. Alma Morales did the synthesis work for Chapter 2, 3, and 4. Dr. Ciceron Yanez did the synthesis work and photophysical measurements for Chapter 5. Dr. Sheng Yao also did the synthesis work for Chapter 5. Dr. Mykhailo Bondar did the photophysical measurement of Chapter 2 and 4. Mr. Adam Woodward did the photophysical measurement of Chapter 3. Mr. Zach Armijo and Mr. Kevan King also did the synthesis work for Chapter 2. Dr. Masanobu Komatsu's research group in Sanford Burnham Research institute helped the animal work for Chapter 3 and 4. Dr. Tero Jarvinen helped the animal work for Chapter 4. I want to thank all of them for the excellent research work they did.

I'm also grateful to all the other group members. Dr. Sheng Yao, Dr. Alma Morales, Dr. Andrew Frazer, and Dr. Taihong Liu are always willing to give helps whenever I need. Dr. Xuhua Wang helped me a lot when I first came here. He taught me how to do different experiments, and how to be a good researcher. Dr. Yuanwei Zhang gave me many helpful advices for my seminar and candidacy exam. Ms. Mengyuan Wang, who is also my roommate, as another Chinese girl coming to the group in the same year with me, is a big support for me in both working and living. Last but not least, Mr. Simon Tang, who is also my boyfriend, gave me lots of support in my research, as well as my life outside research.

In the end, I want to express my thanks and love to my parents, grandparents, and other family members. Their love makes me a stronger person, and supports me all the way during my Ph. D. studies.

TABLE OF CONTENTS

LIST OF FIGURES xii

LIST OF TABLES xvii

LIST OF SCHEMES xviii

CHAPTER 1. BACKGROUND 1

1.1 Two-Photon Absorption Mechanism 1

1.2 Two-Photon Fluorescence Microscopy 1

1.2.1 Two-Photon Fluorescence Microscopy Introduction 1

1.2.2 Two-Photon Fluorescence Compounds 2

1.2.3 Two-Photon Fluorescence Microscopy System 4

1.3 Two-Photon Photodynamic Therapy 5

1.3.1 Photodynamic Therapy 5

1.3.2 Two-Photon Photodynamic Therapy 6

1.3.3 Two-Photon Absorption Photosensitizer (2PA PS) 7

1.4 Fluorene Structure and Properties 9

1.4.1 Structure-Property Relations 9

1.4.2 Fluorene and Fluorene Derivatives 10

CHAPTER 2. APPLICATION OF FLUORENE-SUBSTITUTED QUINOLIZINIUM CATIONS IN PROTEIN LABELING 12

2.1 Introduction 12

2.2 Materials and Methods 14

2.2.1 Synthetic Strategy 14

2.2.2 BSA Binding Experiment 15

2.2.3 BSA Binding Constant 15

2.2.4 Cell Imaging 16

2.3 Results 17

2.3.1 Spectra of QFs 17

2.3.2 Increase of Fluorescence Emission of QFs with BSA Binding 21

2.3.3 Cell Imaging 22

2.4 Discussion 24

2.5 Conclusion 28

CHAPTER 3. APPLICATION OF INTEGRIN TARGETING FLUORENE-SUBSTITUTED PYRAN DYES IN TUMOR VASCULATURE IMAGING 29

3.1 Introduction 29

3.2 Materials and Methods 31

3.2.1 Structures of RGD Conjugated Pyran dyes with Fluorene Substitution (PFs) 31

3.2.2 Ethics Statement 32

3.2.3 Animal Model 32

3.2.4 Cytotoxicity Assay 32

3.2.5 Cell Imaging 32

3.2.6 Tissue Imaging 33

3.3 Results 33

3.3.1 Fluorescence Spectra 33

3.3.2 Cytotoxicity of PFs-**RGD** 35

3.3.3 Integrin Targeted Cell Endocytosis 35

3.3.4 Integrin Targeted Tumor Imaging 37

3.4 Discussion 40

3.5 Conclusion 43

CHAPTER 4. APPLICATION OF INTEGRIN TARGETING FLUORENE DYE IN WOUND VASCULATURE IMAGING 44

4.1 Introduction 44

4.2 Materials and Methods 47

4.2.1 Probe **1** Structure 47

4.2.2 Ethics Statement 49

4.2.3 Wound Healing Model and Administration of Probe **1** 49

4.2.4 Microscopy 50

4.2.5 Immunohistochemistry 51

4.3 Results 51

4.3.1 Fluorescence Spectra 51

4.3.2 Two-Photon Microscopy 52

4.3.3 Segmentation Analysis 53

4.3.4 Immunohistochemistry 54

4.4 Discussion 55

4.5 Conclusion 59

CHAPTER 5. APPLICATION OF SULFONIUM SALTS WITH A FLUORINE CORE TO INDUCE SELECTIVE CELL DEATH 60

5.1 Introduction 60

5.2 Materials and Methods 62

5.2.1 PAGs Structures 62

5.2.2 Encapsulation of PAGs 62

5.2.3 Cell Culture 63

5.2.4 Photocytotoxicity Assay 63

5.2.5 Lysosome Colocalization 64

5.2.6 Live Cell Imaging of PL-PAG **1** 64

5.2.7 Two-Photon Irradiation and Determination of the Type of Cell Death 64

5.2.8 Measurement of Lysosomal pH Drop 65

5.3 Results 66

5.3.1 Photophysical Properties of PAGs 66

5.3.2 Dark Toxicity and Post-Irradiation Toxicity of PL-PAGs in HCT 116 Cells 67

5.3.3 Colocalization of PL-PAG **1** and LysoTracker Red 69

5.3.4 Live Cell Imaging After Irradiation with PL-PAG **1** 70

5.3.5 Type of Cell Death 72

5.3.6 Lysosomal pH Drop 73

5.4 Discussion 75

5.5 Conclusion 79

CHAPTER 6. FUTURE WORK 81

6.1 2PA Fluorescent Probes and PDT Agents Encapsulated in Silica Nanoparticles 81

6.2 RGD Peptide Functionalized Silica Nanoparticles 82

6.3 Live Animal Treatment and Imaging 83

APPENDIX: LIST OF PUBLICATIONS DURING PH.D. DISSERTATION 85

REFERENCES 87

LIST OF FIGURES

Figure 1-1. One-photon and two-photon microscopy excitation. 2

Figure 1-2. Descanned and non-descanned detection path in one-photon and two-photon microscopy. 5

Figure 1-3. Conventional $^1O_2$ based PDT (left) and two-photon absorption photoacid generator based PDT.[7] 6

Figure 1-4. Schematics of various linear chromophores classified based on the substitution pattern. (D = donor group; π = π-conjugated bridge; A = acceptor group)[35] 9

Figure 1-5. Structure of the fluorene core. 11

Figure 2-1. Normalized linear absorption (1-5) and fluorescence (1′-2′) spectra of 1 (a) and 2 (b) in different solvents. Fluorescence spectra in CHX (1′) and TOL (2′). 18

Figure 2-2. Normalized 1PA (1) and degenerate 2PA (2) spectra of 1 (a) and 2 (b) in TOL. 20

Figure 2-3. Fluorescence emission of quinolizinium dyes was increased dramatically with increase of BSA concentration. 21

Figure 2-4. Quenching curves of BSA (λ_{ex} : 280 nm, λ_{em} : 340 nm) by binding with QF 1 (1) and 2 (2) at different ratios. F and F_0 are the intensities of BSA fluorescence emission with and without binding, respectively. 22

Figure 2-5. DIC (A) and Fluorescent (B, C) images of HeLa cells co-incubated with 1 (B) and Alexa Fluor® 488-WGA (C). Fluorescent images were scanned every 250 nm at z direction and then processed with Amira software. D shows the overlay image of B and C. Scale bar indicates 50 μ. 23

Figure 2-6. Colocalization of 1 (A, D, G) with microtubule (B), actin filaments (E) and vinculin (H) in HeLa cells. Different degrees of overlay (C, F, I) were observed between 1 and three proteins. Distribution of 1 appears to be more associated to vinculins (arrows in I), indicating possible binding between 1 and vinculins. Scale bars are 20 μm. 24

Figure 3-1. One-photon absorption, emission of PF 1 in CHX, DCM and DMSO, two-photon absorption of PF 1 in DCM and anisotropy in silicon oil (Si oil) are shown in the left spectrum (A). One-photon absorption (Abs), emission (Em), two-photon absorption (2PA) and anisotropy (R) of PF 2 in DMSO are shown in the right spectrum (B). 34

Figure 3-2. Viability of U87MG cells after 24 h incubation with RGD-conjugated PFs. 35

Figure 3-3. Fluorescence (A-E) and DIC overlay (F) images of MCF-7 (A) and U87MG cells (B-F) after 1 h incubation with PF 1 (D) or PF 1-RGD (A, C, E and F). B shows U87MG cells control. Scale bars show 10 μm. 36

Figure 3-4. Fluorescence (A-E) and DIC overlay (F) images of MCF-7 (A) and U87MG cells (B-F) after 1 h incubation with PF 2 (D) or PF 2-RGD (A, C, E and F). B shows U87MG cells control. Scale bars show 10 μm. 37

Figure 3-5. 3D reconstruction images (A, B) show the vasculature in tumor tissues from mice injected with PF 1 (A) or PF 1-RGD. Cross-section fluorescence at 200 μm depth (C, E) were analyzed (D). Scale bars show 50 μm. 38

Figure 3-6. 3D reconstruction images (A, B) show the vasculature in tumor tissues from mice injected with PF 2 (A) or PF 2-RGD. Cross-section fluorescence at 200 μm depth (C, E) were analyzed (D). Scale bars show 50 μm. 39

Figure 4-1. 2PFM of the ‘‘whole-mounted’’ wounds was performed and reconstructed for 3D visualization (a). RGD-containing probe 1 (e) was employed to target integrins. Integrin-expressing cells (b) and capillaries (c) in optical section are shown separately. d explains the depiction of a wound during the granulation tissue formation. 46

Figure 4-2. Excised wound healing sample was whole-mounted and imaged by 2PFM. 50

Figure 4-3. (A) One-photon absorption (1, 2), emission (1’, 2’) of probe 1 in water-chloroform mixture; (B) two-photon (1, 2, 3) and one photon (1’, 2’, 3’) absorption in chloroform, acetonitrile and water. 52

Figure 4-4. Segmentation analysis from 2PFM images. Fluorescent pixels were used to account for the vasculature. 53

Figure 4-5. Immunohistochemistry staining of tissue sections of wound healing specimen..... 54

Figure 5-1. Sulfonium salt 2PA PAGs structures. 62

Figure 5-2. One-photon absorption spectra of PAGs in PBS following Pluornic-127 encapsulation..... 67

Figure 5-3. Dark toxicity of PL-PAGs in HCT 116 cells. 68

Figure 5-4. Post-exposure toxicity of HCT 116 cells incubated with PL-PAG 1 and 3..... 69

Figure 5-5. DIC (a) and confocal fluorescence images of HCT 116 cells coincubated with PL-PAG 1 (b) and LysoTracker green (c). Overlay image (d) shows PL-PAG 1 mainly built up in lysosomes. Scale bar shows 50 μm..... 70

Figure 5-6. DIC and confocal fluorescence images of HCT 116 cells after irradiation with PL-PAG 1. Scale bar shows 50 μm..... 71

Figure 5-7. PI staining of HCT 116 cells after incubated with PL-PAG 1 and irradiated at 710 nm. Scale bar shows 50 μm. 73

Figure 5-8. Increase of acidic content in cell lysosomes after cells irradiated with PL-PAG 1. LysoSensor Green was employed as a pH indicator..... 74

Figure 5-9. Absorbance changes of Rhodamine B at 555 nm. Calibration curve was calculated to estimate H^+ generation..... 75

Figure 6-1. Three different silica nanoparticle architectures, designated from right as the compact core-shell particle, the expanded core-shell particle, and the homogeneous particle. [139]..... 82

Figure 6-2. Window chamber applied for live mouse imaging. (a) Photograph from coverslip side and (b) photograph (mirror image) from skin side. The window chamber had a diameter of 12 mm.[145] 83

Figure 6-3. Implantation of the window chamber on the skin of a mouse.[146] 84

LIST OF TABLES

Table 2-1. Linear photophysical and photochemical parameters of QF 1 in solvents with different polarity Δf 19

Table 2-2. Linear photophysical and photochemical parameters of QF 2 in solvents with different polarity Δf 19

Table 5-1. Photophysical properties of PAGs 66

LIST OF SCHEMES

Scheme 2-1. Synthesis of bis-fluorenyl quinolizinium QF 1. 14

Scheme 2-2. Synthesis of tetra-fluorenyl quinolizinium QF 2. 15

Scheme 3-1. Synthesis of PF 1, PF 1-RGD, PF 2, and PF 2-RGD. 31

Scheme 4-1. Synthesis of RGD conjugated probe 1. [107] 48

CHAPTER 1. BACKGROUND

1.1 Two-Photon Absorption Mechanism

Molecules can be excited to a higher energy electronic state from the ground state by absorption of photons. One molecule can usually be excited by one photon that has similar energy with its energy gap between the highest occupied molecular orbital and the lowest unoccupied molecular orbital. However, molecules exposed to high intensity light can also undergo near simultaneous absorption of two photons. The combined energy of the two photons can also access a stable excited state of the molecule.[1] This process is referred to as two-photon absorption (2PA).

Because of the demands of both a spatial and temporal overlap of two incident photons to undergo a 2PA, it can generate precisely localized photoexcitation. Therefore, 2PA has attracted significant attention for different applications, including bioimaging[2-4], photodynamic therapy [5-7], 3D data storage[8-10], etc.

1.2 Two-Photon Fluorescence Microscopy

1.2.1 Two-Photon Fluorescence Microscopy Introduction

Two-photon fluorescence microscopy (2PFM) has been widely used in bioimaging of cells and tissues. In traditional one-photon microscopy, incident light is absorbed predominantly at the surface following an exponential absorption profile. On the other hand, the extreme localized two-photon excitation allows for direct optical excitation below the surface at the focus

(**Figure 1-1**).[11] The precise localization can eliminate additional background excitation, and also prevent photobleaching and photodamage of surroundings. These advantages can help produce images with better contrast and higher resolution.

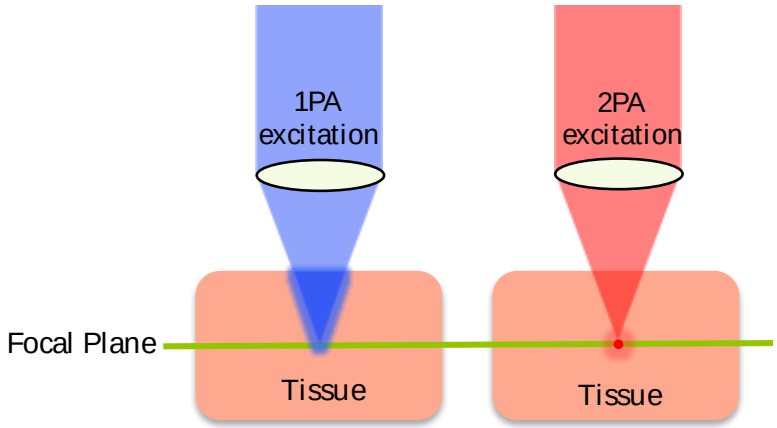

Figure 1-1. One-photon and two-photon microscopy excitation.

Besides, 2PFM applies longer wavelength, in the near infrared (NIR) region for excitation, relative to conventional confocal microscopy. Compared with visible light, biological materials undergo less absorption in the NIR region, resulting in higher penetration in tissues. As a result, 2PFM is also suitable for deep tissue penetration 3D bioimaging.

1.2.2 Two-Photon Fluorescence Compounds

A good candidate for 2PFM should have good photophysical properties. The parameter figure of merit (F_M) is applied to evaluate these properties. F_M is calculated by equation: $F_M = \Phi_f\delta/\Phi_d$, where Φ_f is the fluorescent quantum yield, δ is the 2PA cross-section, and Φ_d is the photodecomposition quantum yield. Structures with higher fluorescence quantum yield and 2PA

absorption cross-section, and lower photodecomposition quantum yield will have a higher F_M, indicating good photophysical properties.

The fluorescent quantum yield measures the efficiency of a material to transfer absorbed energy into fluorescence. A rigid molecule usually leads to a higher fluorescence quantum yield due to better conjugation and less rotational energy loss. In addition, substituents such as NO_2 and heavy atoms often lead to low fluorescence quantum yields via intersystem crossing to a triplet state. [1]

The 2PA cross-section relects the amount of photons the molecules can absorb under two-photon excitation. It is generally related to a molecule's polarizability, its π-electron conjugation length, and the donor/acceptor strength of the fluorophore's substituents.[12, 13]

The photodecomposition quantum yield indicates the efficiency at which a material is decomposed upon excitation. It relates to the reactivity of material. High photostability (low photodecomposition quantum yield) is of great importance to generate high quality images.

Water solubility is also important when applying a compound into biological systems. Good water solubility can be realized by either editing the molecule or applying drug delivery systems. Adding polyethyleneglycol (PEG) moieties or introducing acid groups in the structures can increase their solubility in polar solvents such as water.[14, 15] Liposome, micelle, and silica nanoparticles are widely used as drug delivery systems in bioimaging due to their good biocompatibility and capability to be functionalized with targeting structures.[16-18] This strategy may facilitate use of hydrophobic probes.

Other properties such as low cytotoxicity, efficient cell uptake, and long excitation/emission wavelength should also be added to the list of parameters in consideration for a good dye candidate.

1.2.3 Two-Photon Fluorescence Microscopy System

For the microscopy system, a special light source and detector are required. When the first photon passed through a molecule, the virtual state may form, but only persisting for a very short duration. Only when the second photon arrives before the decay of this virtual state, which is on the order of a few femtoseconds, two-photon excitation would occur. Therefore, an ultrafast laser source, such as a femtosecond laser, is typically required for two-photon excitation.

Additionally, instead of a descanned confocal detector that is employed in traditional one-photon microscopy, a non-descanned detector can be used to collect fluorescence for high signal sensitivity. (**Figure 1-2**) Under descanned detection, the fluorescence emission is collected by the objective; returns all the way back along the excitation beam path to the dichroic mirror, and then focused to an internal photomutiplier (PMT) through a confocal pinhole. The long travel path and many optical elements that the emission light goes through can all reduce the signal actually detected by PMT. While the confocal detection system is important to reduce scattering and out of focus emission in conventional microscopy, it becomes unnecessary in 2PFM. Therefore, it is possible to collect all the emitted light of the required wavelengths. A non-descanned detection path has a dichroic mirror directly after objective lens. It provides the shortest possible light path, fewer optical elements, and no pinhole in the light path.

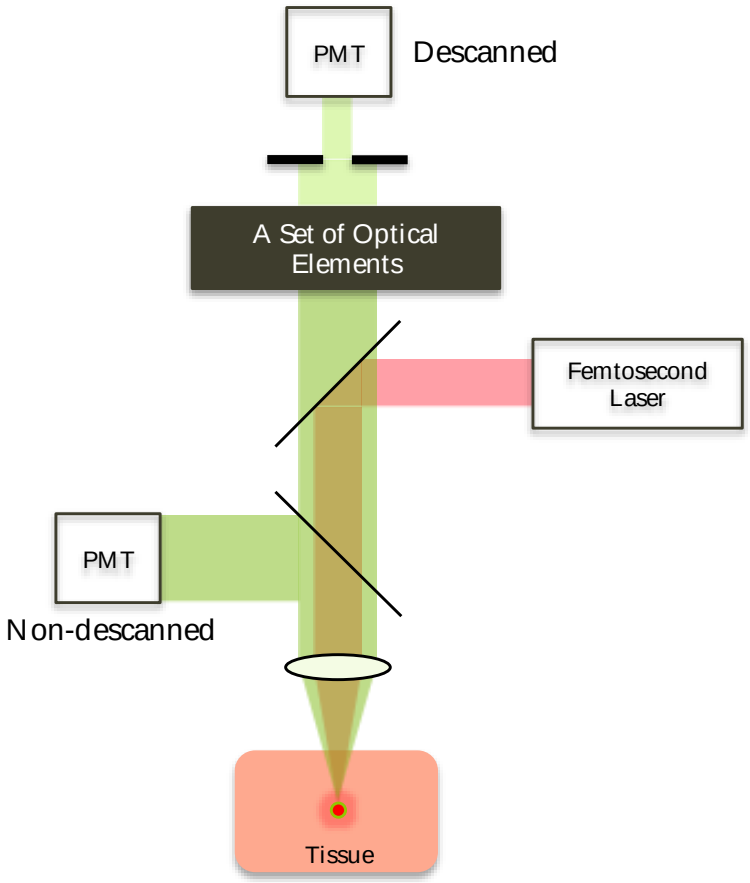

Figure 1-2. Descanned and non-descanned detection path in one-photon and two-photon microscopy.

1.3 Two-Photon Photodynamic Therapy

1.3.1 Photodynamic Therapy

Photodynamic therapy (PDT) is a treatment that uses a photosensitizer in the presence of light to produce a cytotoxic effect on cancer cells.[6] Conventional PDT involves three elements: a photosensitizer, oxygen, and light, resulting in generation of singlet oxygen to induce cell death. Currently, many photosensitizers, such as porphyrin, texaphyrin, and chlorin[19], have been used

clinically to treat skin cancer[20, 21], bladder cancer[22], lung cancer[23], rectum and anus tumors[24], etc. Promising results were also shown in the treatment of brain tumors[5, 25].

Unlike organic compounds, oxygen in the air and tissue exists in the ground state as a triplet, which is non-reactive. However, when a photosensitizer absorbs light at certain wavelength, it can be promoted to an excited state and transfer to a triplet state by intersystem crossing. The photosensitizer can then transfer its energy to oxygen and excite it into a reactive singlet state. (**Figure 1-3,** left).

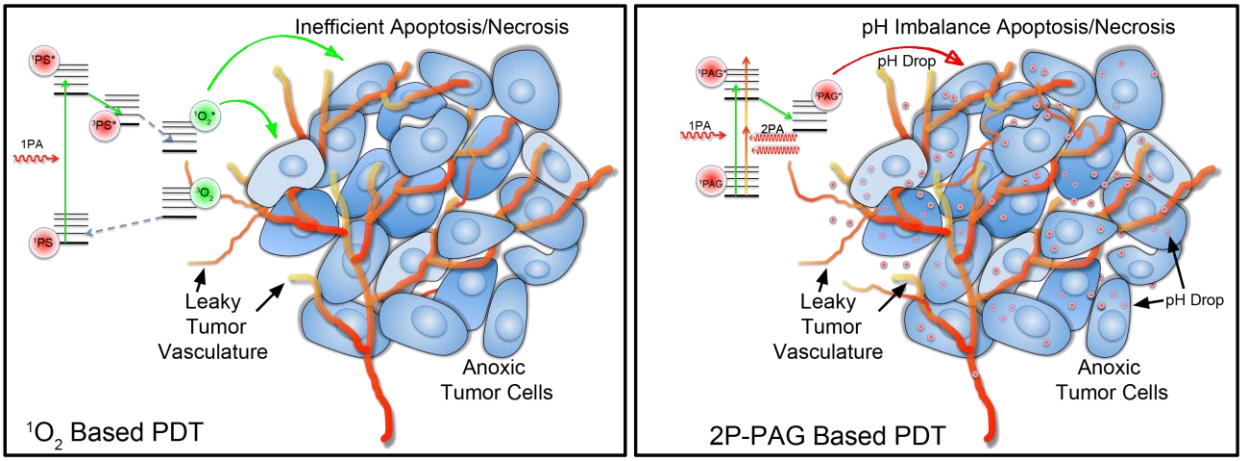

Figure 1-3. Conventional $^1O_2$ based PDT (left) and two-photon absorption photoacid generator based PDT.[7]

1.3.2 Two-Photon Photodynamic Therapy

Compared with other technologies, PDT possesses a number of advantages, such as minimally invasive, low systemic toxicity, rapid effect, and low cost. In addition, treatment can be repeated without inducing significant resistance or hypersensitivity, which is a big problem in chemotherapy. However, there are still challenges limiting its broader application. First of all,

limited light penetration in tissues prevents its application to systemic disease. Intense light incidence can also cause tissue damage. Furthermore, since the treatment is oxygen dependent, the efficiency would be difficult to increase in the hypoxia tumor system.[26-28]

A 2PA photosensitizer, on the other hand, can be excited with longer wavelength in NIR region, which provides deeper penetration and less damage by incident light. Additionally, 2PA has a quadratic dependence on the intensity of the incident light, affording high spatial localization.[29-31] This advantage can be equally exploited in PDT applications and achieve higher treatment efficiency with lower incident power. At the same time, the strict spatial selectivity is also helpful in many treatments for precision, such as treatment of brain tumors, reducing collateral damage.

The limitation of oxygen-dependent efficiency can be overcome by applying a new type of PDT, photoacid generator-based PDT. The concept of this new PDT paradigm is to induce cell death by causing a pH imbalance in the cell. Specifically, the photoacid generator can be excited by 2PA, resulting in generation of strong acid. It is hypothesized that this can cause a fast drop of cell pH and induce cell apoptosis or necrosis.[7] (**Figure 1-3**)

1.3.3 Two-Photon Absorption Photosensitizer (2PA PS)

Higher light absorption efficiency can generate more triplet state to induce singlet oxygen. Therefore, similar as 2PA dyes, 2PA photosensitizers are also preferred to have high 2PA cross-sections. Longer wavelength absorption is also favorable for deeper penetration and lower thermal damage by incident light. This is especially important for treatment of lesions under skin while keeping the top healthy tissue intact.

The efficiency of a photosensitizer can be determined by measuring its singlet oxygen quantum yield. This shows the efficiency of an excited photosensitizer to generate singlet oxygen.

Some photosensitizers also undergo fluorescence after excitaton. This could be clinically useful as fluorescence can help define and adjust treatment fields[32]. Sometimes the fluorescence spectra of a photosensitizer are different between benign and malignant regions, which can help prevent therapy to normal, healthy tissues[33]. Theoretically, the sum of fluorescence and PDT is fixed and limited by the 2PA cross-section of the photosensitizer. Therefore, the photosensitizer with a higher fluorescence quantum yield will have a lower singlet oxygen quantum yield. Thus, a balance needs to be maintained between fluorescence and singlet oxygen generation for a good photosensitizer.

In addition, a qualified photosensitizer should have low cytotoxicity in dark; otherwise the healthy tissue without PDT treatment will undergo cell death as well. Water solubility is another consideration since the photosensitizer needs to function in biological systems. For clinical use, a water-soluble agent can easily travel through the body.[19] Delivery systems can be applied to help carry photosensitizer into water. However, for PDT treatment, drug release would be another concern. A delivery system for PDT should be either biodegradable or responsive to pH, temperature, or other stimuli after being endocytosed.[34]

1.4 Fluorene Structure and Properties

1.4.1 Structure-Property Relations

Fluorescent chromophores can be classified based on its substitution pattern[35] (**Figure 1-4**). Different structures lead to different photophysical properties. Thus, desirable properties, such as high 2PA cross-section, high fluorescence quantum yield, and long excitation wavelength, can be achieved by structural design.

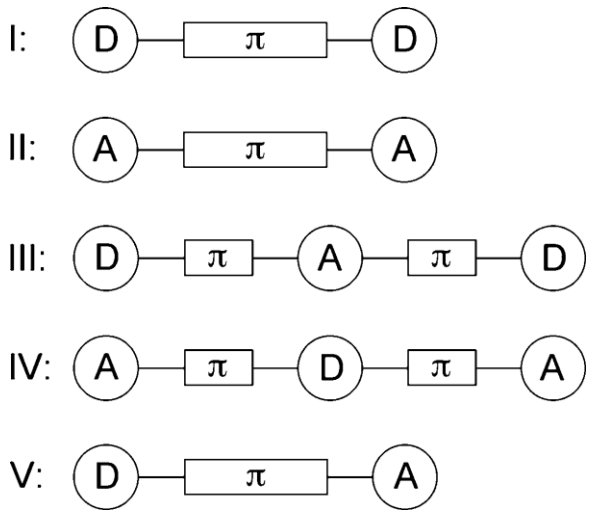

Figure 1-4. Schematics of various linear chromophores classified based on the substitution pattern. (D = donor group; π = π-conjugated bridge; A = acceptor group)[35]

Molecules with electron-rich groups at the termini of the conjugated bridge (**Figure 1-4**, I) often exhibit an increase in the 2PA cross-section compared with those without substitution, with possibility that the 2PA band can also shifts to a longer wavelength.[36, 37] When electron withdrawing groups are in the center of the π conjugated bridge (**Figure 1-4**, III), the 2PA cross-

section can be even larger.[36] In addition, extending the π-conjugated bridge can also lead to an increase in 2PA cross-section, as well as a red shift of the 2PA maximum.[37]

When electron-rich and –poor groups are substituted at the opposite termini of a π-conjugated bridge (**Figure 1-4**, V), a dipolar chromophore is formed. Dipolar chromophores always have the lowest energy 2PA band at the wavelength two times that of the one-photon absorption band. [35] The 2PA cross-section of dipolar molecules can also increase with the length of conjugation.[38] The strength of substituents can also influence the 2PA cross-section. A stronger electron donor group is expected to yield a higher cross-section than a weaker substituent.[38, 39]

The influence of the π-conjugated bridge has more complicated effects other than the length. Large 2PA cross-sections are sometimes achieved when chromophores containing triple bonds are employed compared with double bonds.[40, 41] The type of π-conjugated bridge can also determine the position of the 2PA band. However, changes in the 2PA cross-section and position due to a π-conjugated bridge are hard to predict in most cases. [35]

1.4.2 Fluorene and Fluorene Derivatives

Fluorene derivatives are characterized by their high fluorescence quantum yield.[1] The fluorene core has been largely applied in both quadrupolar (**Figure 1-4**, I-IV) and dipolar (**Figure 1-4**, V) systems, resulting in large 2PA cross-sections, due to its rigid, planar system (**Figure 1-5**), which induces large electron delocalization and serves as a stable π-conjugated bridge system.[1, 42]

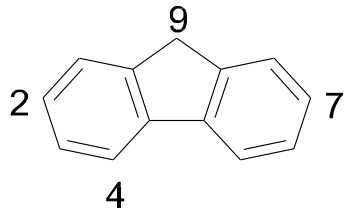

Figure 1-5. Structure of the fluorene core.

The fluorene core structure can be readily functionalized in position 2, 4, 7 and/ or 9 (**Figure 1-5**). Substitution at positions 2, 4 and 7 can extend the conjugation length; hence result in high 2PA cross-sections.[1] Electron withdrawing or electron donating groups can be substituted on these positions to obtain D-π-D, A-π-A or D-π-A structures.[3, 7] Two fluorenes can also be applied symmetrically in one structure, resulting in D-π-A-π-D or A-π-D-π-A structures.[2] Functionalization at position 9 can introduce alkyl chains or hydrophilic groups, to achieve solubility in organic solvent or water, respectively. The substitution at position 9 does not affect the photophysical properties of the conjugation system.[1] As a result, for biological applications, targeting groups can be introduced at position 9 for selective delivery.[38]

CHAPTER 2. APPLICATION OF FLUORENE-SUBSTITUTED QUINOLIZINIUM CATIONS IN PROTEIN LABELING

New symmetrical fluorene-containing quinolizinium derivatives, 2,8-bis((E)-2-(7-(diphenylamino)-9,9-dihexyl-9H-fluoren-2-yl)vinyl)quinolizinium hexafluorophosphate (QF **1**) and 2,8-bis((E)-2-(7-((7(diphenylamino)-9,9-dihexyl-9H-fluoren-2-yl)ethynyl)-9,9-dihexyl-9H-fluoren-2yl)vinyl)quinolizinium hexafluorophosphate (QF **2**), were synthesized and characterized. Though the new dyes were highly fluorescent in nonpolar solvents, they were essentially non-fluorescent in polar media. However, they exhibited fluorescence turn-on behavior upon binding to bovine serum album (BSA) protein, exhibiting over four-fold fluorescence enhancement. BSA binding constants were 1.1×10^5 M^{-1} and 3.1×10^5 M^{-1} for QF **1** and **2**, respectively. The high binding affinity to proteins appeared to assist the probes to attach to cells and show bright fluorescence.

2.1 Introduction

Heteroatomic cations are widely employed in a number of areas of practical applications, including chemical synthesis,[43, 44] metal ion detection,[45, 46] photodynamic therapy,[47-49] optical power limiting,[50-52] and one- and two-photon fluorescence bioimaging microscopy.[53-55] The use of cationic structures as a fluorescent probe, in turn, is concerned with various biomedical techniques, such as fluorimetric detection of DNA and proteins[56-58] and efficient staining agents of organelles in the cytoplasm[59, 60] Such applications are based on fundamental investigations of the linear photophysical and nonlinear optical properties of the charged organic molecules,

including fast dynamic processes in the ground and excited electronic states.[61-63] One of the most intriguing types of cationic structures is a quinolizinium derivative with general D-π-A^+ and D-π-A^+-π-D structures,[53, 64] where A^+ is a charged cationic electron deficient core and D represents electron-donating substituents. A new V-shaped quinolizinium derivative of this type, (*E*,*E*)-2,8-bis(4-N,N-dimethylaminophenylvinyl) quinolizinium hexafluorophosphate (V-DMA2), was shown as a promising marker for fluorescence microscopy of live cells, exhibiting a large two-photon absorption (2PA) cross section and dramatic increase in fluorescence intensity upon binding to DNA.[53]

Linear spectroscopic and excited-state deactivation processes of a series of benzo[*b*]quinolizinium derivatives were reported as highly sensitive "light-up" fluorescence probes for DNA and protein detection.[46, 57, 58, 65] The nature of ultrafast relaxations in the excited state of naphto[1,2-*b*]quinolizinium bromide and its interaction with DNA were probed by femtosecond transient absorption spectroscopy.[66] It is worth mentioning that fast relaxations in the excited state of quinolizinium derivatives are scarcely addressed in the scientific literature; therefore, this is a subject of keen interest as is increasing their 2PA efficiency, a challenging task.

Membrane proteins are of great importance in cell function. They are at the interface between cytoplasm and extracellular space. Most membrane proteins function in transport or signaling or provide the structural framework that shapes cellular compartments.[67] Among these membrane proteins, vinculin, a membrane-cytoskeletal protein, is located in focal adhesions as well as cell-adherence junctions, and plays important role in cell adhesion and migration.[68, 69]

In this chapter, the synthesis and comprehensive investigation of linear spectroscopic is reported and potential uses of the new probes were explored, resulting in turn-on fluorescence behavior upon binding to BSA in an aqueous medium. Based on this propensity, one of the probes was applied for cell imaging. Upon incubation, bright fluorescence was observeed in cell membranes, exhibiting large colocalization with vinculin.

2.2 Materials and Methods

2.2.1 Synthetic Strategy

The syntheses of quinolizinium dyes are shown in **Schemes 1** and **2**.

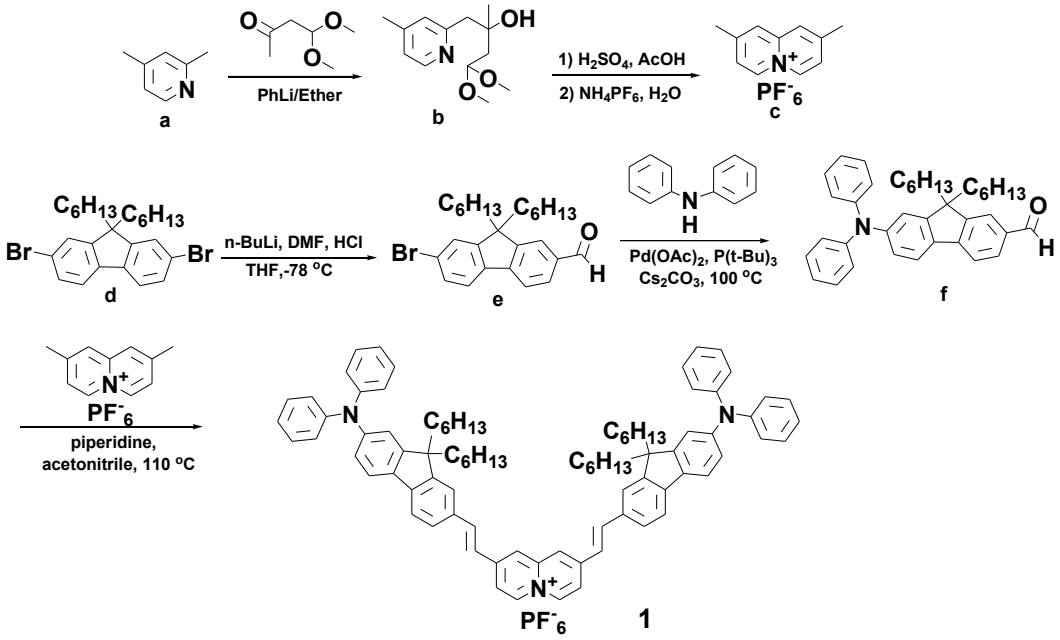

Scheme 2-1. Synthesis of bis-fluorenyl quinolizinium QF **1**.

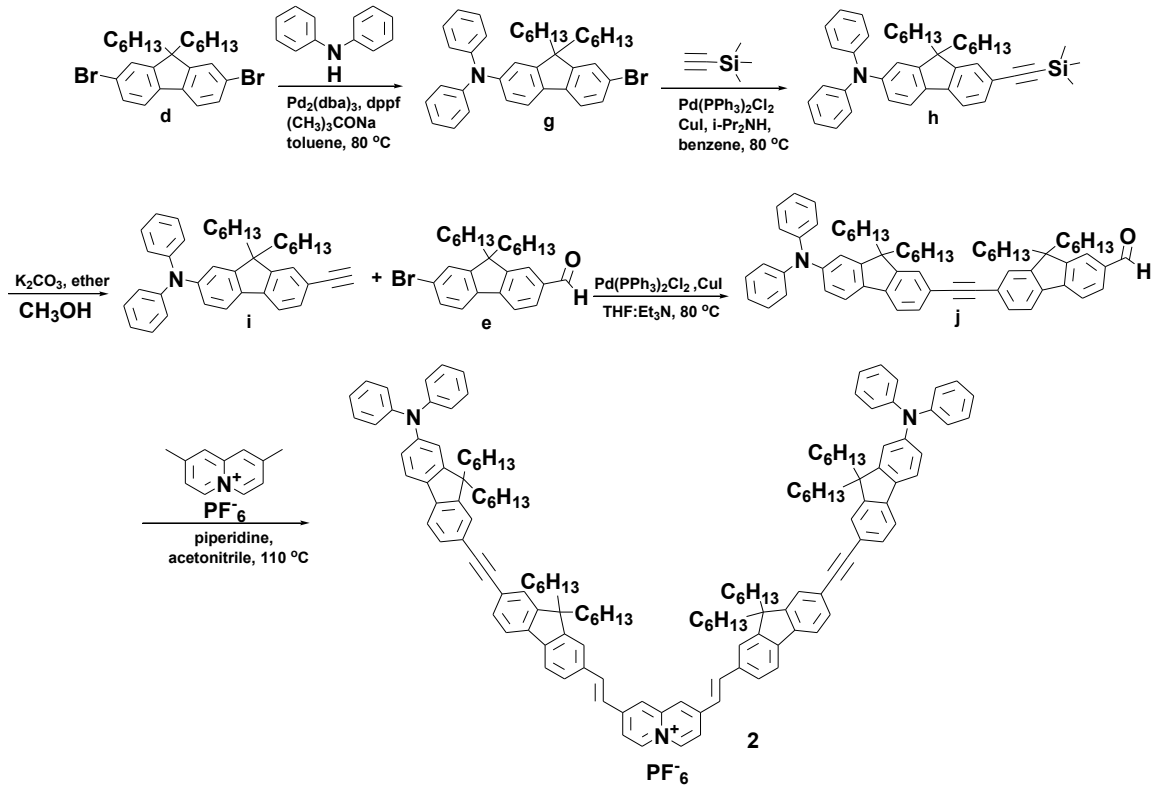

Scheme 2-2. Synthesis of tetra-fluorenyl quinolizinium QF **2**.

2.2.2 BSA Binding Experiment

Quinolizinium in 1:1 H_2O/DMSO mixture (3 mL) was placed in a quartz cell while increasing concentrations of BSA were added. The final concentration of quinolizinium was kept constant at 2.5 μM while the concentration of BSA was varied from 0 – 1.5 equivalents. Fluorescence emission spectra of the quinolizinium were recorded (excitation 480 nm for **1**, and 450 nm for **2**).

2.2.3 BSA Binding Constant

BSA solution (3 mL) was placed in a quartz cuvette with increasing concentration of quinolizinium added. The final concentration of BSA was maintained at 10 μM while the

concentration of quinolizinium was varied from 10-80 μM. Fluorescence emission spectra of BSA were recorded at the same conditions in the range 300–400 nm, with excitation at 280 nm. The maximum emission intensity at 340 nm of each sample was recorded. Binding constant K_a was determined with the Scatchard equation $r/c = nK_a - rK_a$, where r is the ratio of the concentration of bound ligand to total available binding sites, which can be calculated from the quenching of maximum emission intensity,[70, 71] c is the concentration of free drug, and n is the number of binding sites for every BSA molecule. The value of K_a was obtained by plotting r/c against r.

2.2.4 Cell Imaging

For cell membrane imaging, HeLa cells (ATCC®) were seeded on poly-D-lysine coated coverslips at a concentration of $5 \cdot 10^4$ cells/mL and incubated for 48 h. A stock solution of **1** in DMSO was then diluted to 10 μM with MEM medium (Corning, Cellgro®) and added to the cells. Cells were co-incubated with dilute solution of **1** together with Alexa Fluor® 488 Conjugated Wheat Germ Agglutinin (AF-WGA, Life Technologies) for 15 min and then fixed with 4% formaldehyde. $NaBH_4$ was added twice at 1 mg/ mL for 5 min to reduce auto-fluorescence. Coverslips were mounted on slides with ProLong Gold® antifade reagent. Cell slides were imaged with a Leica SP5II microscope equipped with a Coherent Chameleon Vision S laser source (prechirped compensated, 70 fs, 80 MHz). Probe **1** and AF-WGA were exited at 458 nm and 488, respectively. Fluorescence was collected with a pinhole for confocal images in the range 700-800 nm for **1**, and 600-700 nm for AF-WGA. Images were scanned every 250 nm in z direction then processed with Amira software for 3D visualization.

For other colocalized imaging, HeLa cells were seeded on poly-D-lysine coated coverslips at a concentration of 5×10^4 cells/mL and incubated for 48 h. A stock solution of **1** in DMSO was then diluted to 10 μM with MEM medium (Corning, Cellgro®) and added to the cells. After 45 min, cells were fixed with 4% formaldehyde. $NaBH_4$ was added twice at 1 mg/ mL for 5 min to reduce auto-fluorescence. Cells were then penetrated with 0.1 % Triton-X for 10 min. Nonspecific binding was blocked with 1% BSA. For microtubule colocalization, mouse anti-α-tubulin (bovine) monoclonal antibody (Invitrogen) was added at 0.2 μg/well for 1 h, followed by FITC-anti-mouse IgG (Sigma-Aldrich) 2 μg/well for another 1 h. For actin filaments colocalization, Alexa Fluor 532 conjugated phalloidin (Invitrogen) was added at 1 unit/well. For vinculin colocalization, mouse anti-vinculin monoclonal antibody (Calbiochem) was added at 0.2 μg/well for 1 h, followed by FITC-anti-mouse IgG (Sigma-Aldrich) 2 μg/well for another 1 h. Coverslips were then mounted on slides with ProLong Gold® antifade reagent. Microtubule and vinculin colocalization slides were imaged with an Olympus IX70 DSU microscope. Actin filament colocalization slides were imaged with a Leica SP5II microscope equipped with a Coherent Chameleon Vision S laser source.

2.3 Results

2.3.1 Spectra of QFs

Linear absorption and emission of QF **1** and **2** were investigated in cyclohexane (CHX), toluene (TOL), tetrahydrofuran (THF), dichloromethane (DCM) and acetonitrile (ACN). The

steady-state 1PA spectra of QF **1** and **2** (**Figure 2-1**, curves 1-5) exhibit two (a) and three (b) well-defined absorption maxima, respectively.

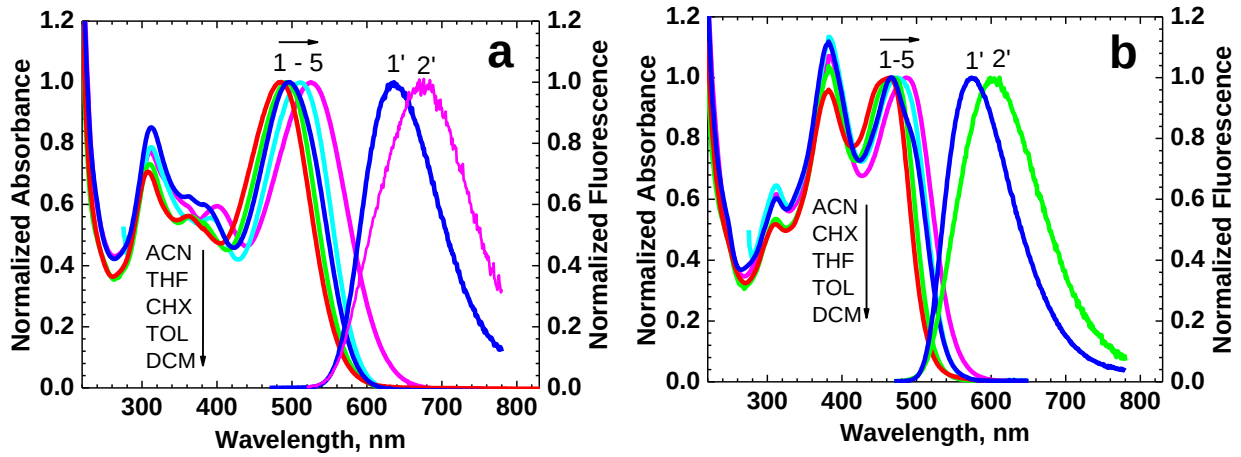

Figure 2-1. Normalized linear absorption (1-5) and fluorescence (1′-2′) spectra of 1 (a) and 2 (b) in different solvents. Fluorescence spectra in CHX (1′) and TOL (2′).

The long-wavelength absorption bands with maxima at $\lambda_{ab}^{max} \approx 463$ - 525 nm (**Tables 1, 2**) can be related to π-π* electronic transitions concerned with the positively charged quinolizinium core. These long-wavelength bands exhibited a weak solvatochromic effect and complicated dependence on solvent polarity (Δf). No monotonic dependence of λ_{ab}^{max} on Δf was detected. It is worth mentioning that the value of λ_{ab}^{max} decreases with the increase in π-conjugation length from QF **1** to **2**, which reflects a weak intramolecular electronic interaction between fluorene and quinolizinium parts and an unusual hypsochromic effect via the extension of conjugation.[72] In this case, the fluorene moieties only play a role of quinolizinium end substituents with a certain electron donating strength. The short-wavelength absorption bands at

≈ 310 nm and ≈ 380 nm (**Figure 2-1)**, which assumedly correspond to the fluorene fragments of QF **1** and **2**, were nearly independent of solvent polarity and nicely correlated with the number of fluorene units.

Table 2-1. Linear photophysical and photochemical parameters of QF **1** in solvents with different polarity Δf.

Compound	**1**				
Solvent	CHX	TOL	THF	DCM	ACN
Δf	0.000248	0.0135	0.209	0.217	0.305
λ_{ab}^{max}, nm	495 ± 1	510 ± 1	493 ± 1	525 ± 1	484 ± 1
λ_{fl}^{max}, nm	636 ± 1	673 ± 1	-	-	-
Stokes shift, nm (cm^{-1})	141 ± 2 (≈ 4480)	163 ± 2 (≈ 4750)	-	-	-
$\varepsilon^{max} \cdot 10^{-3}$, $M^{-1} \cdot cm^{-1}$	42 ± 3	43 ± 3	48 ± 3	43 ± 3	49 ± 3
Φ_{fl}, %	46 ± 5	17 ± 5	-	-	-
$\Phi_{ph} \cdot 10^{4}$	0.5 ± 0.1	1 ± 0.2	0.06 ± 0.03	0.04 ± 0.02	2 ± 0.5
τ_{fl},* ns (A_i)	3.3 ± 0.1	0.4 ± 0.1 (0.75) 1.9 ± 0.1 (0.25)	-	-	-

*Excitation wavelength, λ_{ex} ≈ 400 nm.

Table 2-2. Linear photophysical and photochemical parameters of QF **2** in solvents with different polarity Δf.

Compound	**2**				
Solvent	CHX	TOL	THF	DCM	ACN
Δf	0.000248	0.0135	0.209	0.217	0.305
λ_{ab}^{max}, nm	466 ± 1	474 ± 1	469 ± 1	486 ± 1	463 ± 1
λ_{fl}^{max}, nm	574 ± 1	604 ± 1	≈ 502 (S_2)	-	-
Stokes shift, nm (cm^{-1})	108 ± 2 (≈ 4040)	130 ± 2 (≈ 4540)	-	-	-
$\varepsilon^{max} \cdot 10^{-3}$, $M^{-1} \cdot cm^{-1}$	80 ± 3	74 ± 3	93 ± 3	83 ± 3	77 ± 3
Φ_{fl}, %	65 ± 5	26 ± 5	3 ± 0.5	< 0.5	-

$\Phi_{ph} \cdot 10^4$	3 ± 1	2.7 ± 1	0.1 ± 0.03	0.035 ± 0.01	0.86 ± 0.3
τ_{fl},* ns (A_i)	2.8 ± 0.1	1.5 ± 0.1	-	-	-

*Excitation wavelength, $\lambda_{ex} \approx 400$ nm.

Degenerate 2PA spectra of symmetrical fluorene-containing quinolizinium structures QF **1** and **2** were obtained in a broad spectral range by an open-aperture Z-scan technique[73] and are shown in **Figure 2-2**. At least three well-defined 2PA maxima were observed for the simpler compound QF **1** (**Figure 2-2**, a), and the most intensive one with $\delta_{2PA} \approx 500$ GM is sufficiently close to the main 1PA contour. In the case of the more complicated compound **2,** a broad 2PA spectrum with $\delta_{2PA} \approx 400$ - 600 GM was observed (**Figure 2-2**, b), and the same nature of two-photon transitions can be assumed.

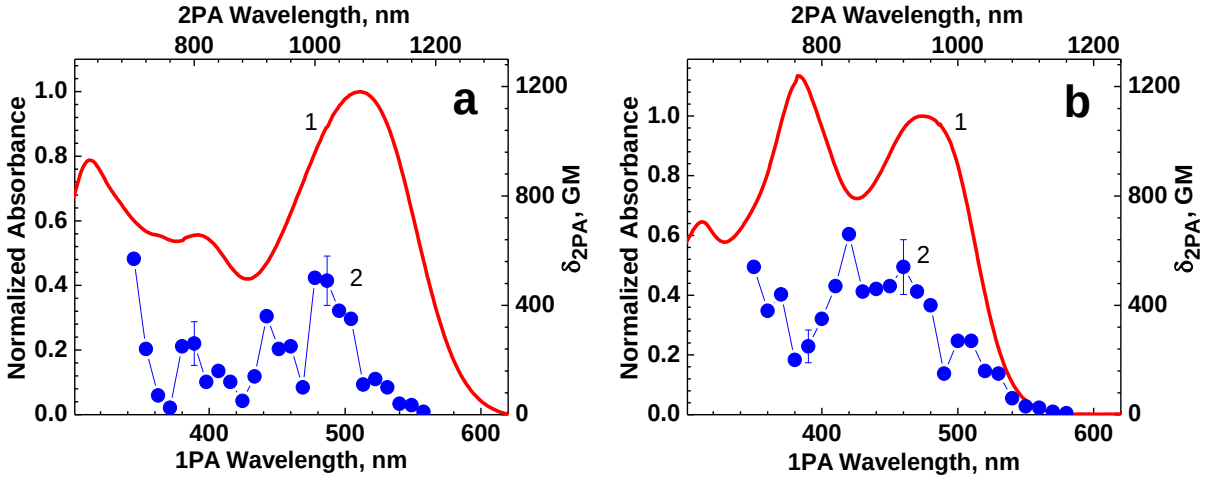

Figure 2-2. Normalized 1PA (1) and degenerate 2PA (2) spectra of 1 (a) and 2 (b) in TOL.

2.3.2 Increase of Fluorescence Emission of QFs with BSA Binding

It was reported that quinolizinium derivatives can bind with biomacromolecules such DNA and proteins, exhibiting a fluorescence turn-on effect.[58, 74] Therefore, binding of QF **1** and **2** was investigated. Increase of fluorescence emission was observed for both quinoliziniums (**Figure 2-2**).

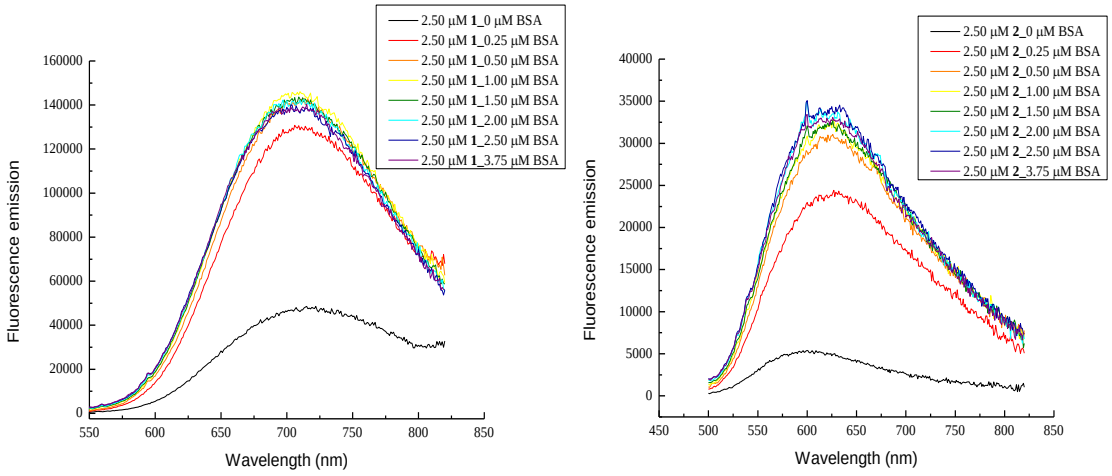

Figure 2-3. Fluorescence emission of quinolizinium dyes was increased dramatically with increase of BSA concentration.

Combining BSA with each of the quinolizinium salts also resulted in a severe decrease of fluorescence emission from BSA at 340 nm (**Figure 2-3**), indicative of the binding of quinolizinium to BSA. A Scatchard plot was performed to calculate BSA binding constants; values of 1.1×10^5 M^{-1} and 3.1×10^5 M^{-1} were obtained for QF **1** and **2**, respectively. According to the binding constants, QF **2** exhibited a higher binding efficiency than **1**. However, poor solubility in DMSO prohibited further study of QF **2** in cell imaging.

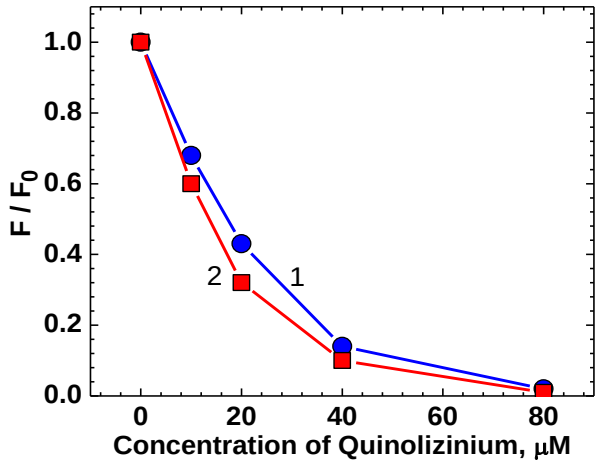

Figure 2-4. Quenching curves of BSA (λ_{ex} : 280 nm, λ_{em} : 340 nm) by binding with QF **1** (1) and **2** (2) at different ratios. F and F_0 are the intensities of BSA fluorescence emission with and without binding, respectively.

2.3.3 Cell Imaging

Cells exhibited bright fluorescence at the wavelength range corresponding to emission of QF **1** (**Figure 2-4**). 3D visualization suggested that the observed fluorescence of **1** was localized on cell membranes. Fluorescently-labeled wheat germ agglutinin (WGA) is used to detect glycoconjugates on cell membranes by selectively binding to N‑acetylglucosamine and N‑acetylneuraminic acid residues (**Figure 2-4**, C).[75] Hence, a co-incubation experiment was performed to assess if QF **1** was localizing on cell membranes. Overlay of two dyes (Alexa Fluor® 488-WGA and QF **1**, **Figure 2-4**, D) indicates that QF **1** may localize on the cell membrane but bind with different membrane components than WGA. Considering the low emission efficiency of **1** as a free dye in DMSO-H_2O mixture (**Figure 2-2**), bright fluorescence

from QF **1** (Figure 14, B) supports that QF **1** enhanced its fluorescence upon binding with cell membrane proteins.

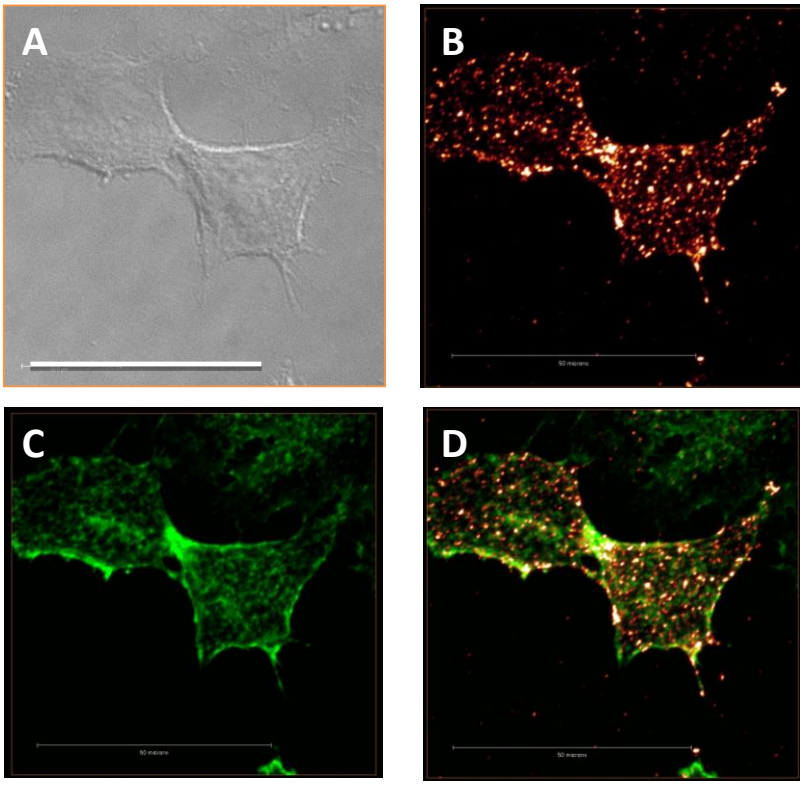

Figure 2-5. DIC (A) and Fluorescent (B, C) images of HeLa cells co-incubated with 1 (B) and Alexa Fluor® 488-WGA (C). Fluorescent images were scanned every 250 nm at z direction and then processed with Amira software. D shows the overlay image of B and C. Scale bar indicates 50 μ.

Co-incubation of QF **1** with anti-α-tubulin antibody, phalloidin, or anti-vinculin shows different degrees of overlay overlap (**Figure 2-5**). Among the three proteins examined, the distribution of **1** appears to be more associated to vinculins (**Figure 2-5**, I).

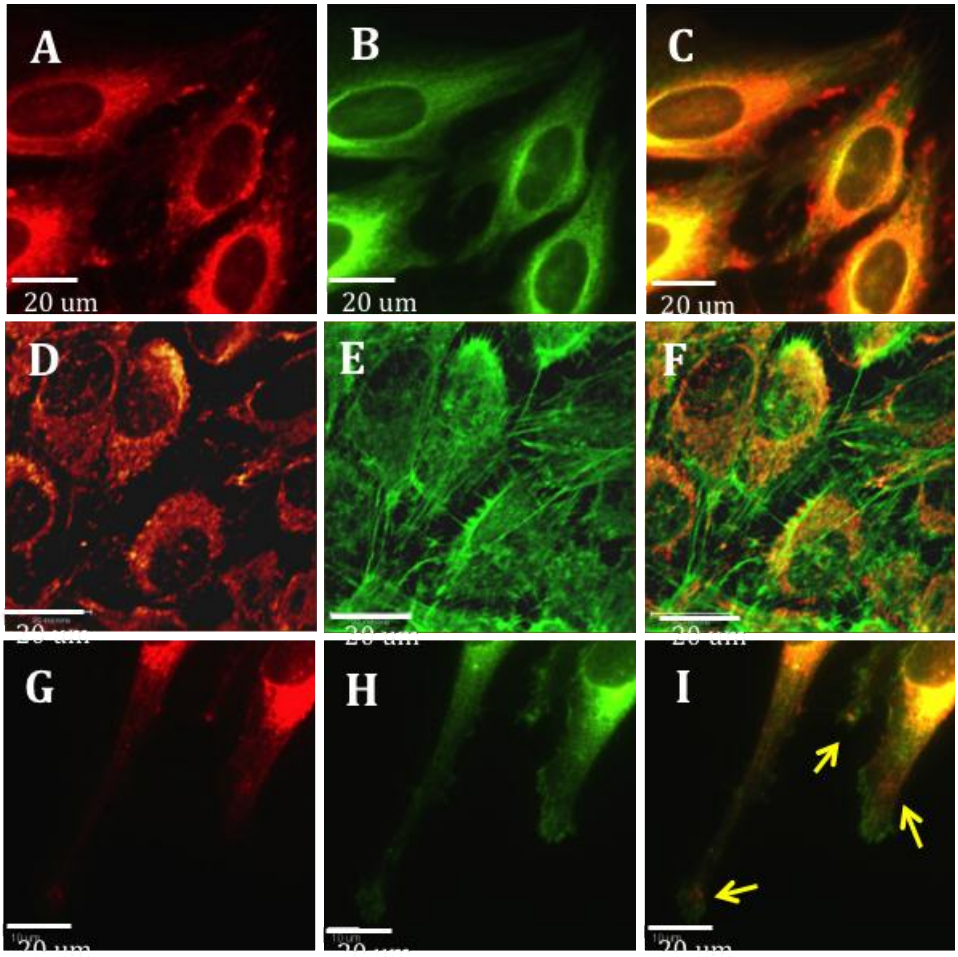

Figure 2-6. Colocalization of **1** (A, D, G) with microtubule (B), actin filaments (E) and vinculin (H) in HeLa cells. Different degrees of overlay (C, F, I) were observed between **1** and three proteins. Distribution of **1** appears to be more associated to vinculins (arrows in I), indicating possible binding between **1** and vinculins. Scale bars are 20 μm.

2.4 Discussion

Linear and non-linear photophysical properties of new fluorene-containing symmetrical quinolizinium derivatives QF **1** and **2** were investigated. The electronic structures of the new quinolizinium fluorene-containing derivatives can be presented as D-π-A^+-π-D type molecules with different π-conjugation lengths (**Schemes 2-1, 2-2**). The steady-state fluorescence,

excitation, spectra revealed the nature of the dual-band fluorescence emission of QF **2** and the complex electronic structure of the main long-wavelength absorption band. The short-wavelength fluorescence band of QF **2**, with maximum at ≈ 425 nm, was attributed to emission from a higher excited electronic state S_n, which is evidence of Kasha's rule violation for this molecular type.

Symmetrical cations QF **1** and **2** exhibited different contours of degenerate 2PA spectra with maximal cross sections δ_{2PA} ≈ 400 - 600 GM and an extended full width at half maximum of the more complicated compound **2**. In contrast to the previously reported quinolizinium derivative V-DMA2,[53] fluorene-containing QF **1** and **2** exhibited a totally different shape of 2PA spectra. New molecules QF **1** and **2** are not centrosymmetric and exhibit relatively large 2PA cross-sections, δ_{2PA}, in the spectral range of the main long-wavelength linear absorption bands.

Linear absorption spectra of QFs exhibited a weak and rather complicated dependence on solvent polarity. However, the fluorescence of QF **1** and **2** showed great dependence on solvent polarity. With quantum yield as high as 46% and 65% in nonpolar solvent CHX, the fluorescence of QF **1** and 2 was not detectable in polar solvent ACN. This is not a favorable property for fluorescence microscopy application.

It was reported that quinolizinium derivatives can bind with biomacromolecules such DNA and proteins, exhibiting a fluorescence turn-on effect, because of a restricted conformation flexibility [58, 74] Similar effects were observed with QF **1** and **2**. Though not fluorescent in polar media, the dyes exhibited noticeable fluorescence turn-on behavior upon binding BSA, exhibiting over four-fold fluorescence enhancement. The fluorescence stopped increasing after ratio of dye to BSA reached around 0.4 - 0.5. When plotted for quenching of BSA florescence

with Stern-Volmer curves ($F_0/F \sim c$), both QFs gave a nonlinear relation (data not shown). These results indicate the binding of QFs and BSA is not in a 1:1 ratio. It could be assumed, according to the binding results, that one QF molecule may bind with more than one BSA molecule. A similar BSA quenching pattern was reported with other quinolizinium structures,[58] however, a detailed binding mechanism has not been yet elucidated. Further studies are necessary to determine the binding sties and binding pattern of these new quinoliziniums. Since Stern-Volmer plots are applied for linear stoichiometric binding,[58, 76, 77] a different method, Scatchard plot analysis, was employed to determine the BSA binding constant.[70, 71] Both QFs showed strong affinity to BSA and sufficient fluorescent increase upon binding. This solved the problem of low fluorescence in polar solvents and supported their further application in bioimaging.

Taking into account the relatively high fluorescence quantum yield of QF **2** (≈ 0.65), large 2PA cross sections, and nice overlap of its 2PA spectrum with the tuning range of Ti:sapphire lasers, it was expected that this compound will have high potential in fluorescence microscopy applications. However, the low solubility of QF **2** in DMSO led to difficulty in getting a sufficient concentration in the cell culture system. Additionally, although QF **2** showed greater fluorescence increase with BSA binding (**Figure 2-3**), the final fluorescence intensity it could reach was still low compared with QF **1** at the same concentration. QF **1**, on the other hand, presented good solubility in DMSO, and efficient increase of fluorescence intensity with BSA binding. Hence, QF **1** was selected for further investigation in cell imaging.

Fluorescence was detected on cell membranes (**Figure 2-5**). Considering the low fluorescence intensity of QF **1** in polar solvents (**Table 2-1**) and DMSO-H_2O mixtures (**Figure 2-3**), the bright fluorescence exhibited on cell membrane indicates the turn-on effect of QF **1** by

a restriction of conformation flexibility upon binding with certain biomacromolecules on cell membrane (likely cell membrane proteins. Co-incubation of QF **1** with a membrane probe, Alexa Fluor® 488 conjugated WGA, which can bind to N- acetylglucosamine and N- acetylneuraminic acid residues on cell membrane, showed that fluorescence of QF **1** located generally in the same regions as WGA, but in somewhat different positions. Therefore, QF **1** was possibly bound to some biomacromolecules other than N- acetylglucosamine and N- acetylneuraminic acid residues on the cell membrane. Considering the high binding affinity of QF **1** with BSA and existence of large amount of proteins on cell membranes, it can be assumed that QF **1** bound to certain proteins on the cell membrane. Thus, additional proteins were examined aa described below.

Vinculin is a membrane-cytoskeletal protein located in focal adhesions as well as cell-adherence junctions. It plays important role in cell adhesion and migration.[68, 69] As an important link between actin cytoskeleton and the transmembrane receptors, integrin was surrounded by multiple proteins such as talin and F-actin[78], with a very complex binding pattern.[79] Activation of this protein leads to the exposure of several binding sites, which interacts with surrounding proteins and transfers signals related to cell adhesion and migration.[79] Probe QF **1** exhibited a certain degree of overlay with vinculin, indicating that QF **1** was likely to bound to vinculin or its surrounding proteins. Co-incubation of QF **1** with microtubule and actin filament probes showed little overlap, which excludes the possibility that QF **1** bound to these two proteins. It is difficult to conclude whether the association of QF **1** and vinculin suggests a specific binding relationship. However, highly specific distribution in the membrane adjacent vinculin suggests

the promising application of QF **1** in cell membrane imaging. Further studies would be necessary to better take advantage of this probe.

2.5 Conclusion

Advantageous linear photophysical and photochemical properties, reasonable 2PA cross sections, and nice overlap of the 2PA spectra with the tuning range of commercial ultrafast lasers, suggested the potential of the new quinolizinium derivatives for laser scanning fluorescence microscopy applications. High BSA binding and bright membrane-localized fluorescence images of HeLa cells confirmed this and may be the subject of future studies.

CHAPTER 3. APPLICATION OF INTEGRIN TARGETING FLUORENE-SUBSTITUTED PYRAN DYES IN TUMOR VASCULATURE IMAGING

Application of targeting peptides in tissue imaging can afford better selectivity and deeper penetration. RGD, a small peptide that contains adjacent L-arginine (R), glycine (G) and L-aspartic acid (D), is widely applied for targeting vessels. Herein, the enhancement of tissue image quality with RGD conjugates was investigated with two new pyran dyes. The dyes employed were 2-(2-methane-6-(2-(7-(diphenylamino)-9-propanoic acid-9-ethyl polyethyleneglycol-9**H** -fluoren-2-yl)vinyl)-4**H** -pyran-4-ylidene)malononitrile (PF **1**) and 2-(2,6-Bis((**E**)-2-(7-(diphenylamino)-9-propanoic acid-9-ethyl polyethylene glycol-9**H**-9',9'-methyl polyethylene glycol-9'**H**-fluoren-2-yl)vinyl)-4**H** -pyran-4-ylidene)malononitrile (PF **2**). Linear and nonlinear photophysical properties were comprehensively characterized. Cell and tissue images were then taken and examined. Deep penetration and high contrast were observed with the pyranyl RGD-conjugates.

3.1 Introduction

Intravital imaging techniques have provided unprecedented insight into tumor microcirculation and microenvironment, allowing quantitative evaluation of tumor blood vasculature, functional lymphatics, and other microenviroment characterization.[80] These techniques are supported by different new imaging methods, such as two-photon fluorescence microscopy (2PFM). 2PFM is able to achieve high resolution, deep penetration images by using

near infrared (NIR) short-pulsed light. Therefore, 2PFM has been applied in many areas, including cancer research.[80-83]

The RGD motif is found in many extracellular matrix proteins and able to recognize integrin expressed on cell membranes. Among these integrins, $\alpha_v\beta_3$ is restrictively expressed on the angiogenic vasculature. As a result, linear and cyclic RGD-peptides, selective for $\alpha_v\beta_3$ integrins, have been used for various purposes such as targeting drugs specifically to tumor vasculature. [84, 85]

The 4**H**-pyran-4-ylidene structures have attracted a fair amount of attention because of their interesting optical properties. This moiety can function as an electron acceptor group with good photochemical stability. Substitution can take place at positions 2 and 6, generating a D-π-A or D-π-A-π-D structure. 4**H**-Pyran-4-ylidene derivatives are widely used in organic light-emitting diodes[86, 87], fluorescence bioimaging[2, 88, 89], and pH sensors[90]. A fluorene di-substituted 4**H**-pyran-4-ylidene derivative was reported with good properties in organic solvents. Although it exhibited poor solubility in polar solvents, it still enabled creating high quality images in biological systems, by encapsulation in silica nanoparticles.[2]

In this chapter, two similar pyranyl structures (**PF 1, 2**) were synthesized, with better water solubility to facilitate their application in biological system. Since they have fluorenyl substitutions at position 2 and 6, it is easy to increase hydrophilicity by introducing PEG groups at position 9 of the fluorene ring system. Their application in 2PFM was evaluated in Lewis lung carcinoma tumor models.

3.2 Materials and Methods

3.2.1 Structures of RGD Conjugated Pyran dyes with Fluorene Substitution (PFs)

The synthesis of pyran dyes PF **1** and PF **2**, as well as their RGD conjugates, PF **1-RGD** and PF **2-RGD**, are shown in **Scheme 3-1**.

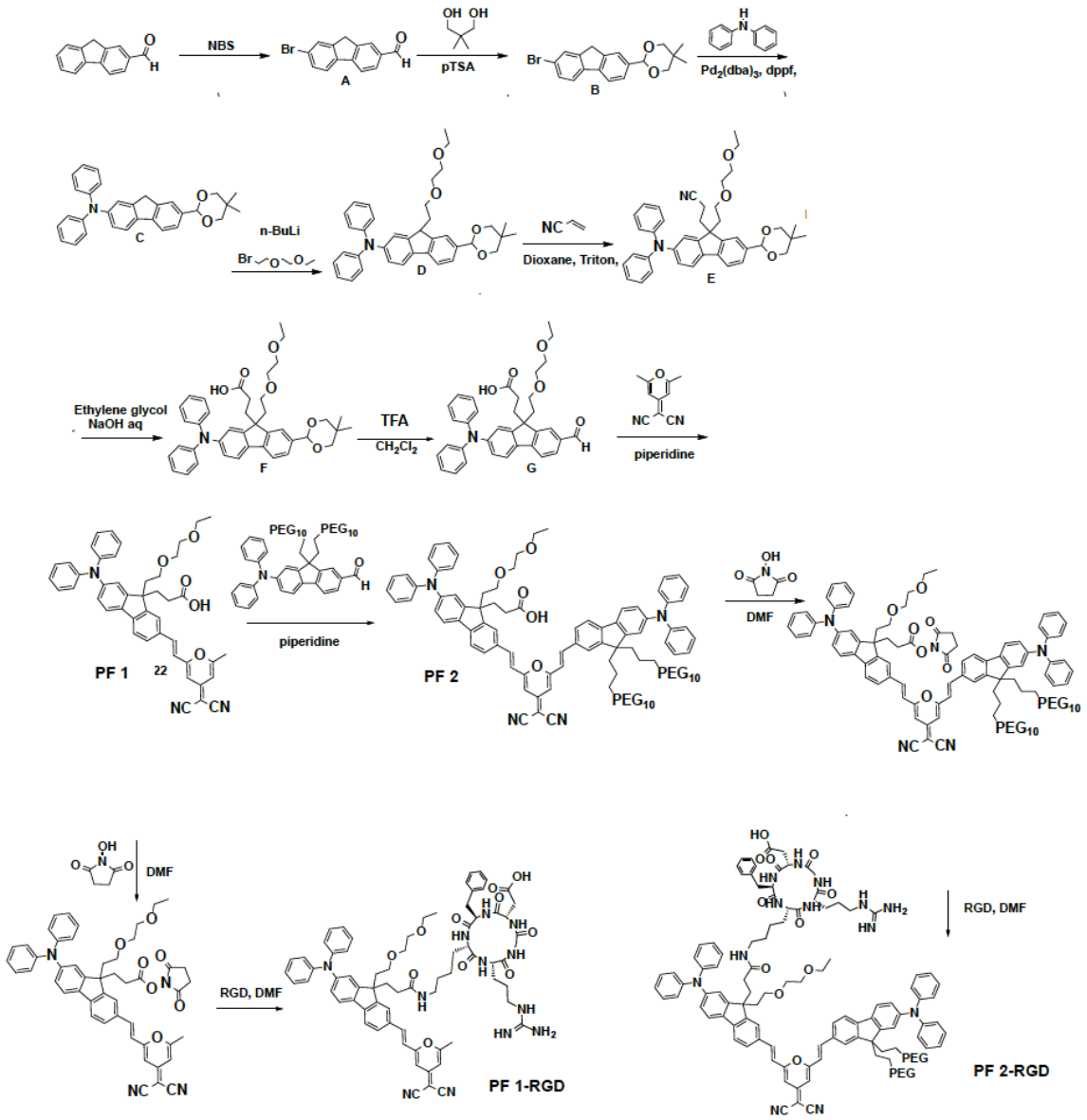

Scheme 3-1. Synthesis of PF **1**, PF **1-RGD**, PF **2**, and PF **2-RGD.**

3.2.2 Ethics Statement

All animal procedures were performed in accordance with the Office of Laboratory Animal Welfare regulations and were approved by the Sanford-Burnham Animal Care and Use Committee prior to execution.

3.2.3 Animal Model

0.5×10^6 Lewis lung carcinoma (LLC) cells were injected into the flank of C57B6 mice. After 13 days, PF **1-RGD** and **2-RGD** was injected intravenously at 4×10^{-8} mol/mouse. Two hours later, PBS was perfused, followed by paraformaldehyde perfusion. Tumors were then dissected from mice and fixed overnight in paraformaldehyde.

3.2.4 Cytotoxicity Assay

U87MG cells were seeded in 96-well plates (Corning, USA) at a concentration of 5×10^3 cells/well and incubated for 48 h. PF **1-RGD** and **2-RGD** stock solutions were prepared in DMSO and PBS, respectively. PFs were diluted into 1.56 μM, 3.12 μM, 6.25 μM, 12.5 μM, 25 μM, and 50 μM from stock solutions. Cells were then incubated with diluted PFs for an additional 24 h. Viability was then determined with the CellTiter 96® AQueous One Solution Reagent (Promega, USA).

3.2.5 Cell Imaging

To investigate the efficiency of RGD-conjugated dye, three negative control groups were included. The MCF-7 cell line was seeded at the same concentration for the first negative control as it does not express high levels of integrin. U87MG cells pre-incubated with free RGD peptide were applied for the second negative control (saturation experiment). U87MG cells

incubated with PF **1** or **2** (unconjugated to RGD) were the third negative control. All cells were seeded on poly-D-lysin coated coverslips at the concentration of 4×10^4 cells/well and incubated for 48 h. PF **1, 2, 1-RGD,** and **2-RGD** were diluted to 10 μM from stock solutions and added to cells. One hour later, cells were washed with PBS and fixed with 4% formaldehyde solution. $NaBH_4$ solution was then applied twice at 1 mg/mL to eliminate autofluorescence. Coverslips were then mounted with ProLong® Gold antifade reagent (Invitrogen, USA). Images were taken with an Olympus IX-81 DSU microscope.

3.2.6 Tissue Imaging

Small sections of tumor tissue were cut at the edge of tumors. Images were obtained with a Leica SP5 II microscope equipped with a Coherent Chameleon Vision S laser source (prechirped compensated, 70 fs, 80 MHz). Tissues were scanned at 900 nm for two-photon imaging, starting from the cutting surface, until no more fluorescence could be observed. An external non-descanned detector (NDD) was employed to collect fluorescence emission. Scanned images were process with Amira software for 3D visualization. Quantitative analysis of images was performed with Image J software.

3.3 Results

3.3.1 Fluorescence Spectra

The one-photon absorption spectra of PF **1** and **2** exhibit two and three well defined absorption maxima, respectively. (**Figure 3-1**) The absorption spectra of PF **1** in different solvents shows similar maxima at around 330 and 450 nm. Emission of PF **1** exhibited a red shift

with increased solvent polarity. The emission maxima were at 570, 680, and 740 nm in cyclohexene (CHX), dichloromethane (DCM) and dimethyl sulfoxide (DMSO), respectively. PF **2** had poor solubility in non-polar solvents; hence photophysical properties were only measured in DMSO. The absorption spectra of PF **2** had three maxima at 310, 360, and 480 nm in DMSO. The emission maximum was at 650 nm. The short-wavelength absorption bands at ≈ 330 nm for PF **1** and ≈ 310 and 380 nm for PF **2** (**Figure 3-1)**, correspond to the fluorene fragments of PF **1** and **2**, and nicely correlated with the number of fluorene units. 2PA spectra of PF **1** in DCM and **2** in DMSO exhibited well defined maxima at about 1000 nm, with maximum 2PA cross-sections reaching 200 GM and 150 GM for PF**1** and PF**2**, respectively.

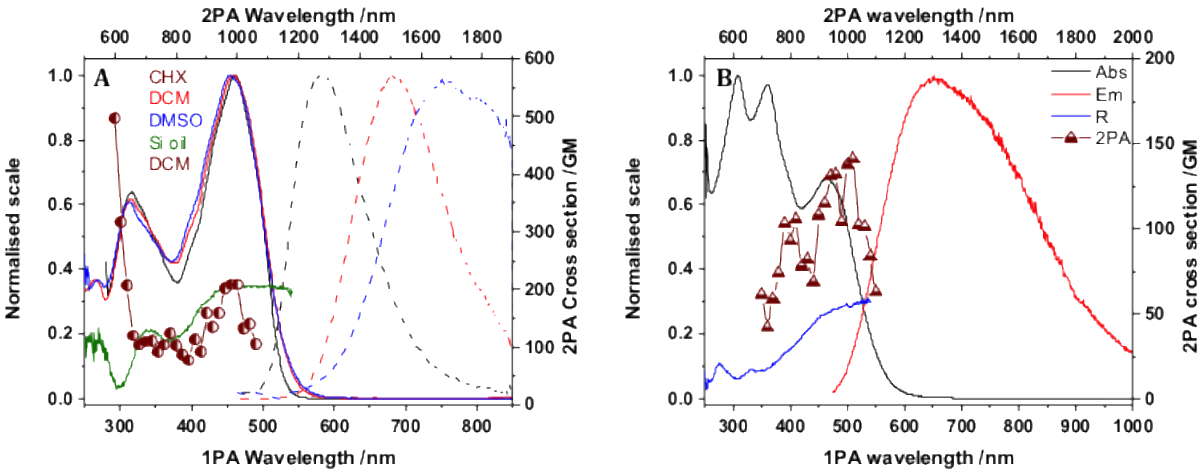

Figure 3-1. One-photon absorption, emission of PF **1** in CHX, DCM and DMSO, two-photon absorption of PF **1** in DCM and anisotropy in silicon oil (Si oil) are shown in the left spectrum (A). One-photon absorption (Abs), emission (Em), two-photon absorption (2PA) and anisotropy (R) of PF **2** in DMSO are shown in the right spectrum (B).

3.3.2 Cytotoxicity of PFs-**RGD**

Both RGD-conjugated PFs showed low toxicity below 12.5 μM. More than 80% viability of U87MG cells was observed at 12.5 μM. (**Figure 3-2**) Therefore, a concentration of 10 μM was applied for both dyes in further cell experiments.

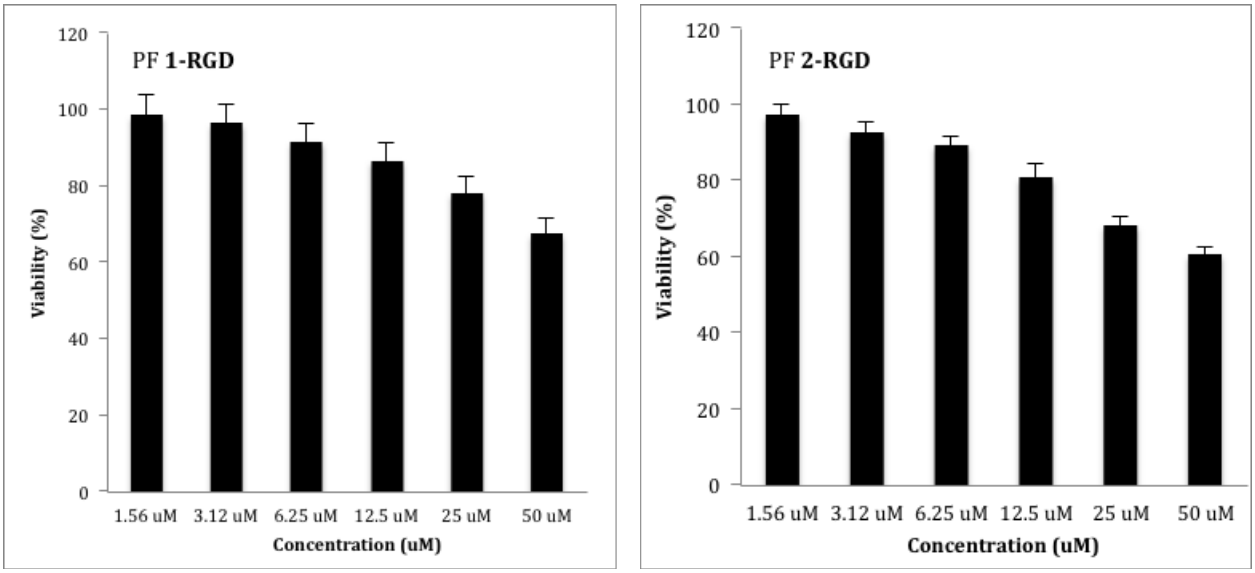

Figure 3-2. Viability of U87MG cells after 24 h incubation with RGD-conjugated PFs.

3.3.3 Integrin Targeted Cell Endocytosis

U87MG cells displayed bright fluorescence after 1 h incubation with PF **1-RGD** (**Figure 3-3**, E). The fluorescence mainly appeared adjacent to nucleus (**Figure 3-3**, F), indicating somewhat selective endocytosis. Multiple negative controls were performed to demonstrate integrin-targeting specificity. MCF-7 cells, which were reported as $\alpha_v\beta_3$ negative,[91] exhibited no noticeable fluorescence after incubation with either RGD-conjugated PFs (**Figure 3-3**, A). U87MG cells incubated with free RGD before incubation with the RGD-conjugated PFs

also exhibited low fluorescence (**Figure 3-3**, C), indicating blocking (saturation) of $\alpha_v\beta_3$ binding sites by free RGD prevented the uptake of the RGD conjugates. PFs without RGD conjugation were also employed to confirm the role of RGD. Although U87MG cells displayed bright fluorescence after incubation with PF **1**, the fluorescence signal exhibited a non-specific distribution (**Figure 2-4**, D).

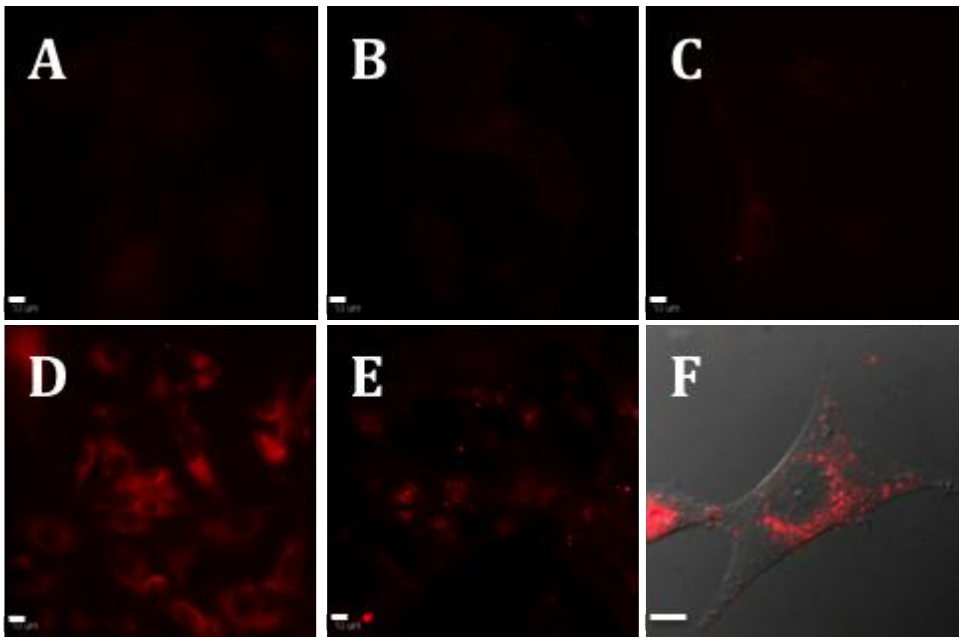

Figure 3-3. Fluorescence (A-E) and DIC overlay (F) images of MCF-7 (A) and U87MG cells (B-F) after 1 h incubation with PF **1** (D) or PF **1-RGD** (A, C, E and F). B shows U87MG cells control. Scale bars show 10 μm.

For PF **2-RGD** incubated cells, bright fluorescence was also observed around the nucleus (**Figure 3-4**, E, F), indicating selective endocytosis. Both MCF-7 cells and U87MG cells that were incubated with free RGD in advance exhibited little fluorescence (negative signal) as well (**Figure 3-4**, A, C), indicating the uptake of PF **2-RGD** requires free integrin $\alpha_v\beta_3$ receptors.

When unconjugated PF **2** was applied, no obvious signal was detected from cells (**Figure 3-4**, D), demonstrating the difficulty of PF **2** uptake without RGD-induced endocytosis.

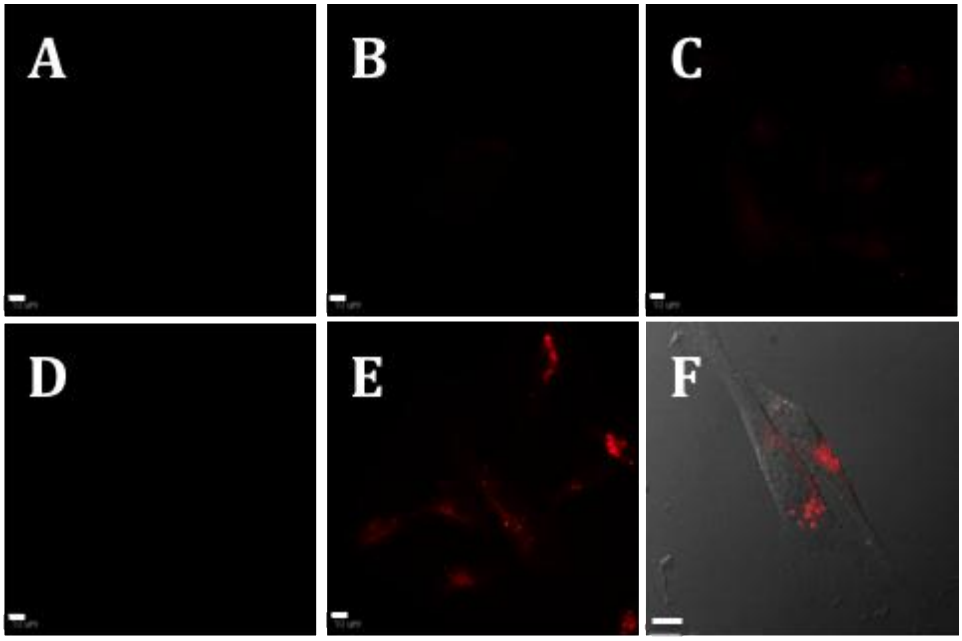

Figure 3-4. Fluorescence (A-E) and DIC overlay (F) images of MCF-7 (A) and U87MG cells (B-F) after 1 h incubation with PF **2** (D) or PF **2-RGD** (A, C, E and F). B shows U87MG cells control. Scale bars show 10 μm.

3.3.4 Integrin Targeted Tumor Imaging

Tumor tissues from mice injected with unconjugated PF **1** exhibited a certain degree of fluorescence (**Figure 3-5**, A). However, when compared with PF **2-RGD** (**Figure 3-5**, B), fluorescence intensity of PF **1** appeared to be much lower. The selectivity of PF **2** was also very weak, with many cells other than vessel endothelium lighting up in the background (**Figure 3-5**, A). On the other hand, fluorescence from PF **2-RGD** was well distributed only on vessels. This is consistent with cell imaging results of PF **1**, indicating more specific endocytosis and better

targeting with the RGD-conjugated dye. Fluorescence penetration of PF **1-RGD** (350 μm) appeared much deeper than PF **1** (200 μm). Additional evidence were shown in the cross-section images (**Figure 3-5**, C and E). Little fluorescence could be observed for PF **1** at 200 μm depth. However, PF **2-RGD** still showed bright, well defined fluorescence. Quantitative analysis of the cross-sections gave distinguished differences in both signal area and intensity.

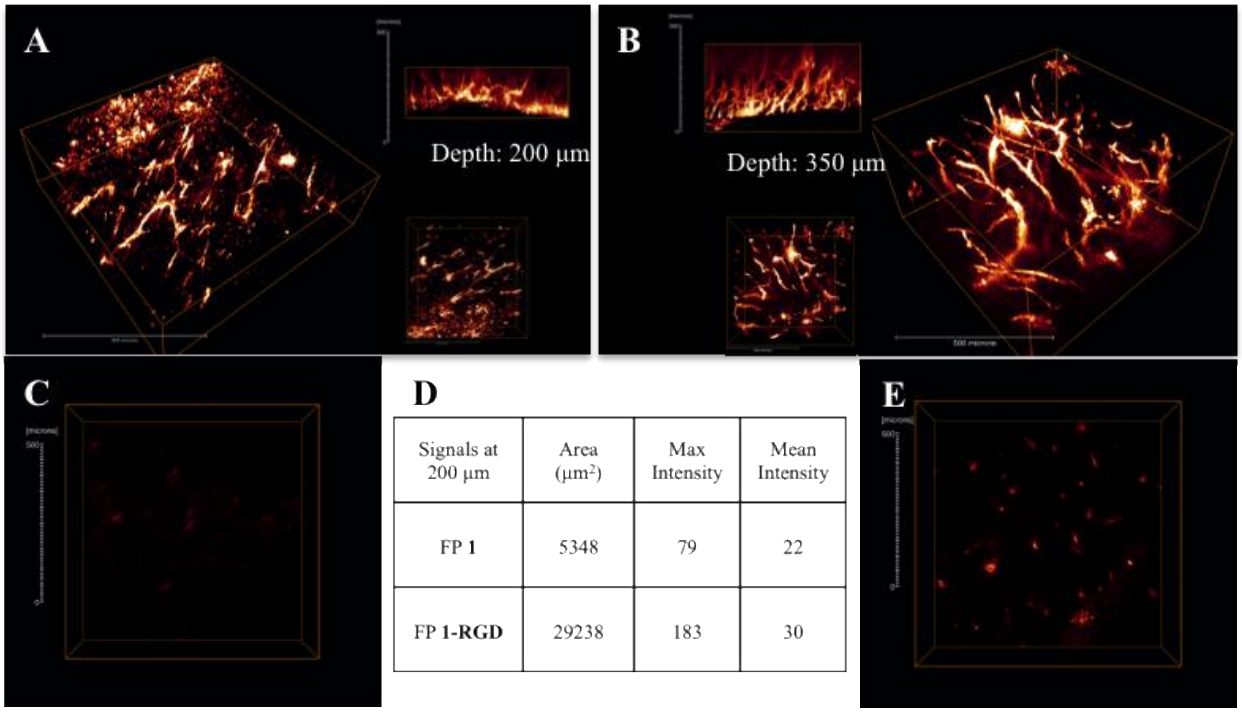

Signals at 200 μm	Area (μm^2)	Max Intensity	Mean Intensity
FP **1**	5348	79	22
FP **1-RGD**	29238	183	30

Figure 3-5. 3D reconstruction images (A, B) show the vasculature in tumor tissues from mice injected with PF **1** (A) or PF **1-RGD**. Cross-section fluorescence at 200 μm depth (C, E) were analyzed (D). Scale bars show 50 μm.

Tumor tissues from mice injected with unconjugated PF **2** exhibited very low fluorescence (**Figure 3-6**, A), while for tumors from PF **2-RGD** injected mice, the fluorescence intensity was much higher (**Figure 3-6**, B), indicating unconjugated PF **2** could not be efficiently endocytosed by the endothelium cells on vessels, consistent with results of cell imaging with PF

2. In addition, the fluorescence penetration of PF **2-RGD** was much deeper than PF **2**. The angles on the surface make the image look deeper than they actually are. Therefore, samples with similar surface angles were selected for comparison. The actual depths of observed fluorescence were 150 μm for PF **2** and 250 μm for PF **2-RGD**. Cross-sections at 200 μm are shown in **Figure 3-6**, C and E. The fluorescence from PF **2** was nearly invisible at this depth. However, PF **2-RGD** still showed bright, well defined fluorescence. Quantitative analysis of the cross-sections also support the conclusion, showing great difference in both signal area and intensity.

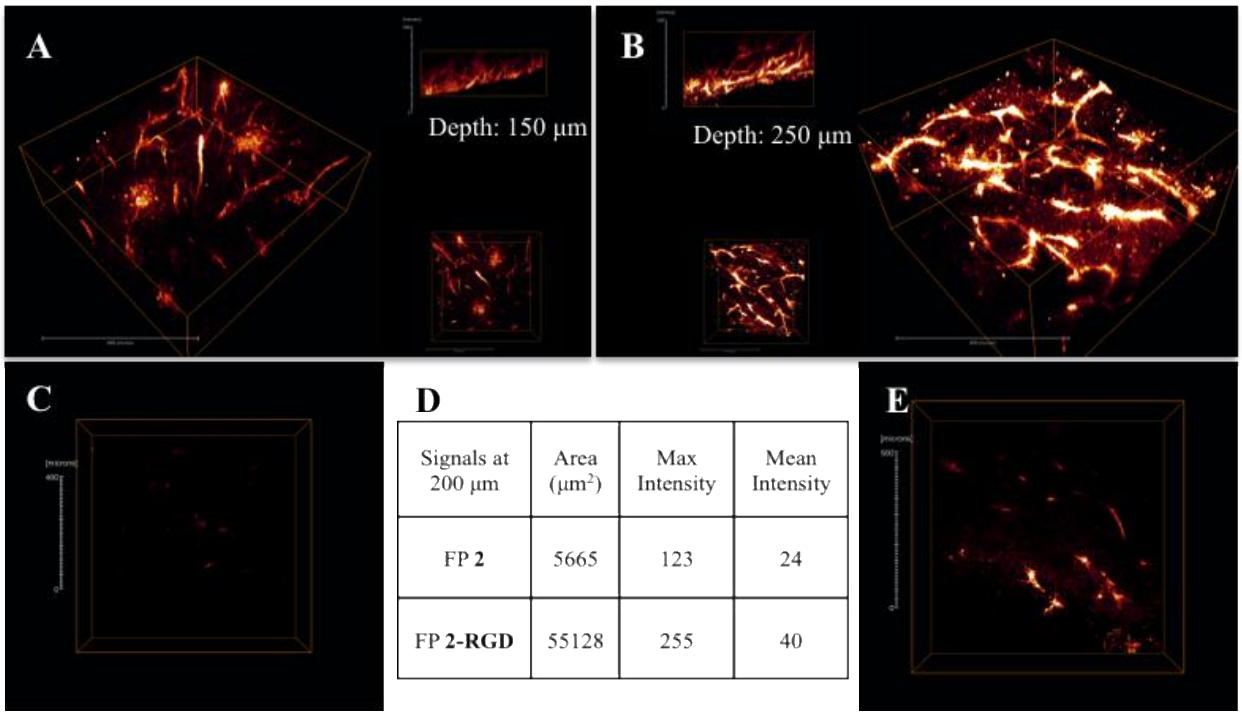

Signals at 200 μm	Area (μm^2)	Max Intensity	Mean Intensity
FP **2**	5665	123	24
FP **2-RGD**	55128	255	40

Figure 3-6. 3D reconstruction images (A, B) show the vasculature in tumor tissues from mice injected with PF **2** (A) or PF **2**-RGD. Cross-section fluorescence at 200 μm depth (C, E) were analyzed (D). Scale bars show 50 μm.

Overall, PF **1** displayed better imaging efficacy than PF **2** for both unconjugated and the RGD-conjugates. Images of PF **1-RGD** exhibited the deepest penetration (350 μm) and better selectivity to vessels.

3.4 Discussion

The two new fluorene-containing 4**H**-pyran-4-ylidene derivatives PF **1** and **2** represent D-π-A and D-π-A-π-D archetypes, respectively (**Scheme 3-1**). Linear and nonlinear photophysical properties were investigated. The 1PA absorption maxima of PF **1** didn't show a dependence on the polarity of solvent while the emission maximum underwent a red shift with increasing of solvent polarity (**Figure 3-1**, A). However, due to longer PEG chain substitution, PF **2** exhibited poor solubility in organic solvents other than DMSO. Therefore, the properties of PF **2** were only measured in DMSO. With a longer conjugated system, PF **2** had longer wavelength 1PA and 2PA bands (**Figure 3-1**, B).

The fluorene and pyran rings in PFs are able to rotate upon the axes of the olefinic double bonds, resulting in conformational flexibility. This flexibility may cause a decrease in fluorescence intensity (quantum yield). Restriction of intramolecular rotations may stiffen the molecular conformation, leading to aggregation induced emission activity. This effect can be larger with two olefinic double bonds substituted at both sides,[2, 92] affording an advantage when applying hydrophobic structures in aqueous solution. However, for hydrophilic structures PF **1** and **2**, the flexibility becomes unfavorable. Due to the hindering the long PEG chain at both fluorene substitutents, it would be hard for PF **2** to maintain a planar conformation. As a result, PF **2** shows a comparable lower 2PA cross-section than PF **1**.

Nevertheless, hydrophilic structures have their advantages for biological imaging, especially for *in vivo* imaging. In most condition, organic probes are hydrophobic and difficult to dissolve in water or other polar solvent like DMSO. To solve this problem, different delivery

systems were applied in the encapsulation of probes, such as micelles, silica nanoparticles and polymer nanoparticles.[2, 34, 88, 93] Although there are many advantages of these delivery systems, it can sometimes cause inconstancy, like size distribution. Stability is also an important issue.[94] Thus, extra quality measurements to control particle size, zeta potential, stability, etc. are necessary. Compared with these technologies, structures with hydrophilic properties are much easier in their application. In this study, PF **1** had good solubility in DMSO and PF **2** can directly dissolve in water, because of the substitution of long PEG chains. A mixture of DMSO and water was employed to mediate probes into mice circulation. Because of the toxicity of DMSO, the percentage of it should be kept at 1% or less. Thanks to high solubility in DMSO, PF **1** was able to get an adequate concentration for imaging in the final DMSO-water mixture. PF **2** was applied directly in PBS buffer. Both methods are easy to apply.

Bright fluorescence in both cell and tissue images demonstrated adequate emission intensity of both dyes in one-photon and two-photon fluorescence microscopy. Both PFs possessed decent 2PA cross-section (200 GM for PF **1** and 150 GM for PF **2**, **Figure 3-1**) and fluorescence quantum yield (2% in DMSO). RGD-targeted cell uptake appeared to increase the fluorescence intensity. The PFs also show increased fluorescence in the presence of BSA (data not shown). Thus, it is possible that proteins in cells bound to PFs resulted in the restriction of conformation or providing a more hydrophilic local environment,, increasing the fluorescence of the PFs.

Angiogenesis, the formation of new vessels from existing microcapillaries, is an important factor in the progression of cancer. It is stimulated when tumor tissues require nutrients and oxygen and triggered by chemical signals from tumor cells, causing tumor growth

and metastasis.[95] Therefore, it is of great importance to observe the activation and inhibition of angiogenesis processes. It was reported that angiogenesis is regulated by integrins, which are member of a family of cell surface receptors.[96] Among these integrins, $\alpha_v\beta_3$ integrin plays a key role in endothelial cell survival and migration and is expressed in response to angiogenic growth factors in tumor progression,[97, 98] indicating $\alpha_v\beta_3$ integrin can be a target for tumor angiogenesis. Cyclic RGDfK (c-RGDfK) peptides bind very specifically to $\alpha_v\beta_3$ integrin.[99] As a result, this peptide was introduced into the 2PA probe structures for tumor vasculature targeted imaging. Compared with structures applied without RGD, structures with RGD shows obvious advantage in tumor vasculature imaging, showing brighter fluorescence and deeper penetration (**Figure** 3-5, **Figure** 3-6).

Observation of living tissues is hard to achieve with conventional (confocal) fluorescence microscopy, because short excitation wavelengths undergo scattering and absortpion in tissues, increasing background noise. Besides, the excessive excitation energy outside the focal plane may bleach surrounding chromophores or cause photodamage.[82] 2PFM technologies make living tissue imaging possible by using longer wavelengths and extremely localized focal plane.
In this study, tumors were dissected 2 h after probe injection. Small sections were cut from the edge of the tumor, where angiogenesis occurred, for 2PFM imaging. Sections were scanned from top to bottom, where thetop was the cutting cross section, in order to get a flat surface for depth measurement. The results showed fluorescence collected at the depth of 350 μm by 2PFM. (**Figure 3-5**, B) Vasculature structures were still well defined even at as deep as 350 μm inside solid tumor tissue.

3.5 Conclusion

In conclusion, fluorene-substituted pyran derivatives PF **1** and PF **2** were designed as hydrophilic structures, showing good photophysical properties in DMSO. After conjugation with an $\alpha_v\beta_3$ integrin targeting cyclic RGDfK peptide, both structures exhibited significant vasculature targeting. Penetration of fluorescence emission was observed as deep as 350 μm, with good resolution of vasculature structures. As a result, RGD-conjugated PF structures may be promising probes for living tissue imaging in the future.

CHAPTER 4. APPLICATION OF INTEGRIN TARGETING FLUORENE DYE IN WOUND VASCULATURE IMAGING

Reproduced with permission from Ciceron O. Yanez, Alma R. Morales, Xiling Yue, Takeo Urakami, Masanobu Komatsu, Tero A. H. Jarvinen, and Kevin D. Belfield, Deep Vascular Imaging in Wounds by Two-Photon Fluorescence Microscopy. *PLOS ONE* **2013,** *8* (7), e67559.

Deep imaging within tissue (over 300 μm) at micrometer resolution has become possible with the advent of two-photon fluorescence microscopy (2PFM). The advantages of 2PFM have been used to interrogate endogenous and exogenous fluorophores in the skin. Herein, we employed the integrin (cell-adhesion proteins expressed by invading angiogenic blood vessels) targeting characteristics of a two-photon absorbing fluorescent probe to image new vasculature and fibroblasts up to ≈ 1600 μm within wound (neodermis)/granulation tissue in lesions made on the skin of mice. Reconstruction revealed three-dimensional (3D) architecture of the vascular plexus forming at the regenerating wound tissue and the presence of a fibroblast bed surrounding the capillaries. Biologically crucial events, such as angiogenesis for wound healing, may be illustrated and analyzed in 3D on the whole organ level, providing novel tools for biomedical applications.

4.1 Introduction

Microscopy of biological specimens deep within the tissue was limited to several hundred microns for several decades because visible light is severely scattered in biological

tissue, leaving to histology the analysis of many relevant physiological events that occur deep within tissues of living organisms. Imaging within tissue (over 300 μm) at micrometer resolution has been achieved by two-photon fluorescence microscopy (2PFM).[100, 101] This technique has been useful in exciting endogenous and exogenous fluorophores in the skin.[4, 102, 103] A good example of the penetration capabilities of 2PFM was recently published, where an impressive 1.6 mm penetration depth was reported by 2PFM, in the cortex of a mouse brain.[104]

The advantages of 2PFM have been exploited in imaging the skin and used in conjunction with one-photon reflection microscopy.[105] The skin, besides being the largest organ in the body, is a protective barrier that keeps other organs from being exposed to external harmful agents. As soon as an injury takes place on the skin, a clot is formed (fibrin clot) that acts as a temporary plug to seal it quickly. Within several hours following the insult, inflammatory cells invade the clot to fight against infection and to phagocytose necrotic cell debris. Several days later, the invasion of inflammatory cells is followed by capillaries and fibroblasts. Throughout the invasive neoangiogenesis that takes place during the wound healing process, endothelial cells up-regulate integrin $\alpha_v\beta_3$, a specific adhesion receptor for migrating cells on their cell surface, but this integrin disappears from the blood vessels/wound once the revascularization is completed.[84, 105, 106] Furthermore, during the early stages of wound healing, residing cells of the dermis that are in the immediate vicinity of the wound edges, which are otherwise relatively sedentary, become activated and invasive to form a matrix for what will become the repaired tissue (**Figure 4-1,** d).

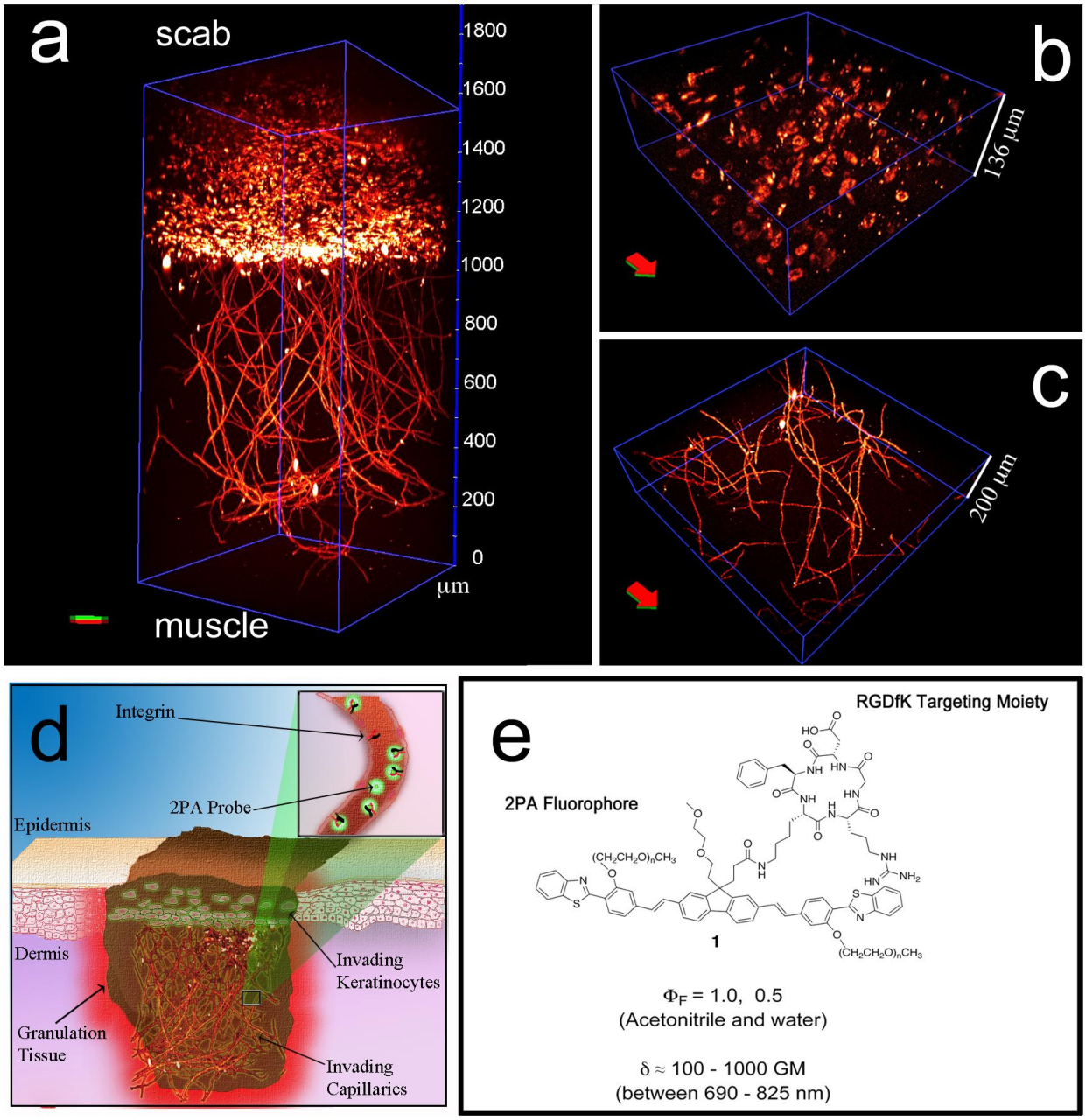

Figure 4-1. 2PFM of the ‘‘whole-mounted’’ wounds was performed and reconstructed for 3D visualization (a). RGD-containing probe **1** (e) was employed to target integrins. Integrin-expressing cells (b) and capillaries (c) in optical section are shown separately. d explains the depiction of a wound during the granulation tissue formation.

Many integrins, such as $\alpha_v\beta_1$, $\alpha_v\beta_3$ and $\alpha_5\beta_1$, are recognized by the Arg-Gly-Asp (RGD) motif found in many extracellular matrix proteins, i.e., expressed by their natural ligands.[106] Due to the restricted expression of $\alpha_v\beta_3$ integrins on the angiogenic vasculature, linear and cyclic RGD-peptides specific for $\alpha_v\beta_3$ integrins have been used for various purposes such as targeting drugs specifically to tumor vasculature.[84, 85]

In this chapter, a custom-made 2PA-absorbing fluorescent probe was used to image invading, angiogenic capillaries within the wound. The integrin (cell-adhesion proteins expressed by invading cells) targeting characteristics of this fluorescent probe revealed new vasculature and fibroblasts up to ≈ 1600 μm within wound (neodermis)/granulation tissue in lesions made on the skin of mice. Reconstruction exposed the three dimensional (3D) architecture of the vascular plexus and the presence of a fibroblast bed surrounding the capillaries.

4.2 Materials and Methods

4.2.1 Probe **1** Structure

Synthesis, purification, along with structural and photophysical characterization of probe **1** was already published.[107] (**Scheme 4-1**)

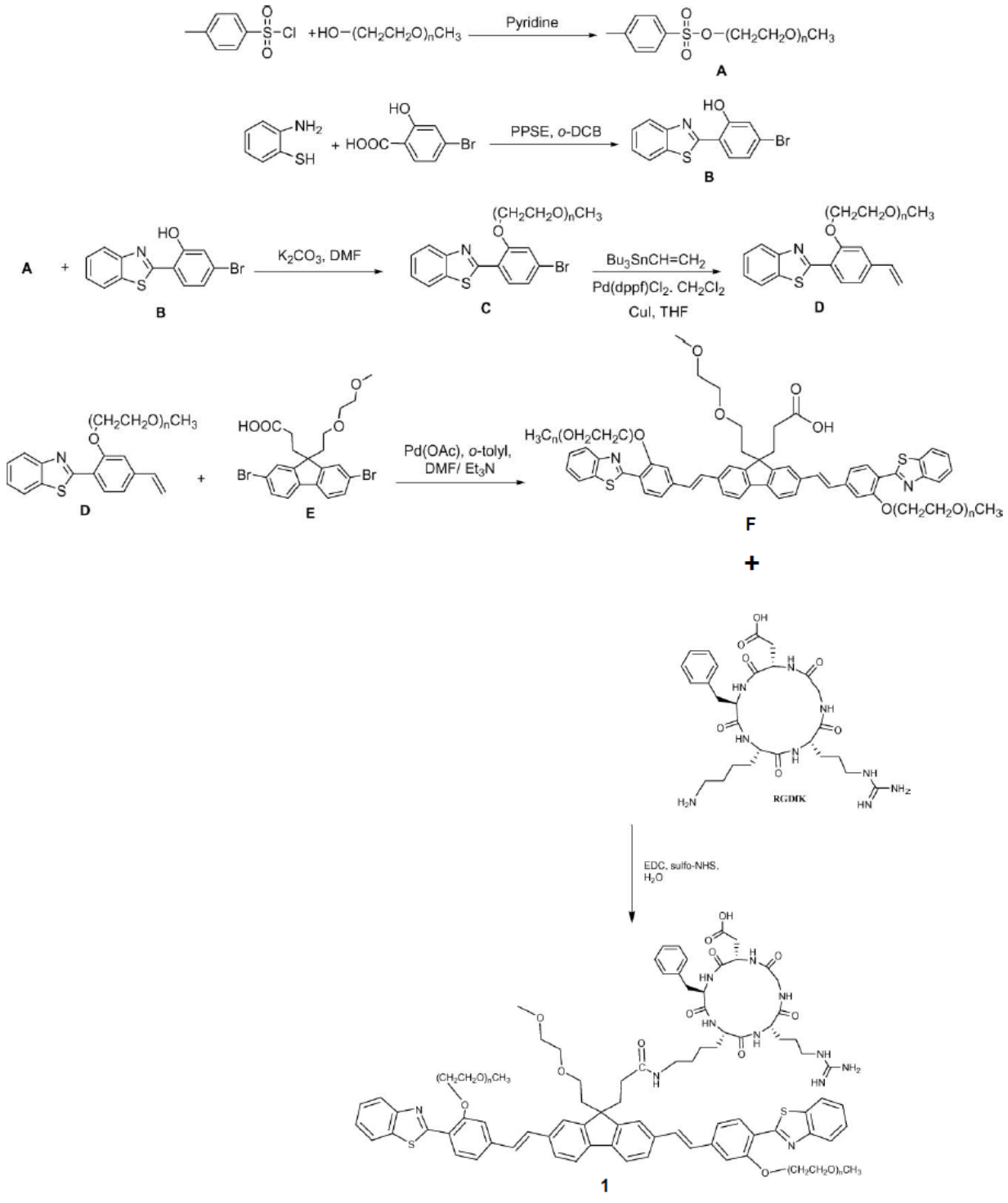

Scheme 4-1. Synthesis of RGD conjugated probe **1**. [107]

4.2.2 Ethics Statement

All animal experiments were reviewed and approved by the institutional anim825al care and use committees of Department of Orthopedic Surgery, Medical School, University of Tampere, Finland.

4.2.3 Wound Healing Model and Administration of Probe **1**

Eight-week-old male BALB/c mice (weighing 23–25 g) were anesthetized with 4% isoflurane and 1.5 L/min of oxygen, and the anesthesia was maintained at ≈1.5% isoflurane at 1 L/min of oxygen. Skin was shaved, cleaned, and disinfected with betadine and 70% alcohol. Treatment trials were conducted on mice that had circular, 6-mm diameter, full thickness (including panniculus carnosus muscle) excision wounds in the dorsal skin. The wounds were first marked by a biopsy punch and then cut with scissors. All skin wounds were left uncovered without a dressing.

After 7 days post-wounding, the mice were injected with 200 μL of a 600 μM solution of probe **1** in PBS, and this was allowed to circulate for 2 h, then perfused first with 1 x PBS + 1% BSA and then with 4 % paraformaldehyde (PFA) for fixation. Excision of a rectangular section of skin containing all wounds as well as underlying skeletal muscle was performed to ensure the uninterrupted wound architecture (**Figure 4-2**). The “whole-mounted” sections were immobilized on filter paper, immersed in 4 % PFA for additional O/N fixation, washed with physiological saline, and imaged from the internal and external faces of the wound.

Figure 4-2. Excised wound healing sample was whole-mounted and imaged by 2PFM.

4.2.4 Microscopy

2PFM with probe **1** was performed on a Leica SP5 II equipped with a Coherent Chameleon Vision S laser source (prechirped compensated, 70 fs, 80 MHz). Micrographs of the whole-mounted fixed tissues were taken under the following conditions: excitation at 825 nm, emission external non-descanned PMT detectors (NDD). A 665 nm shortpass filter was incorporated into the scanhead of the microscope, to avoid excitation laser bleedthrough, and a bandpass barrier filter 457/50 was placed before the NDD. A 20x, 1.0 N. A. water immersion objective was used for ex vivo imaging. Segmentation analysis and 3D rendering was performed with Amira.

Segmentation analysis involved establishing a threshold for the pixels to be counted in each optical section; in all cases the pixels with lowest 5% and the highest 5% counts per second were discarded for the final volume tally. The volume, conformed by fluorescent pixels, was determined and divided by the total scanned volume to determine the vascular density.

4.2.5 Immunohistochemistry

Formalin-fixed, paraffin-embedded tissue sections (5 μm thickness) were prepared from the skin wound model after whole mount two-photon excitation fluorescence imaging. Briefly, the skin was cut longitudinally at the middle of the wounds, mounted and paraffin embedded. Tissue sections were deparaffinized and antigen retrieved by Diva Decloacker (Biocare Medical, Concord,CA) at 120 ˚C for 4 min, blocked for unspecific binding by a species-matched 10 % serum, and then stained with primary antibodies. Following primary antibodies were used: anti-CD34 (clone MEC14. 1:100, BioLegend (San Diego, CA), anti-alpha smooth muscle actin (ab5694, 1:500) and Fibroblast activation protein, alpha (ab53066, 1:200, both from Abcam Cambridge, MA), anti-Mouse Mac-3 (clone M3/84, 1:100, BD Pharmingen, San Jose, CA). Alkaline phosphatase-conjugated with streptavidin (Vector Laboratories, Burlingame, CA) were used to detect primary antibodies in the combination with biotin-labeled species-specific secondary antibody (Invitrogen, Grand Island, NY) and visualized with alkaline phosphatase substrate kit I (Vector Laboratories).

4.3 Results

4.3.1 Fluorescence Spectra

One- and two-photon absorption, emission and anisotropy spectra are shown in **Figure 4-3**.[107]

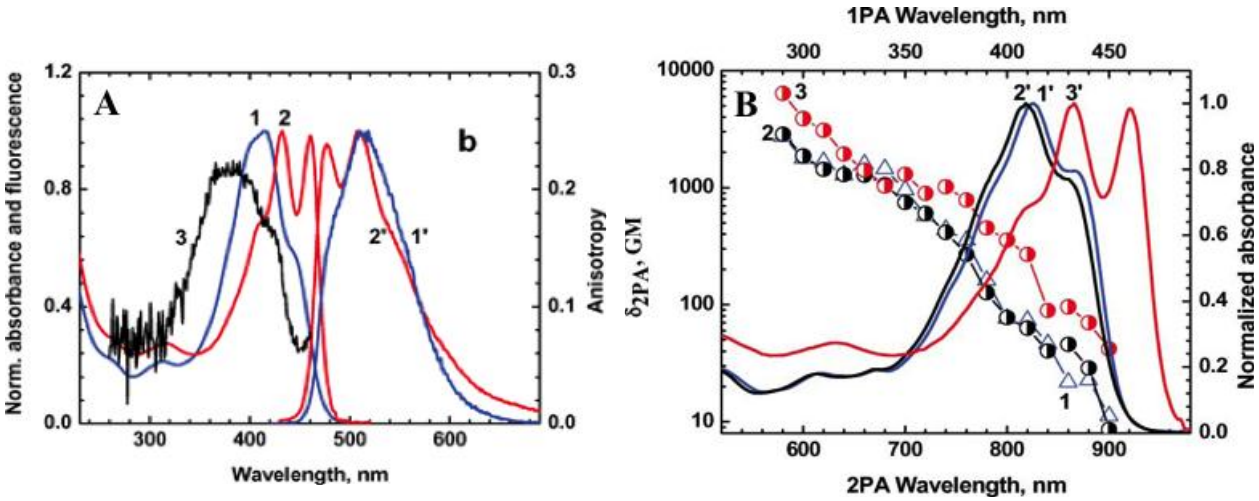

Figure 4-3. (A) One-photon absorption (1, 2), emission (1', 2') of probe **1** in water-chloroform mixture; (B) two-photon (1, 2, 3) and one photon (1', 2', 3') absorption in chloroform, acetonitrile and water.

4.3.2 Two-Photon Microscopy

Excitation from the external face of the wound resulted in poor penetration (not shown) due to absorption by the scabs formed at the surface of the lesion, and the presence of fur also interfered with imaging the neovasculature. From the internal side, it was necessary to overcome collagen/elastin autofluorescence; yet the images were much clearer overall (**Figure 3-1**, A-C). Imaging with shorter wavelengths (690 - 720 nm), where the δ2PA ≈ 1000 GM, was also explored but the contrast was significantly diminished compared with the 800 - 825 nm excitation range. The loss of contrast was primarily due to the excitation of collagen and/or elastin autofluorescence in muscle fibers. Even though cross sections at 825 nm were roughly an order of magnitude lower than at 690 nm, penetration and contrast were significantly enhanced at this wavelength.

3D reconstruction of invading capillaries shows roughly 1600 μm penetration. Vascular plexus extends from 0 to approximately 1100 μm (**Figure 4-1**, c) and integrin-expressing cells from 1100 to 1600 μm (**Figure 4-1**, b).

4.3.3 Segmentation Analysis

Segmentation analysis of the sample was performed throughout sections of the scanned volume to determine vascular densities (**Figure 4-4**). Vascular densities varied significantly throughout the specimen, progressively becoming smaller as one approached the leading end of the capillaries where it reached its smallest value of ≈ 3500 μm^3 of vessels per cubic millimeter of tissue.

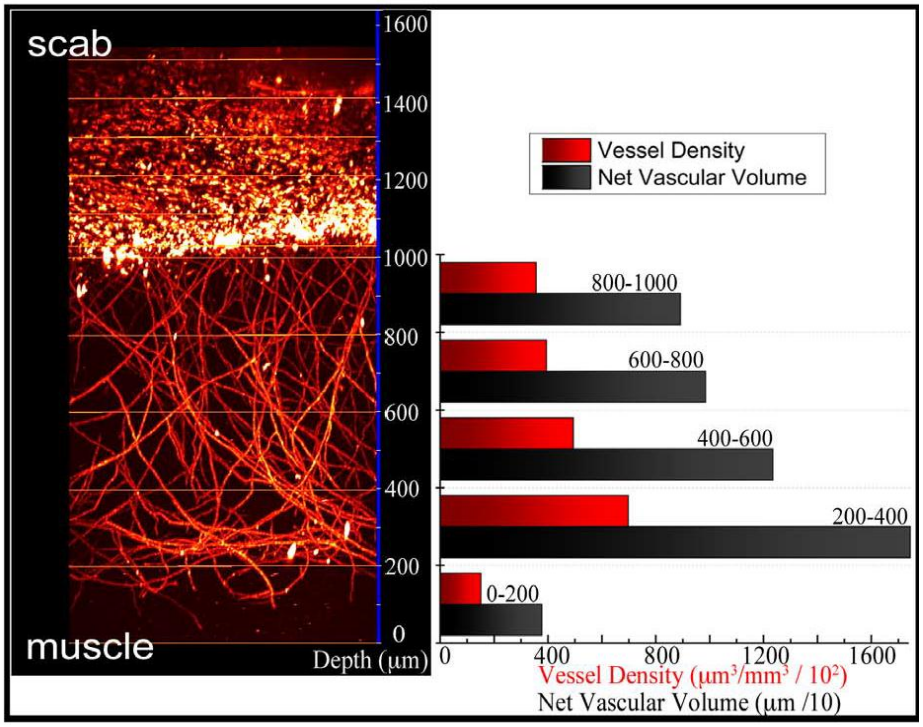

Figure 4-4. Segmentation analysis from 2PFM images. Fluorescent pixels were used to account for the vasculature.

4.3.4 Immunohistochemistry

After the whole-mount two-photon excitation fluorescence imaging of the excised wounds, immunofluorescence staining of horizontal tissue sections of the wounds were carried out to identify different populations of the wound bed; macrophages, integrin-expressing endothelial cells, granulocytes and fibroblasts in the granulation tissue (**Figure 4-5**). The fluorescence resulting from two-photon excitation of probe **1** is shown in green and the one-photon fluorescence of each cell type marker is shown in red.

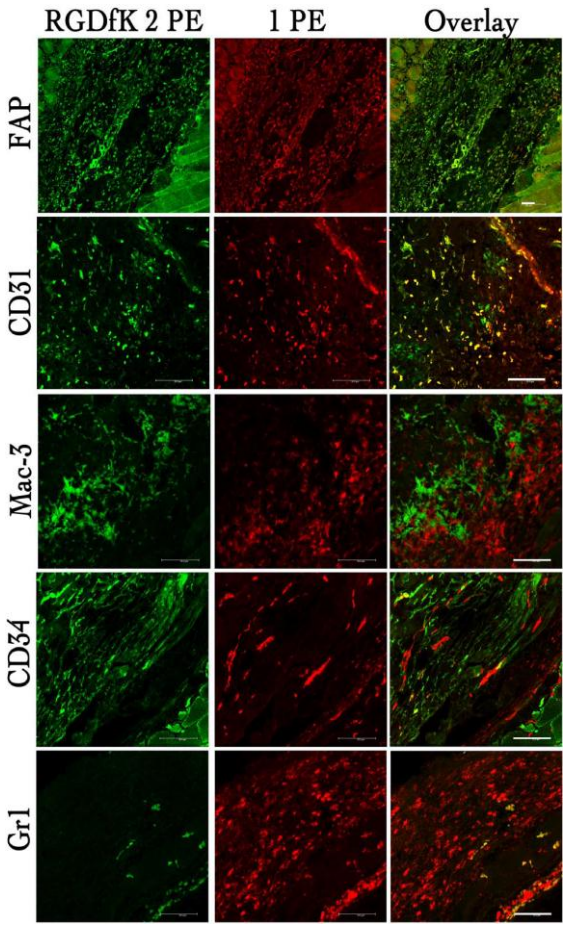

Figure 4-5. Immunohistochemistry staining of tissue sections of wound healing specimen.

Macrophages were stained with a Mac-3 antibody conjugate; the Mac-3 antigen is upregulated by monocytes during their differentiation to macrophages. Colocalization of the Mac-3 conjugate with probe **1** was largely absent in this analysis. As expected, the entire fibrin clot was invaded by macrophages, whereas integrin positive cells had different cell distributions throughout the wound. A CD31 antibody conjugate was used to stain endothelial cells, partial co-localization with the signal from our probe confirmed that endothelial cells were successfully targeted. Furthermore, CD34 antibody, used to stain endothelial cells and endothelial cell precursors, showed partial colocalization with probe **1**.

4.4 Discussion

Understanding the complex dynamics of the wound healing process has traditionally relied on optical microscopy techniques of cells and tissue. Optical microscopy has been instrumental in understanding the process of wound healing, primarily via the staining (H&E) of tissue sections and fluorescence confocal microscopy analysis.[108-110] The limitation of penetration depths in conventional (one-photon absorption, 1PA) fluorescence microscopy has made tissue sectioning mandatory in the analyses of the wound healing process. However, both the fibrin clot and the early granulation tissue have "jelly-like" consistencies and are easily ruptured during the processing of the tissue, leading to the disrupted tissue architecture while the dense "scab" tissue (dead tissue) formed on top of the wounded area (on the top of the immature early granulation) makes it impossible to visualize the actual healing process from the top of the skin. Furthermore, the scab tissue also compromises the quality of the histological sections; vast areas of the wound are lost during the histological processing of the skin wounds.

The wound architecture was maintained virtually intact by keeping the surrounding tissue (primarily muscle) to support the sample during collection. The samples were "whole-mounted" (mounted without further sectioning) and analyzed by 2PFM once it was excised from the mouse (**Figure 4-2**). The autofluorescence emanating from connective tissue of the muscle did not affect the analyses due to the high efficiency of the probe (high two-photon action cross section, $\delta.\Phi_F$), which provided a high enough signal-to-noise ratio to reveal individual integrin-expressing fibroblasts and endothelial cells beyond 1000 μm.

Just as for linear absorption, the efficiency of 2PA can vary significantly from molecule to molecule. In order to take complete advantage of the virtues of 2PFM, fluorophores should have a very particular set of values that include high 2PA cross section, high fluorescence quantum yield, and low photo-decomposition quantum yields.[111] We recently reported the development of an efficient 2PA RGD-containing fluorescent probe **1** that has proven to be useful in imaging integrin sites in cells and tumor vasculature.[107] The probe consisted of two units: 1) a two-photon absorbing component that was designed to exhibit a high 2PA cross section and high fluorescence quantum yield; and 2) a cyclic-RGD peptide that targeted the probe toward αvβ3 integrin expressed on the sprouting capillaries within the wound. The core of the 2PA chromophore was a fluorene molecule flanked by two benzothiazolyl styryl groups in positions 2- and 7-, constructing an A-π-π-π-A system, where A represents an electron-accepting moiety. An olygo-(ethylene glycol) (OEG) chain was incorporated to each styryl phenyl ring to improve the hydrophilicity of the probe. Cyclic RGDfK (c-RGDfK) peptide binds very specifically to αvβ3 integrin.[99] Detailed linear and nonlinear photophysical characterization was previously reported for this probe.[107] The fluorescence quantum yields were 1.0, 1.0, and 0.5

when measured in chloroform, acetonitrile, and water, respectively. Although probe **1** is not symmetrical, its behavior was akin to that of compounds with C2V symmetry, in the sense that the efficiency of its 2PA transition S0 $\rightarrow$S1 is greatly reduced by the dipole selection rules.[112] Nonetheless, the 2PA cross-section values were quite adequate for 2PFM, ranging from $\delta 2PA \approx$ 100-1000 GM (between $\lambda \approx$ 690-825 nm). These values were crucial in obtaining the maximum possible contrast in the micrographs, particularly in this system where the fluorescence signal of the chromophore had to overcome the autofluorescence noise from the connective tissue in muscle that surrounded the fibrin clot.

Two of the main indicators of the proliferative phase in the granulation tissue during the wound healing process are the invasion of fibroblasts and the capillaries in fibrin clot.[108, 113] Within 2 to 3 days, when inflammation is receding, fibroblasts start to appear in the fibrin clot and are the predominating cells in the wound site after a week (**Figure 4-**1 d). They rely on a fibrin/fibronectin scaffold to migrate into the wound. The main role of fibroblasts at this stage is to layout the collagen monomers. This early, loose granulation tissue, upon cross-linking of collagen, will form the firm collagen network at the later stages. This network is key for establishing the mechanical integrity for the disrupted tissue in later phases of the wound healing process. Angiogenesis is a concomitant event, or even precedes, the fibroblast invasion, providing both oxygen and nutrients the fibroblasts need in building the granulation tissue. Figure 3 (A, C, and D) illustrates new capillaries that have invaded the wound. Endothelial cells of new capillaries up-regulate $\alpha_v\beta_3$ integrin, which is transiently expressed only at the tips of sprouting capillaries.[108] Thus, the peptide binding to $\alpha_v\beta_3$ integrin is very specific for newly

formed angiogenic blood vessels and can be used to illustrate the progress and extend of the angiogenesis as the tip of the sprouting capillaries are illuminated.

The results of immunohistochemistry staining (**Figure 4-5**) suggest that not all capillaries were perfused and that probe **1** only labeled endothelial cells of perfused capillaries. This is, in turn, in agreement with the known fact that not all angiogenic blood vessels are perfused during angiogenesis.

Probe **1** colocalized positively with some granulocytes that were costained with Gr-1 antibody. Fibroblasts were stained with anti-fibroblast activation protein (FAP) antibody. Many fibroblasts within the fibrin clot colocalized with RGD probe-positive cells. Thus, the RGDfK moiety on probe **1** targeted endothelial cells and endothelial cell precursors. The probe then extravasated to the extracellular matrix to accumulate within the fibroblast-rich stroma. This observation is consistent with that fact that $\alpha_v\beta_3$ integrin is expressed exclusively by the endothelial cells in the wound. Our results also suggest that the sprouting end of the new capillaries are quite leaky and that the probe binds to stromal cells that express other integrin receptors for RGD.

Reconstruction of the specimen in 3D (**Figure 4-1**, a-c) showed the architecture of the intact capillary network and the relative position of surrounding stromal cells with respect to the invading capillaries. Our probe provides the possibility of carrying out analyses on the whole tissue-level in a 3D-format, i.e. the intact wound tissue architecture can be visualized by this method. Such imaging ability was previously unattainable with this level of detail in intact tissue. Furthermore, the probe effectively extravasated from the capillaries to the surrounding granulation tissue. The ability to extravasate and accumulate in the granulation tissue provides an

unprecedented potential to identify tissue sequesters that are not perfused properly and could hamper tissue regeneration.

4.5 Conclusion

In conclusion, probe **1** was useful in revealing RGD-positive, integrin-expressing cells and endothelial cells up to approximately 1600 μm deep within the specimen. *In silico* reconstruction showed high resolution 3D images of the intact structure of the vascular plexus in healing wounds. The RGD peptide-targeted 2PFM imaging overcame problems associated with histological preparation of fibrin clot for analyses of wounds. This technique offers the possibility of a novel method for cell tracking and monitoring of angiogenesis during the proliferative phase of wound healing, providing an attractive path forward towards in vivo wound healing studies, as we were able to analyze the skin as a whole organ. Intravital 2PFM studies with custom-made imaging windows are currently being performed in our laboratory to image the wound healing process in real-time. This technology may not only be of substantial improvement for the reliable quantification and illustration of key biological processes taking place during the tissue regeneration in the skin, but also forge revolutionary opportunities to assess healing process in situations such as skin crafting and diabetes, where the re-vascularization of the craft/ischemic skin is the rate limiting step for regeneration to take place.

CHAPTER 5. APPLICATION OF SULFONIUM SALTS WITH A FLUORINE CORE TO INDUCE SELECTIVE CELL DEATH

Singlet oxygen sensitized photodynamic therapy (PDT) relies on the concentration of oxygen in the tissue to be treated. Most cancer lesions, however, have poor vasculature and, as a result, are hypoxic, significantly hindering PDT efficacies. An oxygen-independent PDT method may circumvent this limitation. To address this, three sulfonium salts were applied to produce a pH drop within HCT 116 cells via the generation of photoacid within the cytosol. This process was driven by one- or two-photon absorption (1PA or 2PA) of the endocytosed photoacid generators (PAGs). One of the fluorine PAGs, which had a significantly lower dark cytotoxicity and was more efficient in generating photoacid, effectively induced necrotic cell death in the HCT 116 cells. The data suggests that PAGs may be an attractive alternative PDT modality to selectively induce cell death in oxygen-deprived tissue such as tumors.

5.1 Introduction

The success of photodynamic therapy (PDT) requires the careful balance of three conditions that must be present in the targeted cells at the time of therapy: 1) oxygen saturation

of the tissue, 2) sufficient photosensitizer concentration throughout the lesion, and 3) sufficient intensity of the sensitizing light. Even in a single gland like the prostate, all three of these agents are present in quite heterogeneous concentrations and doses.[114, 115] This has significantly complicated and compromised the reproducibility of singlet oxygen photosensitized PDT ($^1O_2$-PS PDT).

For over 100 years photodynamic oncotherapy has sought to produce singlet oxygen in an oxygen-depleted environment. Vasculature in healthy tissue is very well structured; the inner walls of healthy vessels are conformed by well differentiated endothelial cells. In contrast, tumor vessels have very poor morphology and are conformed by immature cells in a mesh-like architecture that confers a leaky property to the vessel. The leaky character of these vessels generates a hypoxic and acidic microenvironment that induces the production of positive or negative regulators of angiogenesis.[116]

This hypoxic environment within a tumor often leads to poor outcomes in $^1O_2$-PS PDT because frequently there is a limited amount of oxygen to excite. The minimal concentrations of oxygen are quickly depleted upon $^1O_2$-PS PDT, making it extremely easy to saturate the irradiation dose upon treatment. Furthermore, these extreme hypoxic events are often followed by ischemia, which not only further compromises the flow of oxygen to the tumor but also hinders the delivery of complementary chemotherapeutic agents that are delivered via the blood stream.[115]

Herein, an oxygen-independent means of inducing cell death via PDT is shown. Instead of inducing singlet oxygen by photosensitization, a pH imbalance was induced within the cytosol of the cells that were targeted by a PAG, affording oxygen-independent PDT.

5.2 Materials and Methods

5.2.1 PAGs Structures

Three sulfonium salt PAGs were previously synthesized and reported.[117] Structures were shown in **Figure 5-1**. Both PAG1 and 2 have fluorine core, while PAG 3 has squaraine core.

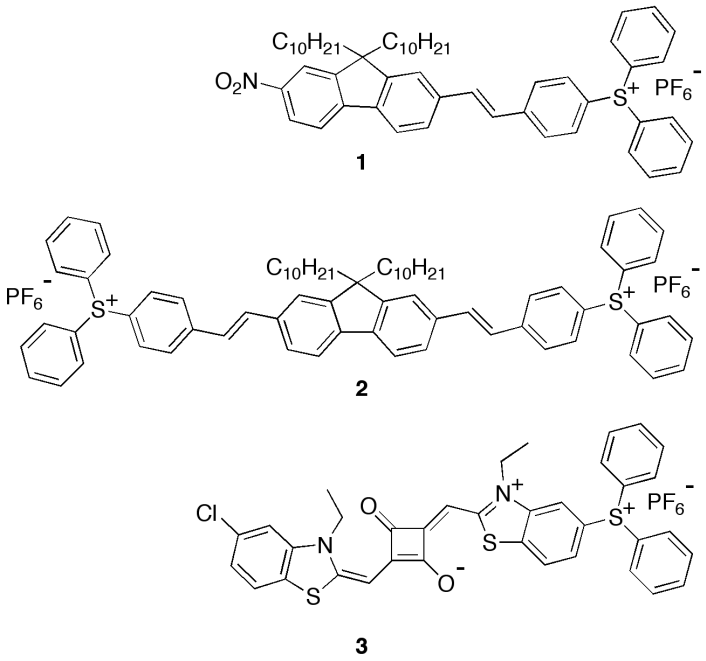

Figure 5-1. Sulfonium salt 2PA PAGs structures.

5.2.2 Encapsulation of PAGs

A solution containing 25 mg of Pluronic® F-127 in 10 mL of PBS buffer (pH= 7.4) was mixed with solutions containing PAGs in CH_2Cl_2 (10 mL), respectively. The organic solvent was allowed to evaporate at room temperature overnight. The mixtures were filtered through 2

μm pore size disposable filters and used as stock solutions. Concentrations of stock solutions (PL-PAG) were determined by molar absorption coefficient.

5.2.3 Cell Culture

HCT 116 cells (ATCC, USA) were cultured in RPMI-1640, supplemented with 10% FBS, 1% penicillin-streptomycin, at 37°C in a 95% humidified atmosphere containing 5% CO2.

5.2.4 Photocytotoxicity Assay

HCT 116 cells were seeded in 96-well black wall clear bottom plates (Corning, USA) at the concentration of 5×10^3 cells/well and incubated for 48 hours. For dark experiments, PL-PAGs were diluted into 0.5 μM, 1 μM, 5 μM, 10 μM and 15 μM from stock solutions. Cells were then incubated with diluted PL-PAGs for additional 24 hours. Viability was then determined with CellTiter 96® AQueous One Solution Reagent (Promega, USA). For photocytotoxicity experiments, PL-PAGs were diluted to 10 μM solutions and added into cells. For PL-PAG **1** and **2**, plates were then placed on an inverted microscope (Olympus IX70) coupled with a 100W mercury lamp. The distance between the bottoms of plates and objective was 1cm to make sure the whole well can be irradiated by the UV light. A customized filter cube (Ex 377/50, DM 409, Em 525/40) was used to match the excitation wavelength of PAGs. The final power reached the plates was 7.4 mW/cm^2. For PL-PAG **3**, plates were placed on an inverted microscope (Olympus Fluoview FV300) coupled with Coherent Mira 900F Ti:Sapphire laser. Cells were irradiated at 700 nm at the CW mode. The final power reached the plates was 5.3 mW/cm^2. Different irradiation times were used to reach the power of 0.03 J/ cm^2, 0.08 J/ cm^2, 0.24 J/ cm^2, 0.72 J/

cm^2, and 2.16 J/ cm^2. After irradiation, cells were incubated for another 24 hours before measuring the viability.

5.2.5 Lysosome Colocalization

Cells were cultured on 12 mm poly-D-lysine functionalized coverslips for 48 hours. PL-PAG **1** was then added into cells at a concentration of 10 μM together with LysoTracker Green at 1 μM for 1 h. Coverslips were then washed with PBS three times and mounted onto slides with ProLong® Gold antifade reagent. Slides were imaged with Olympus IX-81 confocal microscope. A customized filter cube (377/50, 409, 460/50) was used for PAG **1** and the FITC filter cube (477/50, 507, 536/40) was used for LysoTracker Green.

5.2.6 Live Cell Imaging of PL-PAG **1**

Cells were cultured on 40 mm poly-D-lysine functionalized coverslips for 48 hours. PL-PAG **1** was then added into cells at a concentration of 10 μM. After 24 hours, coverslips were washed with PBS three times and mounted onto a bioptics live cell imaging chamber. After irradiated with UV lamp for 100s (0.72 J/ cm^2), cells were imaged with Olympus IX-81 DSU microscope at 1 min intervals for 3 hours in DIC channel.

For in vivo pH indicator, cells were co-incubated with 10 μM PL-PAG **1** (24 hours incubation) and 1 μM LysoSensor Green (Invitrogen, USA) for additional 2 hours. After irradiation, cells were imaged at 1 min intervals for 30 min with FITC channel. Fluorescence intensities at different time points were calculated with SlideBook.

5.2.7 Two-Photon Irradiation and Determination of the Type of Cell Death

Cells were cultured on 12 mm poly-D-lysine functionalized coverslips for 48 hours.

PL-PAG **1** was then added into cells at a concentration of 10 μM. After 24 hours, cells were irradiated with a Coherence two-photon laser at 710 nm for 13 min (70 fs pulses, 80 MHz repetition rate, 2.0 mW/cm^2). Cells were incubated for additional 4 hours before stained with Propidium Iodide (PI, BD Biosciences, USA) and fixed with 4% Formaldehyde. The coverslips were washed with PBS three times and mounted with ProLong® Gold antifade reagent (Invitrogen, USA). Images were taken with Olympus IX-81 DSU microscope.

5.2.8 Measurement of Lysosomal pH Drop

Cells were cultured on 40 mm poly-D-lysine functionalized coverslips for 48 hours. PL-PAG **1** was then added into cells at a concentration of 10 μM together with LysoSensor Green at 1 μM for 2 h. Coverslips were then washed with PBS three times and mounted onto a bioptics live cell imaging chamber. After irradiated with UV lamp for 100s (0.72 J/ cm^2), cells were imaged with Olympus IX-81confocal microscope at 1 min intervals for 30 min with FITC channel. Fluorescence intensities at different time points were then calculated with SlideBook.

To estimate pH drop quantitatively, a solution of PL-PAG **1** (10 μM) and Rh B (100 μM) was placed in a cuvette and the absorption of RhB was recorded. The mixture solution was then exposed at UV lamp and absorption was recorded every 5 s. The absorbance at 555 nm was plotted to make a dose dependent calibration curve. H^+ generation was estimated from the curve and pH drop was calculated.

5.3 Results

5.3.1 Photophysical Properties of PAGs

The photophysical properties of PAGs were previously measured and published.[117] PAG **1** exhibited an increased photoacid quantum yield (**Table 5-1**). The 2PA cross-sections, however, were found to be up to 5 times higher for PAG **2** than for PAG **1** (**Table 5-1**). This disparity in 2PA cross-section values vs. photoacid quantum yield values makes it difficult to rank these PAGs by their overall efficiencies. Using only one of these two photophysical properties would be incomplete and could lead to erroneous interpretations.

Table 5-1. Photophysical properties of PAGs

PAG	Φ_F	Φ_{H+}	δ_{710} (GM)	$\Phi_{H+}.\delta$ (GM)
1	0.10±0.01	0.40±0.04	240±24	96±10
2	0.80±0.06	0.03±0.003	1275±130	38±4
3	0.27±0.02	0.01±0.005	-	-

δ: two-photon absorption cross-sections at 710 nm; $\Phi_{H+}.\delta$: two-photon action cross-section of photoacid generation at 710 nm.

A more useful value to compare the PAGs is the 2PA action cross-section of photoacid generation, given by the product of photoacid generation quantum yield and the 2PA cross-section at a specific wavelength. On the basis of the 2PA action cross-section, the overall efficiency of PAG **1** was higher than that of PAG **2**.

In a constant effort to improve the properties of these molecules, other PAGs are currently being synthesized in the lab that absorb at longer wavelengths and possess higher 2PA cross-sections. An example of this type of molecule is PAG **3** (**Figure 5-2**). The squarane core

has the advantage of having a linear absorption λ_{max} in the NIR and has been associated with high 2PA absorption. (**Figure 5-2**)

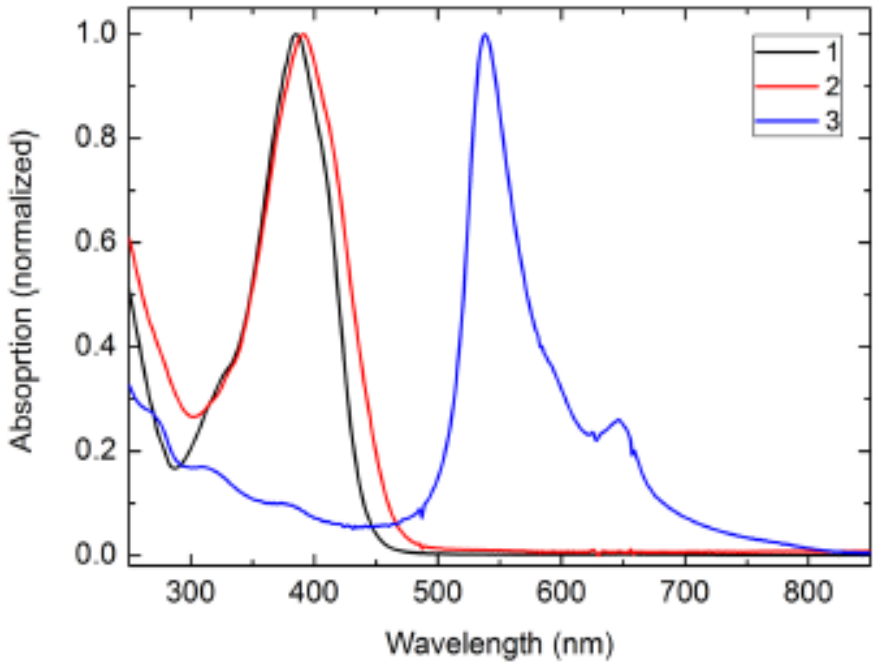

Figure 5-2. One-photon absorption spectra of PAGs in PBS following Pluornic-127 encapsulation.

5.3.2 Dark Toxicity and Post-Irradiation Toxicity of PL-PAGs in HCT 116 Cells

PL-PAG **1** and **3** showed minor toxicity to HCT 116 cells until 10 μM (**Figure 5-3)**. At this concentration, both groups still presented 80% viability. PL-PAG **2**, however, gave a high toxicity in dark, which eliminated its further application in cells.

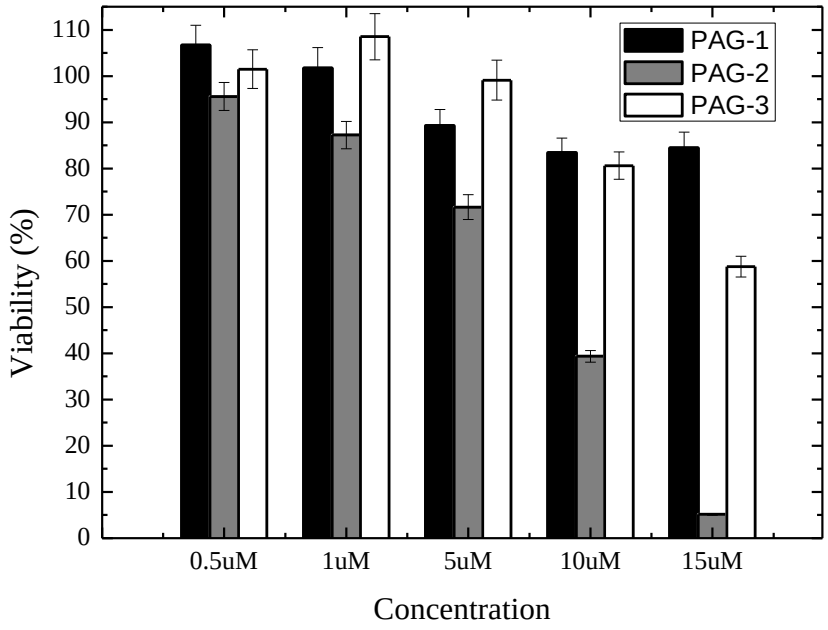

Figure 5-3. Dark toxicity of PL-PAGs in HCT 116 cells.

In the exposure experiment, both exposure source for PL-PAG **1** and **3** exhibited no toxicity to cells by themself. (**Figure 5-4**) PL-PAG **3** didn't induce noticeble cell death in 900 s. This propbably due to its low photoacid quantum yield. PL-PAG **1**, on the other hand, with lowest dark toxicty, exhibited highest post-exposure toxicty. The IC50 dose of PL-PAG **1** was about 100 s. And the viability further dropped to less than 20% at 900 s exposures. The viability change also fitted well to the dose-dependence curve. These results indicated that PL-PAG **1** could be a promising candidate for irradiation induced cell death.

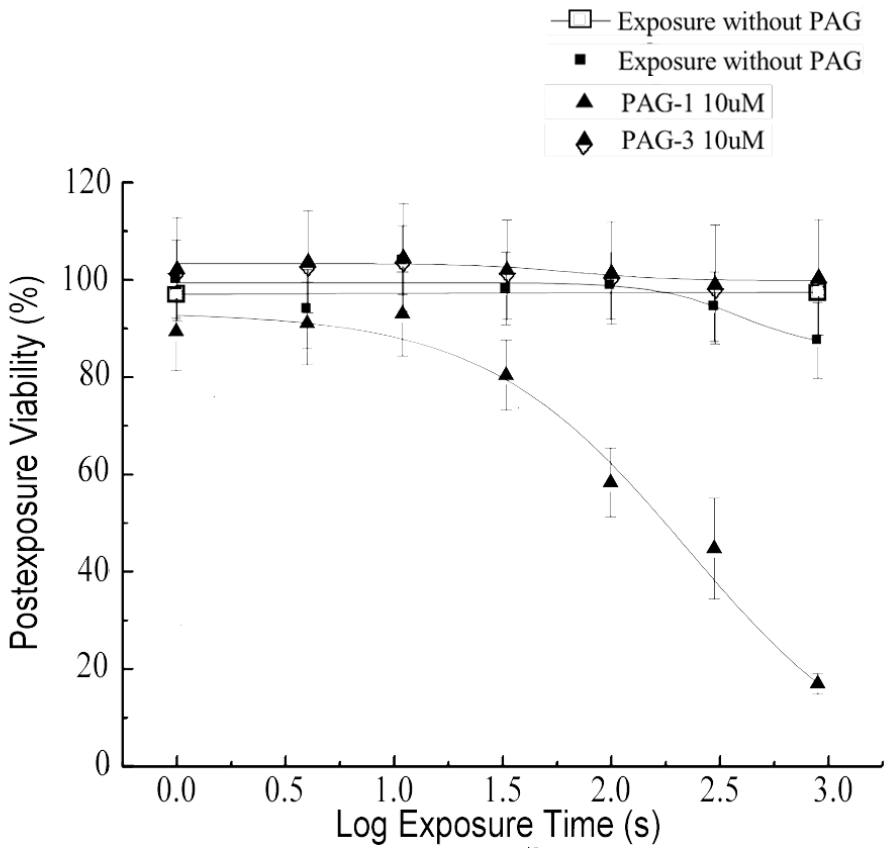

Figure 5-4. Post-exposure toxicity of HCT 116 cells incubated with PL-PAG **1** and **3**.

5.3.3 Colocalization of PL-PAG **1** and LysoTracker Red

To investigate where PL-PAG **1** travels to inside HCT 116 cells, cells were coincubated with PL-PAG **1** and LysoTracker Red, which is a commercial dye that known to stay in Lysosome after uptake by cells. Fluorescence of PAG **1** was collected inside cells (**Figure 5-5, b**), showing a good uptake efficiency of PL-PAG **1**. Overlay image (**Figure 5-5, d**) exhibited good colocalization between PL-PAG **1** and LysoTracker Green, which indicated PL-PAG **1** mainly built up in lysosomes.

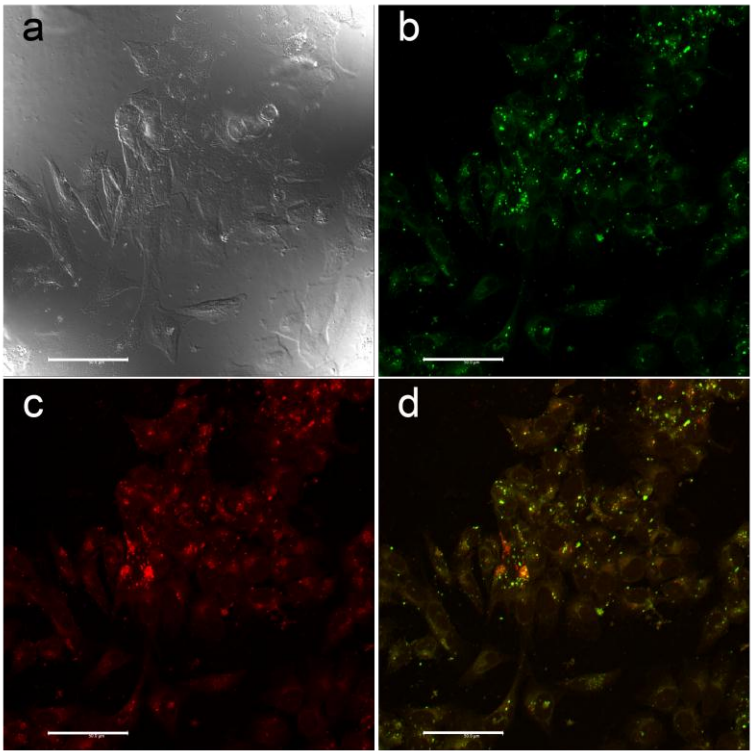

Figure 5-5. DIC (a) and confocal fluorescence images of HCT 116 cells coincubated with PL-PAG **1** (b) and LysoTracker green (c). Overlay image (d) shows PL-PAG **1** mainly built up in lysosomes. Scale bar shows 50 μm.

Pluronic® F-127 has been widely used in drug delivery applications to enhance the solubility of hydrophobic substances such as anticancer drugs.[118, 119] Pluronic® micelles are known to be endocytosed by MDCK cells by means of clathrin-mediated endocytosis when present above the critical micelle concentration.[120-122] The hydrophobic character PAGs **4-3** facilitated their encapsulation in Pluronic® F-127.[14, 123, 124]

5.3.4 Live Cell Imaging After Irradiation with PL-PAG **1**

Time-lapse images were taken to show the process of cell death by light irradiation with -1. (**Figure 5-6**) Widefield fluorescence image showed uptake of PL-PAG **1** in cells (green).

Colocalization with LysoTracker Red (red) showed PL-PAG **1** mainly built up in lysosomes. DIC images show the changes of cell morphology during death process. Green arrows indicate loss of cell adhesion, yellow arrows "blebbing"-like activity (shown in enlargement, lower frame), and blue arrows cell swelling. All cells in the observing area died after 4 h (shown in bottom right).

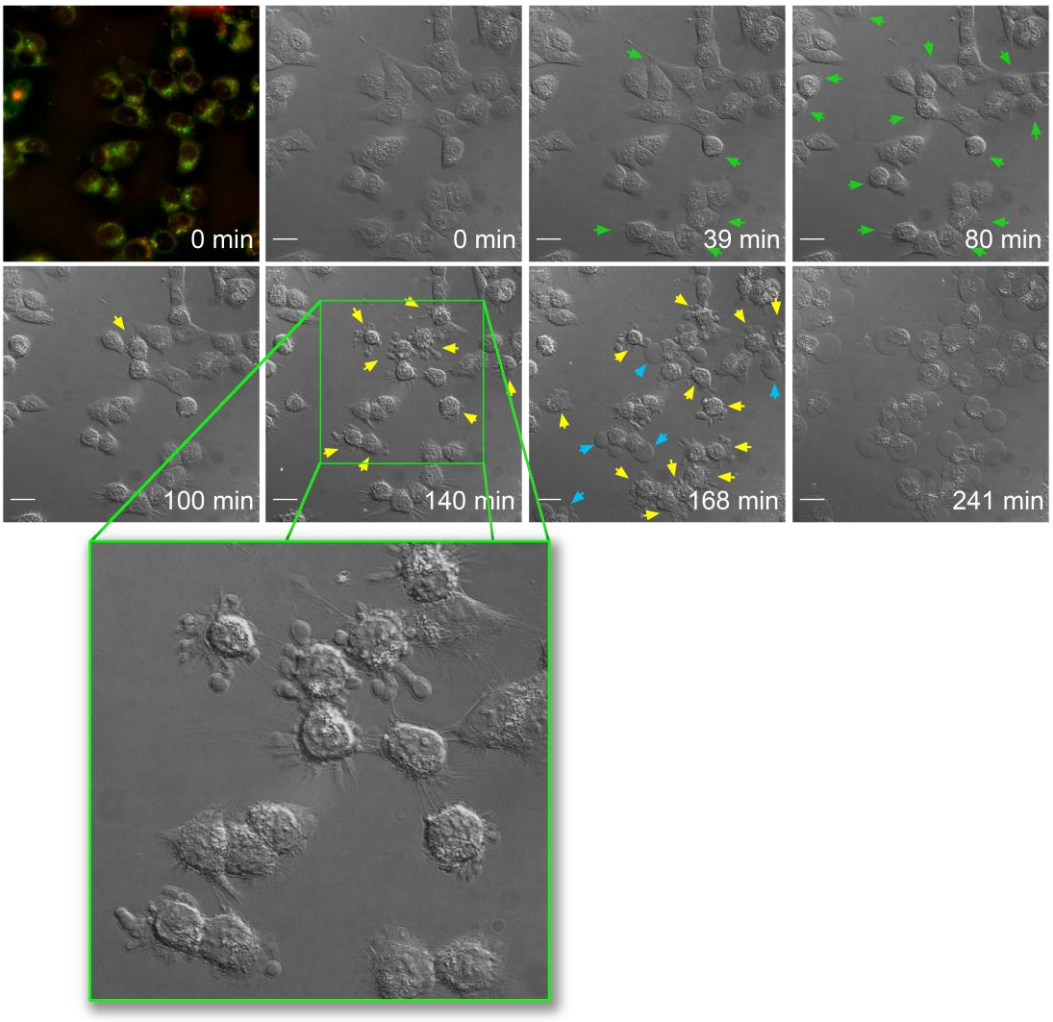

Figure 5-6. DIC and confocal fluorescence images of HCT 116 cells after irradiation with PL-PAG **1**. Scale bar shows 50 μm.

5.3.5 Type of Cell Death

Cell death could also be induced by two-photon photoacid generation. Cells were exposed to two-photon irradiation after incubated with PL-PAG **1** for 24 h. After irradiation, propidium iodide (PI) was employed to assess the proportion of cells that underwent necrotic cell death.

A control sample to determine the effect of the irradiation conditions on the cell was performed by irradiating cells that had not been incubated with the PAG. The micrographs showed excellent cell morphology (DIC) and high viability (low fluorescence intensity of the PI channel) of the cells for up to 24 h following irradiation. A second control, in which cells were incubated with PL-PAG **1** but were not irradiated, showed adequate cell uptake (fluorescence in PAG-1 channel) and no detectable cell death via the necrotic pathway. Irradiated cells showed significant cell swelling and loss of membrane potential as indicated by the uptake of the PI. The abnormal cell morphology and bright PI staining indicates cells underwent necrosis death. (**Figure 5-7**)

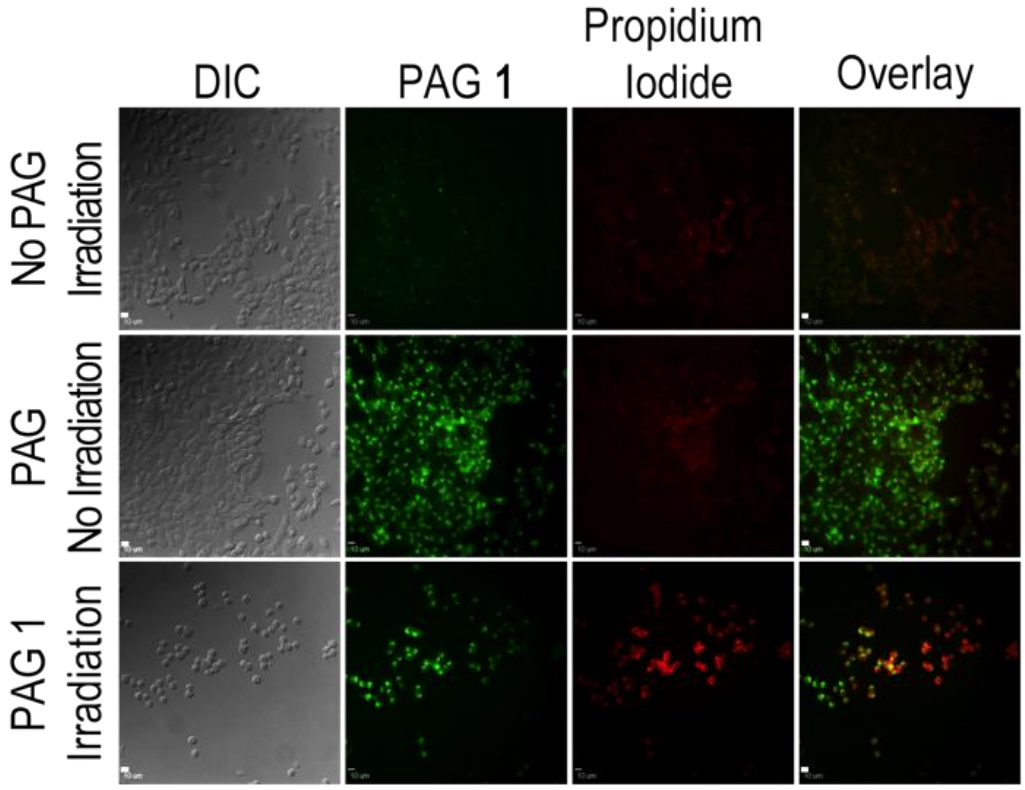

Figure 5-7. PI staining of HCT 116 cells after incubated with PL-PAG **1** and irradiated at 710 nm. Scale bar shows 50 μm.

5.3.6 Lysosomal pH Drop

LysoSensor Green has been reported to monitor acidic pH within cells.[125] This dye is known to increase its fluorescence quantum yields when in acidic compartments. Cell images show an increase in brightness for cells irradiated with PL-PAG **1**, while almost no change for the control cells. (**Figure 5-8**, left) Calculated fluorescence intensities at different time points also show the same trend. The drop in fluorescence intensities as a function of irradiation dose in control cells can be attributed to the photobleaching of the LysoSensor Green. On contrast, fluorescence intensity for PL-PAG **1** with irradiation group kept increasing at the beginning until

it reached the highest intensity at 17 min. (**Figure 5-8**, right) The increase of fluorescent intensity indicates a pH drop in lysosomes in HCT 116 cells after irradiated with PL-PAG **1**.

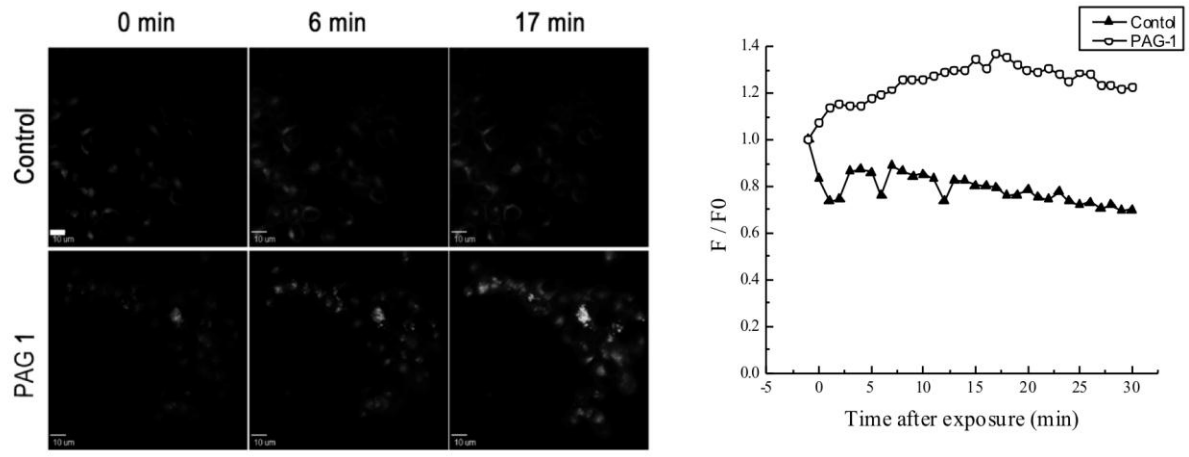

Figure 5-8. Increase of acidic content in cell lysosomes after cells irradiated with PL-PAG **1**. LysoSensor Green was employed as a pH indicator.

To quantitatively estimate the pH drop inside cell lysosomes, Rhodamine B was applied and its absorption was recorded. By means of this method the number of acid molecules generated was assumed to be the same as the number of Rhodamine B Base molecules converted to Rhodamine B+, causing a increase in absorption around 555 nm. H^+ generation was estimated to be 2.11×10^{-6} M via extrapolation of the calibration curve. (**Figure 5-9**) Considering the original pH of lysosome, the lysosomal pH would at least be reduced in 0.2.

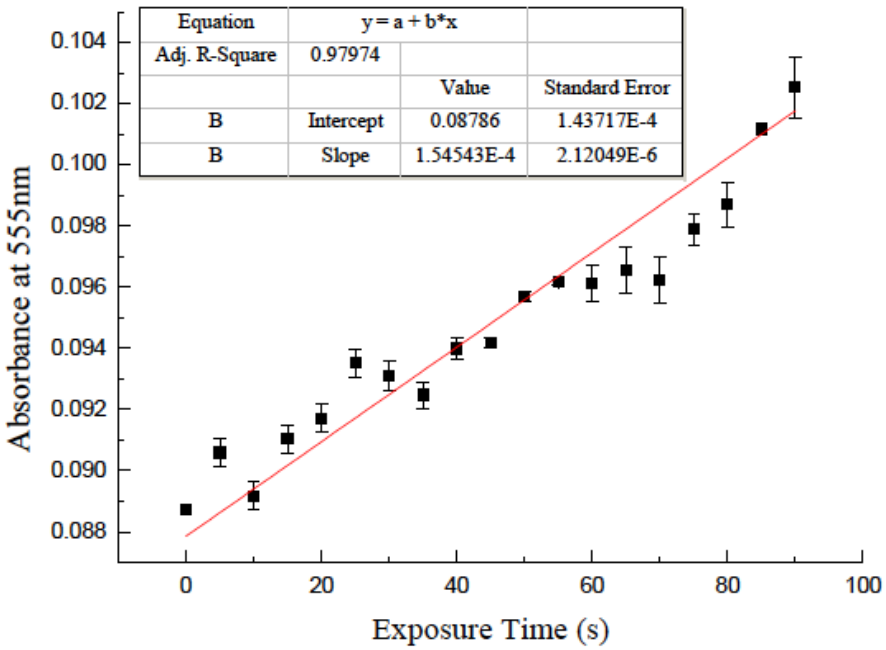

Figure 5-9. Absorbance changes of Rhodamine B at 555 nm. Calibration curve was calculated to estimate H^+ generation.

5.4 Discussion

Most commercially available PAGs have an absorption λ_{max} in the UV or deep-UV because their applications in lithography requires them to absorb at the shortest possible wavelengths. Recently, a series of more conjugated, longer-wavelength-absorbing PAGs were synthesized in our lab that were designed to be efficient two-photon absorbing molecules.[117] The generation of photoacid was induced by one- and two-photon absorption of PAGs **1-3** (**Figure 5-1**). To our knowledge, this is the first example the use of PAGs to cause cell death by generating a pH imbalance in the cell.

The emergence of nonlinear (2PA) techniques has taken advantage of the quadratic dependence that 2PA has on the intensity of the incident light.[29-31] This advantage can equally be

exploited in PDT applications and require that the molecules employed for therapy be efficient two-photon absorbers, i.e., the molecules need to have high two-photon-absorbing cross-sections. The possibility of using such agents in cancer lesions that are buried under sensitive, healthy tissue (i.e. gliomas) makes these 2PA PAGs especially important. Undoubtedly, the simplicity associated with generating photoacid by 1PA is also an advantage. One-photon photoacid generation is a more efficient process, where the excitation source needed is cheaper and easier to use. In exchange for tissue penetration, a larger amount of targeted surface mass within tissue can be covered at a faster rate.

Two-photon photoacid generation is a lower probability process, because it is energy dependent, and relies on more elaborate pulsed lasers as energy sources. However, it has a tremendous tissue penetration advantage and the process is confined to a smaller volume. Ideally, both methods can be used simultaneously to maximize the possibility of success of the OI-PDT process.

Originally the synthesis of triarylsulfonium salts was reported by Crivello and Lam, where the thermolysis of a diphenyliodonium in the presence of a diphenylsulfide formed the desired sulfonium salt.[126-128] Recently, a more efficient, microwave assisted-based, synthetic strategy of triarylsulfonium salt PAGs was reported.[117] PAGs **1**-**3** were designed to exhibit high 2PA cross-sections. Fluorene was chosen as the core structure of PAGs **1** and **2** because of its high thermal and photochemical stability.[129] Quite advantageously, fluorene lends itself to ready substitution in its 2-, 7-, and 9-positions. In PAGs **1** and **2**, stilbenyl motifs were introduced (2- and 7-positions) to extend the π-conjugation. Ultimately, two acceptor groups (triarylsulfonium and nitro) were introduced for net structures of A-π-π-A (PAG **1**) and A- π-π-π-A (PAG **2**).

To enhance the photoacid quantum yield per molecule, the first approach was to incorporate two sulfonium salt motifs onto the fluorenyl scaffold, such as in PAG **2** (**Figure 5-1**). However, this molecule exhibited very low photoacid quantum yields (0.03). The high fluorescence quantum yield of this PAG (0.80) indicated the molecule was undergoing radiative decay (fluorescence) before it had a chance to form photoacid.

The direct photolysis of triarylsulfonium salts has been reported to occur primarily from the first excited singlet state. However, sensitization studies have shown that triplet triarylsulfonium salts are also labile.[130] Consequently, to increase the probability of spin orbit coupling to induce intersystem crossing, a nitro group was incorporated into the fluorene backbone. As a result, the fluorescence quantum yield of the sulfonium salt (PAG **1**) was significantly decreased (Table 1), thereby reducing the radiative decay pathway.

A comparable figure of merit for one of the most widely used PDT agents photofrin (singlet oxygen quantum yield x 2PA cross section) illustrates the efficiency of the PAGs. In the literature photofrin oxygen quantum yields values are approximately 0.2, and its 2PA cross sections range from 10 – 15 GM.[131, 132] Based on these values, the action cross sections for photofrin would range from 2-3 GM. This value is significantly lower than that of PAG **1**.

The PL-PAGs were tracked through the vesicle maturation process of endocytosis. After the micelles undergo endocytosis, they can either reach full endosomal maturation, reaching the lysosomes, follow exocytosis before attaining the endo-lysosomal stage, or buildup in other regions like the mitochondria. We mainly observed the accumulation of the PL-PAGs in the endosomes-lysosomes (even after 24 h of incubation, **Figure 5-5**) in HCT 116 cells.

An ideal PAG for phototherapy would exhibit low cytotoxicity when unexposed and induce a high percentage of cell death upon irradiation. To assess the intrinsic toxicity of the PAGs, cell viability assays were initially carried out in the dark (dark viability) to avoid the production of photoacid. The results indicated PL-PAG **1** had the lowest dark cytotoxicity throughout this concentration range, followed by PL-PAG **3** and PL-PAG **2**, respectively (**Figure 5-3**).

Based on these results, exposure experiments were performed at 1, 5, and 10 μM for all PL-PAGs. The most appreciable changes in viability (from dark viability to post-exposure viability) were observed at 10 μM (**Figure 5-4**). PAG **1** showed the best results, promoting a drop from 90% viability to 20% viability after 3 seconds of exposure. Even at these relatively high concentrations, PAG **2** and **3** failed to induce a significant drop in cell viability. This is consistent with their photoacid quantum yields (**Table 5-1**), which are much less efficient in producing photoacid than PAG **1**, i.e., the induction of cell death was proportional to the amount of acid generated.

A correlation of irradiation and increase in lysosomal pH was demonstrated by the aid of LysoSensor Green. This indicates a drop in intralysosomal pH (of the already acidic compartments) followed irradiation in HCT 116 cells previously incubated with PL-PAG **1** (10 μM). The measurement of lysosomal pH, however, is rather complex and controversial, although there are reports of measuring lysosomal pH via ratiometric analysis (i.e. LysoSensor Green, FITC conjugates, Oregon Green 488 conjugates). Haggie and Verkman[133] reported difficulties in using commercial LysoSensor probes to quantitatively measure lysosomal pH, concluding previous reports using these dyes for pH measurement were either invalid or semi-quantitative at

best. Our situation is further complicated due to the presence of another absorbing molecule (e.g., PAG-**1**) with overlapping absorption and/or emission spectra with the pH probe. Thus, to provide an estimate of pH change, we used an approach previously found to quantify the concentration of photoacid molecules generated/photons absorbed by PAG-**1** has consisted using Rhodamine B base as an indicator.[117] It was estimated that a 10 μM concentration of PAG **1** would, at least, generate 2.11 x 10^{-6} M at the irradiation doses used 80% cell death (3min). This would lead to a drop of intralysosomal pH to about pH = 4.5 (**Figure 5-9**).

Cell death induced by two-photon photoacid generation was demonstrated in an experiment where HCT 116 cells were incubated with PL-PAG **1** for 24 h, followed by two-photon irradiation. All the cells in the exposed area appeared to die by necrosis (**Figure 5-7**), which is expected when such a grave physiological imbalance takes place. Time-lapsed micrographs show this progressive change in cell morphology following the generation of photoacid (**Figure 5-6**). Loss of cell adhesion (green arrows) is followed by a "blebbing"-like activity (yellow arrows). The integrity of the nuclei in these cells is a sign that chromatin condensation is not occurring and hence the process is not apoptotic. What followed was significant cell swelling that is characteristic of necrosis (blue arrows). Despite the low fluorescence quantum yield, PAG **1** was fluorescent enough to allow visualization of its uptake and co-localization with LysoTracker Red (**Figures 5-5** and **Figure 5-6**). The high degree of co-localization suggests that it was mainly localized in the lysosomes.

5.5 Conclusion

The use of photoacid generators to induce cell death by creating a grave pH imbalance in cells has not been reported prior to this work. We demonstrated that sulfonium-based PAGs

could be used to selectively induce cell death upon photoexcitation. This opens the possibility of photochemically inducing cell death in an oxygen-independent manner. More specifically, PL PAGs have induced necrotic cell death via generation of photoacid in the lysosomes in HCT 116 cells. Photoacid was generated by both 1PA and 2PA, which means cell death, can be induced by either method. In order to achieve deep tissue penetration, two-photon excitation is particularly attractive. Thus, the ability to induce two-photon photoacid generation of PAGs is significant and a particular priority. PL-PAG **1** is a versatile compound that can be used to exploit the advantages of one- or two-photon photoacid-based PDT. These results lay the foundations for the use of PAGs in OI-PDT.

CHAPTER 6. FUTURE WORK

Future applications of 2PA materials can be focused on live animal experiments. Due to the deep penetration of 2PA excitation, it is possible to conduct therapy or imaging tumor models with ultrafast laser system without sacrificing the animals. Besides, by applying functionalized nanoparticles, the therapeutic agents and imaging probes can be specifically delivered to the targeted area, which will increase the efficiency of therapy and resolution of imaging.[2, 134, 135] Furthermore, these two materials can be combined together, so that the therapeutic agents can be tracked by the imaging probes.[136, 137] As a result, silica nanoparticles that encapsulate 2PA fluorescent probes and PDT agents and are functionalized with, e.g., an RGD peptide are proposed for live animal experiment for the future work.

6.1 2PA Fluorescent Probes and PDT Agents Encapsulated in Silica Nanoparticles

Werner Stober and his coworkers discovered the physical chemistry process of making monodisperse silica nanoparticles (SiNPs) in 1968, by adding silane structures in water containing alcohol and ammonia.[138] This method was widely investigated and modified for different sizes, colors, and architectures. To function as a drug delivery system, SiNPs should be selective, nontoxic, and exhibit good clearance rates. One of the SiNPs platforms, Cornell dots (C dots), meet all these criteria and has been approved by the FDA for human clinical trials, suggesting SiNPs are promising deliver system for live animals.

All the 2PA fluorescence structures in this dissertation can be encapsulated into silica nanoparticles for tumor imaging. To best eliminate quenching effects of probes, different SiNPs architectures should be explored and the one with best performance can be selected. (**Figure 6-**

1). It was reported that for tetramethylrhodamine isothiocyanate (TRITC), expanded core-shell particles showed highest fluorescence intensity and longest lifetime.[139]

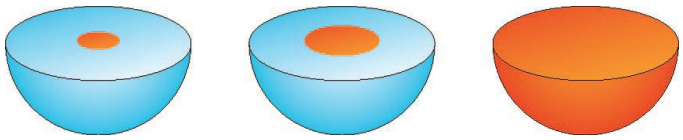

Figure 6-1. Three different silica nanoparticle architectures, designated from right as the compact core-shell particle, the expanded core-shell particle, and the homogeneous particle. [139]

PDT agents can be introduced in to SiNPs by encapsulating or covalent bonding.[140-142] The PAG agents in this dissertation can also be encapsulated inside or attached outside SiNPs. Considering that PAGs works by release acid in to cells, attaching them to the periphery would be more preferable.

Before further modification and application, properties of encapsulated SiNPs, such as size distribution, spectrum, and viability need to be characterized. Sizes around 20 nm would be ideal for good cell uptake efficiency.[143] Meanwhile, sizes between 10-20 nm will permit longer distribution times in the circulatory system, with efficient clearance by the kidneys and liver.[144]

6.2 RGD Peptide Functionalized Silica Nanoparticles

Functionalization at the surface of nanoparticles has been widely applied for targeting. Tumor selective targeting has been demonstrated by applying functionalized SiNPs in mice.[2, 134] RGD peptides have been well demonstrated for its selective binding properties with tumor vasculatures. RGD can be introduced into a SiNP system by applying bifunctional PEG groups, with the maleimide ending bind to the thiol group on the SiNP surface and use N-hydroxysuccinimide to react with the primary amine group of RGD (a lysine residue).

6.3 Live Animal Treatment and Imaging

The advantage of deeper penetration of 2PA excitation can be exhibited in the live animal experiments. By studying the tumor environment without sacrificing the animal model, it can reduce the number of models used in experiments. In addition, use of a window chamber leads to better comparison by tracking the cancer progression on the individual model. For imaging in live animals, such as mice, the window chamber can be applied[145, 146] (**Figure 6-2**). After tumor cells are injected under skin, a window chamber will be implanted on the same area days after. (**Figure 6-3**) Skin at one side of the chamber is open, so the tumor is exposed and can be imaged through a coverslip window.

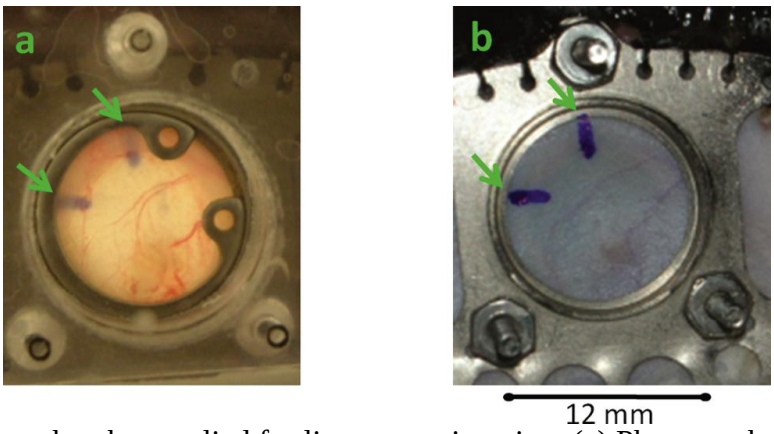

Figure 6-2. Window chamber applied for live mouse imaging. (a) Photograph from coverslip side and (b) photograph (mirror image) from skin side. The window chamber had a diameter of 12 mm.[145]

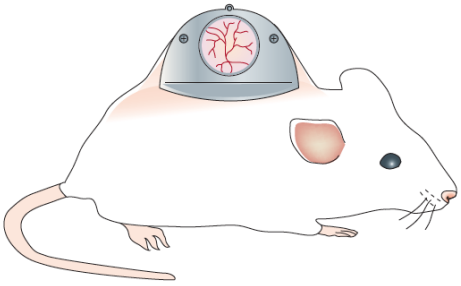

Figure 6-3. Implantation of the window chamber on the skin of a mouse.[146]

Functionalized SiNPs encapsulated with 2PA probes will then be injected into mice through the tail vein every day. Vasculature growth during tumor progression can be detected by 2PA fluorescence imaging using an upright microscope.

For PDT therapy, SiNPs containing both 2PA probes and PAGs will be injected into mice through the tail vein. Fluorescence from 2PA probes can employed to demonstrate the distribution of SiNPs in the tumor area. PDT treatment can then be performed by exposure of the tumor area with near-IR light also by 2PA, just tuned to a difference wavelength than used for imaging. Treatment efficiency can be evaluated by measuring the tumor sizes in the window chamber. Change of tumor vasculature during PDT can also be tracked by fluorescence imaging of 2PA probes.

APPENDIX: LIST OF PUBLICATIONS DURING PH.D. DISSERTATION

1. Zhang, Y.; Yue, X.; Kim, B.; Yao, S.; *Belfield, K. D. “Deoxyribonucleoside-Modified Squaraines as Near-IR Viscosity Sensors” *Chemistry A European Journal* 2014, *20*, 7249-7253

2. Zhang, Y.; Yue, X.; Kim, B.; Yao, S.; Bondar, M. V.; *Belfield, K. D. “Sensing and Labeling Bovine Serum Albumin (BSA) with Fluorogenic Near-IR-emitting Squarine Dyes” *ACS Applied Materials and Interfaces* 2013, *5*, 8710-8717.

3. Zhang, X.; *Xiao, Y.; Qi, J.; *Qu, J.; Kim, B.; Yue, X.; *Belfield, K. D. “Longwavelength, Photostable, Two-photon Excitable BODIPY Fluorophores Readily Modifiable for Molecular Probes*” Journal of Organic Chemistry*, 2013, *78*, 9153-9160.

4. Yanez, C.O.; Morales, A. R.; Yue, X.; Urakami, T.; Komatsu, M.; Jarvinen, T. A. H.; *Belfield, K. D. “Deep Vascular Imaging in Wounds by Two-Photon Fluorescence Microscopy” *PLoS ONE* 2013, *8(7)*, e67559.

5. Yue, X.; Yanez, C. O.; Yao, S.; *Belfield, K. D. “Selective Cell Death by Photochemically Induced pH Imbalance in Cancer Cells*” Journal of the American Chemical Society* 2013, *135*, 2112-2115.

6. *Belfield, K. D.; Bondar, M. V.; Morales, A. R.; Yue, X.; Luchita, G.; Przhonska, O. V.; Kachkovsky, O. D. “Two-Photon Absorption and Time-Resolved Stimulated Emission Depletion Spectroscopy of a New Fluorenyl Derivative” *ChemPhysChem* 2012, *13*, 3481-3491.

7. *Belfield, K. D.; Bondar, M. V.; Morales, A. R.; Yue, X.; Luchita, G.; Przhonska, O. V. “Transient Excited-state Absorption and Gain Spectroscopy of a Two-Photon Absorbing Probe with Efficient Superfluorescent Properties” *Journal of Physical Chemistry C* 2012, *116*, 11261-11271.

REFERENCES

1. Belfield, K. D.; Yao, S.; Bondar, M. V., Two-photon Absorbing Photonic Materials: From Fundamentals to Applications. *Adv Polym Sci* **2008,** *213*, 97-156.
2. Wang, X. H.; Morales, A. R.; Urakami, T.; Zhang, L. F.; Bondar, M. V.; Komatsu, M.; Belfield, K. D., Folate Receptor-Targeted Aggregation-Enhanced Near-IR Emitting Silica Nanoprobe for One-Photon in Vivo and Two-Photon ex Vivo Fluorescence Bioimaging. *Bioconjugate Chemistry* **2011,** *22* (7), 1438-1450.
3. Yanez, C. O.; Morales, A. R.; Yue, X. L.; Urakami, T.; Komatsu, M.; Jarvinen, T. A. H.; Belfield, K. D., Deep Vascular Imaging in Wounds by Two-Photon Fluorescence Microscopy. *Plos One* **2013,** *8* (7).
4. Schenke-Layland, K.; Riemann, I.; Damour, O.; Stock, U. A.; Konig, K., Two-photon microscopes and in vivo multiphoton tomographs - Powerful dicagnostic tools for tissue engineering and drug delivery. *Advanced Drug Delivery Reviews* **2006,** *58* (7), 878-896.
5. Bisland, S. K.; Lilge, L.; Lin, A.; Rusnov, R.; Bogaards, A.; Wilson, B. C., Metronomic photodynamic therapy as a new paradigm for photodynamic therapy: Rationale and preclinical evaluation of technical feasibility for treating malignant brain tumors (vol 80, pg 22, 2004). *Photochem Photobiol* **2004,** *80* (2), 373-373.
6. Bhawalkar, J. D.; Kumar, N. D.; Zhao, C. F.; Prasad, P. N., Two-photon photodynamic therapy. *Journal of clinical laser medicine & surgery* **1997,** *15* (5), 201-4.
7. Yue, X.; Yanez, C. O.; Yao, S.; Belfield, K. D., Selective cell death by photochemically induced pH imbalance in cancer cells. *J Am Chem Soc* **2013,** *135* (6), 2112-5.
8. Belfield, K. D.; Yanez, C. O.; Yao, S.; Huang, Z. L.; Corredor, C. C., Improved photosensitive polymeric materials for 3-D WORM optical data storage using two-photon fluorescent writing and readout. *Abstr Pap Am Chem S* **2007,** *233*.
9. Belfield, K. D.; Yanez, C. O.; Andrade, C. D.; Yao, S., POLY 598-New photosensitive polymeric materials for two-photon 3-D WORM optical data storage. *Abstr Pap Am Chem S* **2008,** *236*.
10. Yanez, C. O.; Andrade, C. D.; Yao, S.; Luchita, G.; Bondar, M. V.; Belfield, K. D., Photosensitive Polymeric Materials for Two-Photon 3D WORM Optical Data Storage Systems. *Acs Appl Mater Inter* **2009,** *1* (10), 2219-2229.
11. Barnard, E. S.; Hoke, E. T.; Connor, S. T.; Groves, J. R.; Kuykendall, T.; Yan, Z.; Samulon, E. C.; Bourret-Courchesne, E. D.; Aloni, S.; Schuck, P. J.; Peters, C. H.; Hardin, B. E., Probing carrier lifetimes in photovoltaic materials using subsurface two-photon microscopy. *Sci Rep-Uk* **2013,** *3*.
12. Morales, A. R.; Belfield, K. D.; Hales, J. M.; Van Stryland, E. W.; Hagan, D. J., Synthesis of two-photon absorbing unsymmetrical fluorenyl-based chromophores. *Chem Mater* **2006,** *18* (20), 4972-4980.
13. Yao, S.; Belfield, K. D., Two-Photon Fluorescent Probes for Bioimaging. *Eur J Org Chem* **2012,** (17), 3199-3217.
14. Wang, X. H.; Nguyen, D. M.; Yanez, C. O.; Rodriguez, L.; Ahn, H. Y.; Bonder, M. V.; Belfield, K. D., High-Fidelity Hydrophilic Probe for Two-Photon Fluorescence Lysosomal Imaging. *Journal of the American Chemical Society* **2010,** *132* (35), 12237-12239.

15. Yao, S.; Schafer-Hales, K. J.; Belfield, K. D., A new water-soluble near-neutral ratiometric fluorescent pH indicator. *Org Lett* **2007,** *9* (26), 5645-5648.
16. Torchilin, V. P., Micellar nanocarriers: Pharmaceutical perspectives. *Pharm Res* **2007,** *24* (1), 1-16.
17. Coimbra, M.; Isacchi, B.; van Bloois, L.; Torano, J. S.; Ket, A.; Wu, X. J.; Broere, F.; Metselaar, J. M.; Rijcken, C. J. F.; Storm, G.; Bilia, R.; Schiffelers, R. M., Improving solubility and chemical stability of natural compounds for medicinal use by incorporation into liposomes. *Int J Pharmaceut* **2011,** *416* (2), 433-442.
18. Wang, Z. L.; Hao, J. H.; Chan, H. L. W.; Law, G. L.; Wong, W. T.; Wong, K. L.; Murphy, M. B.; Su, T.; Zhang, Z. H.; Zeng, S. Q., Simultaneous synthesis and functionalization of water-soluble up-conversion nanoparticles for in-vitro cell and nude mouse imaging. *Nanoscale* **2011,** *3* (5), 2175-2181.
19. Allison, R. R.; Downie, G. H.; Cuenca, R.; Hu, X. H.; Childs, C. J. H.; Sibata, C. H., Photosensitizers in clinical PDT. *Photodiagn Photodyn* **2004,** *1* (1), 27-42.
20. Wang, I.; Bendsoe, N.; Klinteberg, C. A. F.; Enejder, A. M. K.; Andersson-Engels, S.; Svanberg, S.; Svanberg, K., Photodynamic therapy vs. cryosurgery of basal cell carcinomas: results of a phase III clinical trial. *Brit J Dermatol* **2001,** *144* (4), 832-840.
21. Morton, C. A.; Whitehurst, C.; McColl, J. H.; Moore, J. V.; MacKie, R. M., Photodynamic therapy for large or multiple patches of Bowen disease and basal cell carcinoma. *Arch Dermatol* **2001,** *137* (3), 319-324.
22. Sibata, C. H.; Colussi, V. C.; Oleinick, N. L.; Kinsella, T. J., Photodynamic therapy: a new concept in medical treatment. *Brazilian journal of medical and biological research = Revista brasileira de pesquisas medicas e biologicas / Sociedade Brasileira de Biofisica ... [et al.]* **2000,** *33* (8), 869-80.
23. Kato, H.; Okunaka, T.; Konaka, C., [Photodynamic therapy for bronchogenic carcinoma]. *Nihon Geka Gakkai zasshi* **1997,** *98* (1), 36-40.
24. Runfola, M. A.; Weber, T. K.; Rodriguez-Bigas, M. A.; Dougherty, T. J.; Petrelli, N. J., Photodynamic therapy for residual neoplasms of the perianal skin. *Dis Colon Rectum* **2000,** *43* (4), 499-502.
25. Popovic, E. A.; Kaye, A. H.; Hill, J. S., Photodynamic therapy of brain tumors. *Journal of clinical laser medicine & surgery* **1996,** *14* (5), 251-61.
26. Mennel, S.; Barbazetto, I.; Meyer, C. H.; Peter, S.; Stur, M., Ocular photodynamic therapy - Standard applications and new indications (Part 1). *Ophthalmologica* **2007,** *221* (4), 216-226.
27. Brown, S. B.; Brown, E. A.; Walker, I., The present and future role of photodynamic therapy in cancer treatment. *Lancet Oncol* **2004,** *5* (8), 497-508.
28. Wilson, B. C.; Patterson, M. S., The physics, biophysics and technology of photodynamic therapy. *Phys Med Biol* **2008,** *53* (9), R61-R109.
29. Maruo, S.; Nakamura, O.; Kawata, S., Three-dimensional microfabrication with two-photon-absorbed photopolymerization. *Optics Letters* **1997,** *22* (2), 132-134.
30. Parthenopoulos, D. A.; Rentzepis, P. M., 3-DIMENSIONAL OPTICAL STORAGE MEMORY. *Science* **1989,** *245* (4920), 843-845.

31. Strickler, J. H.; Webb, W. W., 3-DIMENSIONAL OPTICAL-DATA STORAGE IN REFRACTIVE MEDIA BY 2-PHOTON POINT EXCITATION. *Optics Letters* **1991,** *16* (22), 1780-1782.
32. Wagnieres, G. A.; Star, W. M.; Wilson, B. C., In vivo fluorescence spectroscopy and imaging for oncological applications. *Photochem Photobiol* **1998,** *68* (5), 603-632.
33. Gillenwater, A.; Jacob, R.; Richards-Kortum, R., Fluorescence spectroscopy: A technique with potential to improve the early detection of aerodigestive tract neoplasia. *Head Neck-J Sci Spec* **1998,** *20* (6), 556-562.
34. Chen, Y. C.; Lo, C. L.; Hsiue, G. H., Multifunctional nanomicellar systems for delivering anticancer drugs. *J Biomed Mater Res A* **2014,** *102* (6), 2024-2038.
35. Rumi, M.; Barlow, S.; Wang, J.; Perry, J. W.; Marder, S. R., Two-Photon Absorbing Materials and Two-Photon-induced Chemistry. *Adv Polym Sci* **2008,** *213*, 1-95.
36. Rumi, M.; Ehrlich, J. E.; Heikal, A. A.; Perry, J. W.; Barlow, S.; Hu, Z. Y.; McCord-Maughon, D.; Parker, T. C.; Rockel, H.; Thayumanavan, S.; Marder, S. R.; Beljonne, D.; Bredas, J. L., Structure-property relationships for two-photon absorbing chromophores: Bis-donor diphenylpolyene and bis(styryl)benzene derivatives. *Journal of the American Chemical Society* **2000,** *122* (39), 9500-9510.
37. Albota, M.; Beljonne, D.; Bredas, J. L.; Ehrlich, J. E.; Fu, J. Y.; Heikal, A. A.; Hess, S. E.; Kogej, T.; Levin, M. D.; Marder, S. R.; McCord-Maughon, D.; Perry, J. W.; Rockel, H.; Rumi, M.; Subramaniam, C.; Webb, W. W.; Wu, X. L.; Xu, C., Design of organic molecules with large two-photon absorption cross sections. *Science* **1998,** *281* (5383), 1653-1656.
38. Audebert, P.; Kamada, K.; Matsunaga, K.; Ohta, K., The third-order NLO properties of D-pi-A molecules with changing a primary amino group into pyrrole. *Chem Phys Lett* **2003,** *367* (1-2), 62-71.
39. Cherioux, F.; Maillotte, H.; Dudley, J. M.; Audebert, P., Enhancement of non-resonant non-linear refractive index with reduction of absorption in push-pull molecules by reduction of their donor group strength. *Chem Phys Lett* **2000,** *319* (5-6), 669-673.
40. Yang, W. J.; Kim, D. Y.; Jeong, M. Y.; Kim, H. M.; Jeon, S. J.; Cho, B. R., 2,6-Bis(styryl)anthracene derivatives with large two-photon cross-sections. *Chemical Communications* **2003,** (20), 2618-2619.
41. Kamada, K.; Ohta, K.; Yoichiro, I.; Kondo, K., Two-photon absorption properties of symmetric substituted diacetylene: drastic enhancement of the cross section near the one-photon absorption peak. *Chem Phys Lett* **2003,** *372* (3-4), 386-393.
42. Mongin, O.; Porres, L.; Charlot, M.; Katan, C.; Blanchard-Desce, M., Synthesis, fluorescence, and two-photon absorption of a series of elongated rodlike and banana-shaped quadrupolar fluorophores: A comprehensive study of structure-property relationships. *Chem-Eur J* **2007,** *13* (5), 1481-1498.
43. Sato, K.; Okazaki, S.; Yamagishi, T.; Arai, S., The synthesis of azoniadithia[6]helicenes. *J. Heterocyclic Chem.* **2004,** *41*, 443-447.
44. Osbond, J. M., Chemical constitution and amoebicidal activity. VI. A new synthesis of 2-ketones and 2-alcohols derived from 3-alkyl-1,3,4,6,7,11b hexahydro-9,10-dimethoxy-2H-benzo-[a]quinolizines. *J. Chem. Soc.* **1961**, 4711-4718.

45. Tian, M.; Ihmels, H., Selective colorimetric detection of Hg^{2+} and Mg^{2+} with crown ether substituted *N*-Aryl-9-aminobenzo[b]quinolizinium derivatives. *Eur. J. Org. Chem.* **2011**, 4145-4153.
46. Tian, M.; Ihmels, H.; Ye, S., Fluorimetric detection of Mg^{2+} and DNA with 9-(alkoxyphenyl)benzo[b]quinolizinium derivatives. *Org. Biomol. Chem.* **2012,** *10*, 3010-3018.
47. Ihmels, H.; Salbach, A., Efficient photoinduced DNA damage by coralyne. *Photochem. Photobiol.* **2006,** *82*, 1572-1576.
48. Ihmels, H.; Faulhaber, K.; Vedaldi, D.; Dall'Acqua, F.; Viola, G., Intercalation of organic dye molecules into double-stranded DNA. Part 2: The annelated quinolizinium ion as a structural motif in DNA intercalators. *Photochem. Photobiol.* **2005,** *81*, 1107-1115.
49. Viola, G.; Bressanini, M.; Gabellini, N.; Vedaldi, D.; Dall'Acqua, F.; Ihmels, H., Naphthoquinolizinium derivatives as a novel platform for DNA-binding and DNA-photodamaging chromophores. *Photochem. Photobiol. Sci.* **2002,** *1*, 882-889.
50. Zhuo, G.; Wang, X.; Wang, D.; Wang, C.; Zhao, X.; Shao, Z.; Jiang, M., Two-photon induced optical-power limiting and upconverted superradiance properties of a new organic dye HEASPI. *Opt. Laser Technol.* **2001,** *33*, 209-212.
51. Bellier, Q.; Makarov, N. S.; Bouit, P.-A.; Rigaut, S.; Kamada, K.; Feneyrou, P.; Berginc, G.; Maury, O.; Perry, J. W.; Andraud, C., Excited state absorption: a key phenomenon for the improvement of biphotonic based optical limiting at telecommunication wavelengths. *Phys. Chem. Chem. Phys., 2012, 14, 15299–15307* **2012,** *14*, 15299-15307.
52. Kopylova, T. N.; Svetlichnyi, V. A.; Mayer, G. V.; Reznichenko, A. V.; Podgaetskii, V. M.; Ponomareva, O. V.; Samsonova, L. G.; Filinov, D. N.; Pomogaev, V. A.; Tel'minov, E. N.; Lapin, I. N.; Svetlichnaya, N. N.; Sinchenko, E. I., Limitation of high-power optical radiation by organic molecules: I. Substituted pyranes and cyanine dyes. *Quantum Electron.* **2003,** *33* (11), 967-974.
53. Macoas, E.; Marcelo, G.; Pinto, S.; Caneque, T.; Cuadro, A. M.; Vaquero, J. J.; Martinho, J. M. G., A V-shaped cationic dye for nonlinear optical bioimaging. *Chem. Commun.* **2011,** *47*, 7374-7376.
54. Zhou, S.; Zhang, Q.; Tian, X.; Hu, G.; Hao, F.; Wu, J.; Tian, Y., Synthesis, crystal structure, optical properties, DNA-binding and cell imaging of an organic chromophore. *Dyes Pigm.* **2011,** *92*, 689-695.
55. Nag, O. K.; Nayak, R. R.; Lim, C. S.; Kim, I. H.; Kyhm, K.; Cho, B. R.; Woo, H. Y., Two-photon absorption properties of cationic 1,4-bis(styryl)benzene derivative and its inclusion complexes with cyclodextrins. *J. Phys. Chem. B* **2010,** *114*, 9684-9690.
56. Ho, H.-A.; Najari, A.; Leclerc, M., Optical detection of DNA and proteins with cationic polythiophenes. *Acc. Chem. Res.* **2008,** *41* (2), 168-178.
57. Granzhan, A.; Ihmels, H., *N*-Aryl-9-amino-substituted acridizinium derivatives as fluorescent "light-up" probes for DNA and protein detection. *Org. Lett.* **2005,** *7* (23), 5119-5122.
58. Faulhaber, K.; Granzhan, A.; Ihmels, H.; Otto, D.; Thomas, L.; Wells, S., Studies of the fluorescence light-up effect of amino-substituted benzo[*b*]quinolizinium derivatives in the presence of biomacromolecules. *Photochem. Photobiol. Sci.* **2011,** *10*, 1535-1545.
59. Tokar, V. P.; Losytskyy, M. Y.; Ohulchanskyy, T. Y.; Kryvorotenko, D. V.; Kovalska, V. B.; Balanda, A. O.; Dmytruk, I. M.; Prokopets, V. M.; Yarmoluk, S. M.; Yashchuk, V. M.,

Styryl dyes as two-photon excited fluorescent probes for DNA detection and two-photon laser scanning fluorescence microscopy of living cells. *J. Fluoresc.* **2010,** *20*, 865-872.
60. Yashchuk, V. M.; Yu.Kudrya, V. Y.; Losytskyy, M. Y.; Tokar, V. P.; Yarmoluk, S. M.; Dmytruk, I. M.; Prokopets, V. M.; Kovalska, V. B.; Balanda, A. O.; Kryvorotenko, D. V.; Ogul'chansky, T. Y., The optical biomedical sensors for the DNA detection and imaging based on two-photon excited luminescent styryl dyes. Phototoxic influence on the DNA. *Proc. SPIE* **2007,** *6796*, 67960M/1-14.
61. Wang, J.; Burdzinski, G.; Zhu, Z.; Platz, M. S.; Carra, C.; Bally, T., Ultrafast spectroscopic and matrix isolation studies of *p*-biphenylyl, *o*-biphenylyl, and 1-Naphthylnitrenium cations. *J. Am. Chem. Soc.* **2007,** *129*, 8380-8388.
62. Malval, J.-P.; Chaumeil, H.; Rettig, W.; Kharlanov, V.; Diemer, V.; Ay, E.; Morlet-Savary, F.; Poizat, O., Excited-state dynamics of phenol–pyridinium biaryl. *Phys. Chem. Chem. Phys.* **2012,** *14*, 562-574.
63. Furuta, K.; Fuyuki, M.; Wada, A., Multiphoton reaction of DTTCI observed by femtosecond pump-probe and two-pulse correlation measurements. *Chem. Phys.* **2013,** *418*, 42-46.
64. Ramírez, M. A.; Cuadro, A. M.; Alvarez-Builla, J.; Castaño, O.; Andrés, J. L.; Mendicuti, F.; Clays, K.; Asselberghs, I.; Vaquero, J. J., Donor-(p-bridge)-azinium as D-p-A^+ one-dimensional and D-p-A^+-p-D multidimensional V-shaped chromophores. *Org. Biomol. Chem.* **2012,** *10* 1659-1669.
65. Faulhaber, K.; Granzhan, A.; Ihmels, H.; Viola, G., Detection of biomacromolecules with fluorescent light-up probes. *Pure Appl. Chem.* **2006,** *78* (12).
66. Barbafina, A.; Amelia, M.; Latterini, L.; Aloisi, G. G.; Elisei, F., Photophysical properties of quinolizinium salts and their interactions with DNA in aqueous solution. *J. Phys. Chem. A* **2009,** *113*, 14514-14520.
67. Vinothkumar, K. R.; Henderson, R., Structures of membrane proteins. *Q Rev Biophys* **2010,** *43* (1), 65-158.
68. Goldmann, W. H.; Auernheimer, V.; Thievessen, I.; Ben, F., Vinculin, cell mechanics and tumour cell invasion. *Cell Biol Int* **2013,** *37* (5), 397-405.
69. Carisey, A.; Ballestrem, C., Vinculin, an adapter protein in control of cell adhesion signalling. *Eur J Cell Biol* **2011,** *90* (2-3), 157-163.
70. Seedher, N.; Kanojia, M., Mechanism of interaction of hypoglycemic agents glimepiride and glipizide with human serum albumin. *Cent. Eur. J. Chem.* **2009,** *7* (1), 96-104.
71. Seedher, N.; Agarwal, P., Competitive binding of fluoroquinolone antibiotics and some other drugs to human serum albumin: a luminescence spectroscopic study. *Luminescence* **2013,** *28* (4), 562-568.
72. Meier, H.; Petermann, R.; Gerold, J., Bathochromic or hypsochromic effects via the extension of conjugation: a study of stilbenoid squaraines. *Chem. Commun.* **1999**, 977-978.
73. Sheik-Bahae, M.; Said, A. A.; Wei, T. H.; Hagan, D. J.; Van Stryland, E. W., Sensitive measurement of optical nonlinearities using a single beam. *IEEE J. Quantum Elect.* **1990,** *26* (4), 760-769.
74. Khan, A. Y.; Hossain, M.; Kumar, G. S., Binding of plant alkaloids berberine and palmatine to serum albumins: a thermodynamic investigation. *Mol. Biol. Rep.* **2013,** *40* (1), 553-566.

75. Chang, K. J.; Bennett, V.; Cuatrecasas, P., Membrane receptors as general markers for plasma-membrane isolation procedures - Use of I 125-labeled wheat-germ agglutinin, insulin, and cholera toxin. *J. Biol. Chem.* **1975,** *250* (2), 488-500.
76. Abou-Zied, O. K.; Al-Shihi, O. I. K., Characterization of subdomain IIA binding site of human serum albumin in its native, unfolded, and refolded states using small molecular probes. *Journal of the American Chemical Society* **2008,** *130* (32), 10793-10801.
77. Khan, A. Y.; Hossain, M.; Kumar, G. S., Binding of plant alkaloids berberine and palmatine to serum albumins: a thermodynamic investigation. *Mol Biol Rep* **2013,** *40* (1), 553-566.
78. Corredor, C. C.; Belfield, K. D.; Bondar, M. V.; Przhonska, O. V.; Yao, S., One- and two-photon photochemical stability of linear and branched fluorene derivatives. *J. Photoch. Photobio. A* **2006,** *184* (1-2), 105-112.
79. Janssen, M. E. W.; Kim, E.; Liu, H. J.; Fujimoto, L. M.; Bobkov, A.; Volkmann, N.; Hanein, D., Three-dimensional structure of vinculin bound to actin filaments. *Mol Cell* **2006,** *21* (2), 271-281.
80. Fukumura, D.; Duda, D. G.; Munn, L. L.; Jain, R. K., Tumor Microvasculature and Microenvironment: Novel Insights Through Intravital Imaging in Pre-Clinical Models. *Microcirculation* **2010,** *17* (3), 206-225.
81. Provenzano, P. P.; Eliceiri, K. W.; Keely, P. J., Multiphoton microscopy and fluorescence lifetime imaging microscopy (FLIM) to monitor metastasis and the tumor microenvironment. *Clin Exp Metastas* **2009,** *26* (4), 357-370.
82. Tozer, G. M.; Ameer-Beg, S. M.; Baker, J.; Barber, P. R.; Hill, S. A.; Hodgkiss, R. J.; Locke, R.; Prise, V. E.; Wilson, I.; Vojnovic, B., Intravital imaging of tumour vascular networks using multi-photon fluorescence microscopy. *Advanced Drug Delivery Reviews* **2005,** *57* (1), 135-152.
83. Beerling, E.; Ritsma, L.; Vrisekoop, N.; Derksen, P. W. B.; van Rheenen, J., Intravital microscopy: new insights into metastasis of tumors. *J Cell Sci* **2011,** *124* (3), 299-310.
84. Hirano, Y.; Kando, Y.; Hayashi, T.; Goto, K.; Nakajima, A., SYNTHESIS AND CELL ATTACHMENT ACTIVITY OF BIOACTIVE OLIGOPEPTIDES - RGD, RGDS, RGDV, AND RGDT. *Journal of Biomedical Materials Research* **1991,** *25* (12), 1523-1534.
85. Dechantsreiter, M. A.; Planker, E.; Matha, B.; Lohof, E.; Holzemann, G.; Jonczyk, A.; Goodman, S. L.; Kessler, H., N-methylated cyclic RGD peptides as highly active and selective alpha(v)beta(3) integrin antagonists. *Journal of Medicinal Chemistry* **1999,** *42* (16), 3033-3040.
86. Lim, S. T.; Chun, M. H.; Lee, K. W.; Shin, D. M., Organic light emitting diodes with red emission using (2,6-dimethyl-4H-pyran-4 '-ylidene)malononitrile moiety. *Opt Mater* **2003,** *21* (1-3), 217-220.
87. Andreu, R.; Galan, E.; Garin, J.; Herrero, V.; Lacarra, E.; Orduna, J.; Alicante, R.; Villacampa, B., Linear and V-Shaped Nonlinear Optical Chromophores with Multiple 4H-Pyran-4-ylidene Moieties. *Journal of Organic Chemistry* **2010,** *75* (5), 1684-1692.
88. Qin, W.; Ding, D.; Liu, J. Z.; Yuan, W. Z.; Hu, Y.; Liu, B.; Tang, B. Z., Biocompatible Nanoparticles with Aggregation-Induced Emission Characteristics as Far-Red/Near-Infrared Fluorescent Bioprobes for In Vitro and In Vivo Imaging Applications. *Adv Funct Mater* **2012,** *22* (4), 771-779.

89. Geng, J. L.; Li, K.; Ding, D.; Zhang, X. H.; Qin, W.; Liu, J. Z.; Tang, B. Z.; Liu, B., Lipid-PEG-Folate Encapsulated Nanoparticles with Aggregation Induced Emission Characteristics: Cellular Uptake Mechanism and Two-Photon Fluorescence Imaging. *Small* **2012,** *8* (23), 3655-3663.
90. Kim, D. Y.; Kim, J. N.; Kim, H. J., 2-{2-[4-(Dimethylamino)phenyl]-6-methyl-4H-pyran-4-ylidene}malononitrile: a colorimetric and fluorescent chemosensor for low pH values. *Spectrochimica acta. Part A, Molecular and biomolecular spectroscopy* **2014,** *122*, 304-8.
91. Deryugina, E. I.; Bourdon, M. A.; Jungwirth, K.; Smith, J. W.; Strongin, A. Y., Functional activation of integrin alpha V beta 3 in tumor cells expressing membrane-type 1 matrix metalloproteinase. *International journal of cancer. Journal international du cancer* **2000,** *86* (1), 15-23.
92. Tong, H.; Hong, Y. N.; Dong, Y. Q.; Ren, Y.; Haussler, M.; Lam, J. W. Y.; Wong, K. S.; Tang, B. Z., Color-tunable, aggregation-induced emission of a butterfly-shaped molecule comprising a pyran skeleton and two cholesteryl wings. *J Phys Chem B* **2007,** *111* (8), 2000-2007.
93. Pecher, J.; Huber, J.; Winterhalder, M.; Zumbusch, A.; Mecking, S., Tailor-Made Conjugated Polymer Nanoparticles for Multicolor and Multiphoton Cell Imaging. *Biomacromolecules* **2010,** *11* (10), 2776-2780.
94. Popovic, Z.; Liu, W.; Chauhan, V. P.; Lee, J.; Wong, C.; Greytak, A. B.; Insin, N.; Nocera, D. G.; Fukumura, D.; Jain, R. K.; Bawendi, M. G., A nanoparticle size series for in vivo fluorescence imaging. *Angewandte Chemie* **2010,** *49* (46), 8649-52.
95. Nishida, N.; Yano, H.; Nishida, T.; Kamura, T.; Kojiro, M., Angiogenesis in cancer. *Vascular health and risk management* **2006,** *2* (3), 213-9.
96. Avraamides, C. J.; Garmy-Susini, B.; Varner, J. A., Integrins in angiogenesis and lymphangiogenesis. *Nat Rev Cancer* **2008,** *8* (8), 604-617.
97. Brooks, P. C.; Clark, R. A.; Cheresh, D. A., Requirement of vascular integrin alpha v beta 3 for angiogenesis. *Science* **1994,** *264* (5158), 569-71.
98. Friedlander, M.; Brooks, P. C.; Shaffer, R. W.; Kincaid, C. M.; Varner, J. A.; Cheresh, D. A., Definition of two angiogenic pathways by distinct alpha v integrins. *Science* **1995,** *270* (5241), 1500-2.
99. Pfaff, M.; Tangemann, K.; Muller, B.; Gurrath, M.; Muller, G.; Kessler, H.; Timpl, R.; Engel, J., Selective Recognition of Cyclic Rgd Peptides of Nmr Defined Conformation by Alpha-Ii-Beta-3, Alpha-V-Beta-3, and Alpha-5-Beta-1 Integrins. *J Biol Chem* **1994,** *269* (32), 20233-20238.
100. Denk, W.; Svoboda, K., Photon upmanship: Why multiphoton imaging is more than a gimmick. *Neuron* **1997,** *18* (3), 351-357.
101. Oheim, M.; Beaurepaire, E.; Chaigneau, E.; Mertz, J.; Charpak, S., Two-photon microscopy in brain tissue: parameters influencing the imaging depth. *Journal of Neuroscience Methods* **2001,** *111* (1), 29-37.
102. Konig, K.; Riemann, I., High-resolution multiphoton tomography of human skin with subcellular spatial resolution and picosecond time resolution. *Journal of Biomedical Optics* **2003,** *8* (3), 432-439.
103. So, P. T. C.; Kim, H.; Kochevar, I. E., Two-photon deep tissue ex vivo imaging of mouse dermal and subcutaneous structures. *Optics Express* **1998,** *3* (9), 339-350.

104. Kobat, D.; Horton, N. G.; Xu, C., In vivo two-photon microscopy to 1.6-mm depth in mouse cortex. *Journal of Biomedical Optics* **2011,** *16* (10).
105. Chen, W.-L.; Chou, C.-K.; Lin, M.-G.; Chen, Y.-F.; Jee, S.-H.; Tan, H.-Y.; Tsai, T.-H.; Kim, K.-H.; Kim, D.; So, P. T. C.; Lin, S.-J.; Dong, C.-Y., Single-wavelength reflected confocal and multiphoton microscopy for tissue imaging. *Journal of Biomedical Optics* **2009,** - *14* (- 5), - 054026.
106. Ruoslahti, E., RGD and other recognition sequences for integrins. *Annual Review of Cell and Developmental Biology* **1996,** *12*, 697-715.
107. Morales, A. R.; Luchita, G.; Yanez, C. O.; Bondar, M. V.; Przhonska, O. V.; Belfield, K. D., Linear and nonlinear photophysics and bioimaging of an integrin-targeting water-soluble fluorenyl probe. *Organic & Biomolecular Chemistry* **2010,** *8* (11), 2600-2608.
108. Brooks, P. C.; Clark, R. A. F.; Cheresh, D. A., REQUIREMENT OF VASCULAR INTEGRIN ALPHA(V)BETA(3) FOR ANGIOGENESIS. *Science* **1994,** *264* (5158), 569-571.
109. Cavani, A.; Zambruno, G.; Marconi, A.; Manca, V.; Marchetti, M.; Giannetti, A., DISTINCTIVE INTEGRIN EXPRESSION IN THE NEWLY FORMING EPIDERMIS DURING WOUND-HEALING IN HUMANS. *J. Invest. Dermatol.* **1993,** *101* (4), 600-604.
110. Jarvinen, T. A. H.; Ruoslahti, E., Target-seeking antifibrotic compound enhances wound healing and suppresses scar formation in mice. *Proceedings of the National Academy of Sciences of the United States of America* **2010,** *107* (50), 21671-21676.
111. Pawlicki, M.; Collins, H. A.; Denning, R. G.; Anderson, H. L., Two-Photon Absorption and the Design of Two-Photon Dyes. *Angewandte Chemie-International Edition* **2009,** *48* (18), 3244-3266.
112. Peticola.Wl, MULTIPHOTON SPECTROSCOPY. *Annual Review of Physical Chemistry* **1967,** *18*, 233-&.
113. Stadelmann, W. K.; Digenis, A. G.; Tobin, G. R., Physiology and healing dynamics of chronic cutaneous wounds. *Am J Surg* **1998,** *176* (2A Suppl), 26S-38S.
114. Zhu, T. C.; Finlay, J. C.; Hahn, S. M., Determination of the distribution of light, optical properties, drug concentration, and tissue oxygenation in-vivo in human prostate during motexafin lutetium-mediated photodynamic therapy. *Journal of Photochemistry and Photobiology B: Biology* **2005,** *79* (3), 231-241.
115. Moore, R. B.; Chapman, J. D.; Mercer, J. R.; Mannan, R. H.; Wiebe, L. I.; McEwan, A. J.; McPhee, M. S., MEASUREMENT OF PDT-INDUCED HYPOXIA IN DUNNING PROSTATE TUMORS BY IODINE-123-IODOAZOMYCIN ARABINOSIDE. *Journal of Nuclear Medicine* **1993,** *34* (3), 405-411.
116. Brown, J. M.; William, W. R., Exploiting tumour hypoxia in cancer treatment. *Nature Reviews: Cancer* **2004,** *4* (6), 437-447.
117. Yanez, C. O.; Andrade, C. D.; Belfield, K. D., Characterization of novel sulfonium photoacid generators and their microwave-assisted synthesis. *Chemical Communications* **2009,** (7), 827-829.
118. Escobar-Chavez, J. J.; Lopez-Cervantes, M.; Naik, A.; Kalia, Y. N.; Quintanar-Guerrero, D.; Ganem-Quintanar, A., Applications of thermoreversible pluronic F-127 gels in pharmaceutical formulations. *Journal of Pharmacy and Pharmaceutical Sciences* **2006,** *9* (3), 339-358.

119. Batrakova, E. V.; Kabanov, A. V., Pluronic block copolymers: Evolution of drug delivery concept from inert nanocarriers to biological response modifiers. *Journal of Controlled Release* **2008,** *130* (2), 98-106.
120. Sahay, G.; Batrakova, E. V.; Kabanov, A. V., Different Internalization Pathways of Polymeric Micelles and Unimers and Their Effects on Vesicular Transport. *Bioconjugate Chemistry* **2008,** *19* (10), 2023-2029.
121. Batrakova, E. V.; Li, S.; Vinogradov, S. V.; Alakhov, V. Y.; Miller, D. W.; Kabanov, A. V., Mechanism of pluronic effect on P-glycoprotein efflux system in blood-brain barrier: Contributions of energy depletion and membrane fluidization. *Journal of Pharmacology and Experimental Therapeutics* **2001,** *299* (2), 483-493.
122. Kabanov, A. V.; Levashov, A. V.; Alakhov, V. Y., LIPID MODIFICATION OF PROTEINS AND THEIR MEMBRANE-TRANSPORT. *Protein Engineering* **1989,** *3* (1), 39-42.
123. Andrade, C. D.; Yanez, C. O.; Qaddoura, M. A.; Wang, X. H.; Arnett, C. L.; Coombs, S. A.; Yu, J.; Bassiouni, R.; Bondar, M. V.; Belfield, K. D., Two-Photon Fluorescence Lysosomal Bioimaging with a Micelle-Encapsulated Fluorescent Probe. *Journal of Fluorescence* **2011,** *21* (3), 1223-1230.
124. Andrade, C. D.; Yanez, C. O.; Rodriguez, L.; Belfield, K. D., A Series of Fluorene-Based Two-Photon Absorbing Molecules: Synthesis, Linear and Nonlinear Characterization, and Bioimaging. *Journal of Organic Chemistry* **2010,** *75* (12), 3975-3982.
125. Tian, Y.; Su, F.; Weber, W.; Nandakumar, V.; Shumway, B. R.; Jin, Y.; Zhou, X.; Holl, M. R.; Johnson, R. H.; Meldrum, D. R., A series of naphthalimide derivatives as intra and extracellular pH sensors. *Biomaterials* **2010,** - *31* (- 29), - 7422.
126. Crivello, J. V.; Lam, J. H. W., NEW PREPARATION OF TRIARYLSULFONIUM AND TRIARYLSELENONIUM SALTS VIA COPPER(II)-CATALYZED ARYLATION OF SULFIDES AND SELENIDES WITH DIARYLIODONIUM SALTS. *Journal of Organic Chemistry* **1978,** *43* (15), 3055-3058.
127. Crivello, J. V.; Lam, J. H. W., DYE-SENSITIZED PHOTOINITIATED CATIONIC POLYMERIZATION. *Journal of Polymer Science. Part a-1: Polymer Chemistry* **1978,** *16* (10), 2441-2451.
128. Crivello, J. V.; Lam, J. H. W., PHOTOINITIATED CATIONIC POLYMERIZATION BY DIARYLCHLORONIUM AND DIARYLBROMONIUM SALTS. *Journal of Polymer Science. Part B. Polymer Letters* **1978,** *16* (11), 563-571.
129. Belfield, K. D.; Bondar, M. V.; Przhonska, O. V.; Schafer, K. J., Photostability of a series of two-photon absorbing fluorene derivatives. *Journal of Photochemistry and Photobiology A: Chemistry* **2004,** *162* (2-3), 489-496.
130. Dektar, J. L.; Hacker, N. P., PHOTOCHEMISTRY OF TRIARYLSULFONIUM SALTS. *Journal of the American Chemical Society* **1990,** *112* (16), 6004-6015.
131. DeRosa, M. C.; Crutchley, R. J., Photosensitized singlet oxygen and its applications. *Coordination Chemistry Reviews* **2002,** *233*, 351-371.
132. Mathai, S.; Bird, D. K.; Stylli, S. S.; Smith, T. A.; Ghiggino, K. P., Two-photon absorption cross-sections and time-resolved fluorescence imaging using porphyrin photosensitisers. *Photochemical & Photobiological Sciences* **2007,** *6* (9), 1019-1026.

133. Haggie, P. M.; Verkman, A. S., Unimpaired Lysosomal Acidification in Respiratory Epithelial Cells in Cystic Fibrosis. *J Biol Chem* **2009,** *284* (12), 7681-7686.
134. Benezra, M.; Penate-Medina, O.; Zanzonico, P. B.; Schaer, D.; Ow, H.; Burns, A.; DeStanchina, E.; Longo, V.; Herz, E.; Iyer, S.; Wolchok, J.; Larson, S. M.; Wiesner, U.; Bradbury, M. S., Multimodal silica nanoparticles are effective cancer-targeted probes in a model of human melanoma. *J Clin Invest* **2011,** *121* (7), 2768-2780.
135. Tang, L.; Cheng, J. J., Nonporous silica nanoparticles for nanomedicine application. *Nano Today* **2013,** *8* (3), 290-312.
136. Ji, X. J.; Shao, R. P.; Elliott, A. M.; Stafford, R. J.; Esparza-Coss, E.; Bankson, J. A.; Liang, G.; Luo, Z. P.; Park, K.; Markert, J. T.; Li, C., Bifunctional gold nanoshells with a superparamagnetic iron oxide-silica core suitable for both MR imaging and photothermal therapy. *J Phys Chem C* **2007,** *111* (17), 6245-6251.
137. He, X. X.; Wu, X.; Wang, K. M.; Shi, B. H.; Hai, L., Methylene blue-encapsulated phosphonate-terminated silica nanoparticles for simultaneous in vivo imaging and photodynamic therapy. *Biomaterials* **2009,** *30* (29), 5601-5609.
138. Stober, W.; Fink, A.; Bohn, E., Controlled Growth of Monodisperse Silica Spheres in Micron Size Range. *J Colloid Interf Sci* **1968,** *26* (1), 62-&.
139. Larson, D. R.; Ow, H.; Vishwasrao, H. D.; Heikal, A. A.; Wiesner, U.; Webb, W. W., Silica nanoparticle architecture determines radiative properties of encapsulated fluorophores. *Chem Mater* **2008,** *20* (8), 2677-2684.
140. Bechet, D.; Couleaud, P.; Frochot, C.; Viriot, M. L.; Guillemin, F.; Barberi-Heyob, M., Nanoparticles as vehicles for delivery of photodynamic therapy agents. *Trends Biotechnol* **2008,** *26* (11), 612-621.
141. Couleaud, P.; Morosini, V.; Frochot, C.; Richeter, S.; Raehm, L.; Durand, J. O., Silica-based nanoparticles for photodynamic therapy applications. *Nanoscale* **2010,** *2* (7), 1083-1095.
142. Chatterjee, D. K.; Fong, L. S.; Zhang, Y., Nanoparticles in photodynamic therapy: An emerging paradigm. *Advanced Drug Delivery Reviews* **2008,** *60* (15), 1627-1637.
143. Tang, L.; Fan, T. M.; Borst, L. B.; Cheng, J. J., Synthesis and Biological Response of Size-Specific, Monodisperse Drug-Silica Nanoconjugates. *Acs Nano* **2012,** *6* (5), 3954-3966.
144. Longmire, M.; Choyke, P. L.; Kobayashi, H., Clearance properties of nano-sized particles and molecules as imaging agents: considerations and caveats. *Nanomedicine-Uk* **2008,** *3* (5), 703-717.
145. Bauer, D. R.; Olafsson, R.; Montilla, L. G.; Witte, R. S., 3-D photoacoustic and pulse echo imaging of prostate tumor progression in the mouse window chamber. *Journal of Biomedical Optics* **2011,** *16* (2).
146. Dewhirst, M. W.; Cao, Y.; Moeller, B., Cycling hypoxia and free radicals regulate angiogenesis and radiotherapy response. *Nat Rev Cancer* **2008,** *8* (6), 425-437.